IntechOpen

Surface Waves

New Trends and Developments

Edited by Farzad Ebrahimi

SURFACE WAVES - NEW TRENDS AND DEVELOPMENTS

Edited by **Farzad Ebrahimi**

Surface Waves - New Trends and Developments
http://dx.doi.org/10.5772/intechopen.68840
Edited by Farzad Ebrahimi

Contributors

Shotaro Ishino, Alexander Murynin, Valery Bondur, Piotr Kielczynski, Carlos Javier Zapata-Rodríguez, Slobodan Vukovic, Juan José Miret, Mahin Naserpour, Milivoj Belic, Jobson Nascimento, Regina Maria De Lima Neta, José Moraes Gurgel Neto, Adi Neves Rocha, Alexsandro Aleixo Pereira Da Silva, Volodymyr Fesenko, Vladimir Tuz, Illia Fedorin, Charles Bostater

Notice

First published in London, United Kingdom, 2018 by IntechOpen
eBook (PDF) Published by IntechOpen, 2019
IntechOpen is the global imprint of INTECHOPEN LIMITED, registered in England and Wales, registration number: 11086078, The Shard, 25th floor, 32 London Bridge Street
London, SE19SG – United Kingdom
Printed in Croatia

British Library Cataloguing-in-Publication Data
A catalogue record for this book is available from the British Library

Additional hard and PDF copies can be obtained from orders@intechopen.com

Surface Waves - New Trends and Developments
Edited by Farzad Ebrahimi

p. cm.

Print ISBN 978-1-78923-062-8

Online ISBN 978-1-78923-063-5

eBook (PDF) ISBN 978-1-83881-356-7

Meet the editor

Dr. Farzad Ebrahimi was born in Qazvin, Iran, in 1979. He graduated in Mechanical Engineering from the University of Tehran, Iran, in 2002. He received his MSc and PhD degrees in Mechanical Engineering with a specialization in applied design from the University of Tehran, Iran, in 2009. Since 2002, he has been working at the Smart Materials and Structures Research Center, Faculty of Mechanical Engineering, University of Tehran, where he is a researcher of smart functionally graded materials and structures. He joined the Department of Mechanical Engineering at the Imam Khomeini International University as an associate professor in 2010.

He is involved in several international journals as an Editor and a reviewer. He serves on the Editorial board of the SAGE Publication: *Journal of Advances in Mechanical Engineering*. He is the author of books *Smart Functionally Graded Plates* and *Progress in Analysis of Functionally Graded Structures* (Nova Science Publishers, NY). He also served as the editor of the book *Nanocomposites—New Trends and Developments* (InTech—Open Access Publisher). His research interests focus on the areas of smart materials and structures, nanostructures, vibration nanocomposites, composite materials, and structures, and he has published several researches in these fields. His research in these areas has been presented at international conferences and appeared in academic journals such as *Composite Structures*, *Composites Part B*, *Journal of Mechanical Science and Technology*, *Smart Materials and Structures*, *European Journal of Mechanics*, and *Archive of Applied Mechanics*. He also has a strong collaboration with the Iranian industries on gas and oil projects, and he serves as ad hoc referee in several top academic journals as well.

Contents

Preface

A surface wave is a mechanical wave that propagates along the interface between differing media. A common example is gravity waves along the surface of liquids, such as ocean waves. Gravity waves can also occur within liquids at the interface between two fluids with different densities. Elastic surface waves can travel along the surface of solids, such as Rayleigh or Love waves. Electromagnetic waves can also propagate as "surface waves" in which they can be guided along a refractive index gradient or along an interface between two media having different dielectric constants.

Surface waves have drawn a significant attention and interest in the recent years in a broad range of commercial applications, while their commercial developments have been supported by fundamental and applied research studies.

This book is a result of contributions of experts from international scientific community working in different aspects of *surface waves* and reports on the state-of-the-art research and development findings on this topic through original and innovative research studies.

The book contains up-to-date publications of leading experts, and the edition is intended to furnish valuable recent information to the professionals involved in *surface wave* aspects and technologies. The text is addressed not only to researchers but also to professional engineers, students, and other experts in various disciplines, both academic and industrial, seeking to gain a better understanding of what has been done in the field recently and what kind of open problems are in this area.

I hope that readers will find the book useful and inspiring by examining the recent developments in *surface waves* aspects.

Finally, I would like to thank all the authors for their excellent contributions in different areas covered in this book, and I would also like to thank the InTech team, especially Ms. Renata Sliva, Publishing Process Manager, for her support and patience during the whole process of creating this book.

Dr. Farzad Ebrahimi
Associate Professor
Department of Mechanical Engineering
Imam Khomeini International University
Qazvin, Iran

Chapter 1

Novel Waveguide Technologies and Its Future System Applications

Shotaro Ishino

Additional information is available at the end of the chapter

http://dx.doi.org/10.5772/intechopen.72039

Abstract

Radio waves are widely used in the fields of communication and sensing, and technologies for sending wireless power are currently being put to practical use. The barriers that have so far limited these technologies are about to disappear completely. In the present study, we examine waveguides, which are a key component of the next-generation wireless technologies. A waveguide is a metal pipe through which radio waves transfer. Although a waveguide is a very heavy component, due to technological innovations, waveguides will undergo drastic modifications in the near future. This chapter introduces trends in innovative waveguide technologies and the latest wireless systems, including communication and power transfer system, that use waveguides.

Keywords: microwaves, radio waves, wave propagation, electromagnetic theory, surface transmission, evanescent wave, components, waveguide, antenna, wireless communication, wireless power transfer, wireless systems

1. Introduction

Electromagnetic waves are waves formed by changing electric and magnetic fields in space. Electromagnetic waves refer to waves with a wavelength of 100 μm or more (3 THz or less). They are described as microwaves or millimeter waves, depending on the wavelength. The existence of electromagnetic waves was predicted by J. C. Maxwell in 1864. J. C. Maxwell proved that the speed at which electromagnetic waves propagate is equal to the speed of light and revealed the fundamental principle that light is propagated in the form of electromagnetic waves [1]. In 1888, H. R. Herth confirmed the presence of electromagnetic waves. This experimentally demonstrated the existence of the electromagnetic waves that was theoretically explained by Maxwell and was shown by the air propagation that Maxwell had not revealed [2]. In 1895, G. Marconi

succeeded in wireless telegraphy [3–5]. In Japan, radio broadcasting began in 1925, and television broadcasting began in in 1953. Moreover, to date, electromagnetic waves are used for various purposes ranging from communication and sensing to microwave ovens. Electromagnetic waves are colloquially described as "fluttering in space," and it can be said that life is established by these waves. In recent years, attention has been paid to a technology for wireless power transfer. This technology converts electric power that was previously sent by wire into electromagnetic waves to transmit electricity in space [6–9]. In around the 1900s, N. Tesla tried wireless transmission at a frequency of 150 kHz but failed in his attempts. However, in the 1960s, W. Brown succeeded with his experiments by using microwaves at 2.45 GHz [10]. Research on wireless power transfer is being actively conducted for the range of several-microwatts, used for energy harvesting [11–14] and RFID [15, 16], to the several-kilowatts, used for applications in space in solar power satellites [17–19]. Ultimately, a perfect wireless smart society (**Figure 1**) may be realized in which all wires are unnecessary. As G. Marconi said, "It is dangerous to put limits on wireless." The possibilities of wireless are, indeed, infinite.

However, electromagnetic waves have several drawbacks. As electromagnetic waves propagate, the propagation loss increases because they spread out in space when radiated. This is indicated by the Friis formula [20, 21] and is a physically fixed loss. When the transmission power is Pt, the received power is Pr, the wavelength is λ, and the transmission distance is d, then the transmission equation is as follows.

$$Pr = \left(\frac{\lambda}{4\pi d}\right)^2 Pt \tag{1}$$

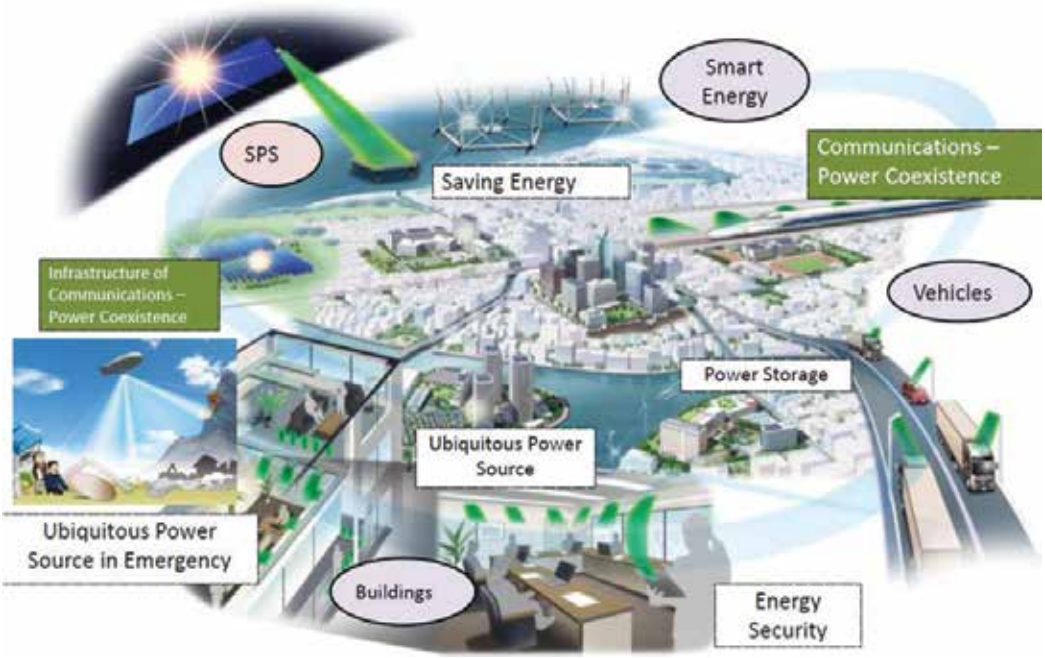

Figure 1. Our dream: wireless smart society [19].

The received power is inversely proportional to the square of the distance and it attenuates. Moreover, if shields are present between transmission and reception of power or if the line of sight is bad, then the attenuation increases further or is completely cut off. Therefore, efficient and reliable transmission is an issue. In the future wireless society, a transmission path that assists transmission lines will play an important role. In this study, we examine waveguides, which are a key component of the next-generation wireless technologies. A waveguide is a metal pipe through which radio waves transfer. Despite being a very heavy component, due to technological innovations, waveguides will undergo drastic modifications in the near future. This chapter introduces trends in innovative waveguide technologies and the latest wireless systems, including communication and power transfer system, that use waveguides.

2. What is a waveguide

A waveguide is a transmission line that transmits electromagnetic waves in a hollow tube (**Figure 2**). Initially, J. J. Thomson and L. Rayleigh et al. came up with the first proposal for such a system [22–30]. Since a waveguide is installed within an enclosed tube, the problem of blocking transmission is solved, thus contributing to improved reliability. There is no fear of power spreading in space; thus, there is no transmission loss. Compared to other forms of transmission, better transmission efficiency is offered by a waveguide. For utilizing the features of waveguides, they are widely used as components for high-power transmission, such as for feeding to an antenna for broadcasting and application between a magnetron and a chamber in a microwave oven. Microwave heating applications are not limited to domestic microwave ovens but extend to industrial applications such as food processing [31–33] and smelting of iron ores [34, 35]. A waveguide is designed to be approximately $\lambda/2$ with respect to the wavelength of the electromagnetic wave to be used if the waveguide is circular in diameter. Moreover, in the case of rectangular waveguide, a waveguide is long side dimension.

The electromagnetic field is a wave that exhibits sinusoidal variation in time. By solving Maxwell's equations and the Helmholtz equations, the solution of the electromagnetic field propagating in the +z direction can be classified into the following three types [36].

$$E_z = 0, \quad H_z = 0; \text{ Transverse electric and magnetic (TEM)} \tag{2}$$

$$E_z = 0, \quad H_z \neq 0; \text{ Transverse electric (TE)} \tag{3}$$

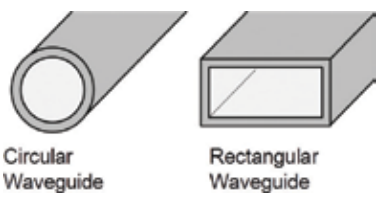

Figure 2. Examples of waveguides.

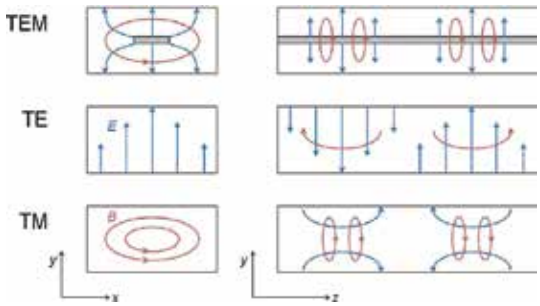

Figure 3. Propagation modes.

$$E_z \neq 0, \quad H_z = 0; \text{ Transverse magnetic (TM)} \tag{4}$$

An electromagnetic field can be expressed as a combination of three types of waves. The TEM wave has no electromagnetic field component in the propagation direction. The wave is an entirely transverse electromagnetic wave. A plane wave propagating in space, a flat plate line, and an electromagnetic wave transmitted inside the coaxial line are all TEM waves. A plane wave propagating in an electromagnetic field can be expressed as a combination of three types of waves. Space, a flat plate line, and an electromagnetic wave transmitted inside a coaxial line are TEM waves. The states of the electric and magnetic fields in the x–y plane perpendicular to the propagation direction of the TEM wave are the same as those of the electrostatic field and the static magnetic field. Because there is no electrostatic field in the tube surrounded by the conductor wall of the same potential, the TEM wave does not propagate to the waveguide. In order to propagate the TEM wave, it is necessary to use a transmission path comprising two or more insulated conductors.

TE and TM waves are generated in the waveguide. The TE wave is also known as the H wave. The z component of the electric field E is an electromagnetic wave with $Ez = 0$. The electric field is a transverse wave. The magnetic field is a longitudinal wave. In a rectangular waveguide, electromagnetic waves are transmitted with the TE wave as a basic mode. The TM wave is also known as the E wave. The z component of the magnetic field H is an electromagnetic wave with $Hz = 0$. The electric field is the longitudinal and transverse waves, and the magnetic field is the transverse wave. The spherical wave propagating in space is a TM wave (**Figure 3**).

A cut-off frequency exists in the waveguide, and a frequency lower than the cut-off frequency is in the attenuation mode (evanescent mode) and cannot be transmitted. That is, it functions as a high-pass filter. Conversely, in the TEM wave transmission, the frequency is arbitrary and there is no cut-off frequency.

3. Novel waveguide technologies

3.1. 3D printing waveguides

3D printers were invented in the 1980s [37, 38], and their applications are spreading rapidly. Originally known as rapid prototyping machine, a 3D printer is a molding machine that specializes in rapid shaping. In recent years, the price of 3D printers has reduced, and home-use

3D printers based on thermal melting lamination are also available for sale. Moreover, for business use, machines that employ the inkjet method, optical shaping, and powder sintering molding are used in the development department of the manufacturing industry. Because 3D prototypes can be made without a mold, they can be made using simple prototyping.

Various reports have been produced on prototypes of waveguides and peripheral components made by resin molding 3D printers [39–43]. Because electromagnetic waves cannot be confined in plastic tubes, it is necessary to make additional conductive membranes on the surface of the pipe. Thus, although a film having high conductivity can be formed by the plating method, the film thickness is approximately 1 μm and so the microwave penetrates into the inside of the film before finally being transmitted. Thus, adequate shielding properties cannot be obtained. There are also examples that employ a conductive paint to achieve a film thickness of approximately 10 μm; however, the conductivity is poor and the loss due to the conductor becomes large. Moreover, these are mainly microwave components. For millimeter wave components, fine processing is required, which is difficult to realize with the current processing precision.

Moreover, evaluation of several resin materials of the acrylonitrile butadiene styrene such as the resin used in the optical fabrication method revealed that the value of the imaginary part of the dielectric constant, which is a factor of the loss of electromagnetic waves, is relatively large. In the future, it is desirable to develop low-loss materials and molding methods for microwave components.

Moreover, 3D printers capable of directly molding metallic materials are also being used. Metal powder can be sintered by selective laser sintering or selective laser melting. As a result, processing of the conductive film and losses due to resin are eliminated. However, unevenness is formed on the surface, and there can be a problem with the surface becoming very rough. As surface roughness decreases, the conductivity of the surface decreases conduction loss increases. Currently, aluminum alloys are mainly used in 3D printing as materials, but a practical use of copper-based materials is progressing. If the conductivity of the material improves, this loss can be expected to decrease. We fabricated a 10-GHz rectangular waveguide and evaluated its characteristics (**Figure 4**). As a result, there was a transmission loss of approximately 1.5 times than that of the usual waveguide. There was also a leak from the flange portion. The connection was improved by polishing unevenness, but additional work is still required.

3.2. Hose-type waveguide

Weight reduction of the waveguide is done by using resin, but the structure of the waveguide has remained as a non-hollow, solid pipe. Therefore, we are developing a flexible waveguide that is like a water hose. Besides improving convenience by making the pipe flexible like a

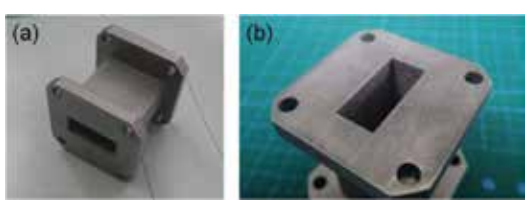

Figure 4. (a) Metallic rectangular waveguide and (b) polished surface.

hose, the image changes and the application range may expand. We introduce an example in which a waveguide is made by winding a copper foil in a hollow resin hose [44].

Our waveguide is a hollow, soft-resin hose with a conductive coating on the outside for electromagnetic wave transfer. Conventional metal waveguides undergo passage, return, and conductive losses, which should be reduced as far as possible. Resin waveguides generate additional dielectric and radiation losses. The dielectric losses are due to absorption by the resin, and radiation losses occurs by leakage due to the insufficient shielding of the thin-film conductor. Dielectric and radiation losses are the dominant loss components in resin waveguides (**Figure 5**).

In this study, we use a soft elastomer material with excellent properties for forming flexible waveguides. In the 10-GHz band, the relative permittivity and dielectric loss tangent of the resin are $\varepsilon' r = 2.28$ and $\tan\delta = 0.00072$, respectively, ensuring very low losses as in a Teflon.

Conversely, the conventional metal-film-deposition techniques of plating, sputtering, and vapor deposition are limited to conductive films with submicron thickness. The required thickness at 10 GHz, estimated from the skin-depth relationship, is at least 10 μm. Therefore, the film in our prototype was formed by winding an 18-μm-thick copper foil around the aforementioned resin hose. We investigated several types of foil winding and found that the lowest radiation loss occurs in the H-center configuration of the waveguide.

The prototype (**Figure 6**) weighs 67 g/m and costs $1.3 per meter, enabling a lightweight and inexpensive waveguide. The waveguide has a low loss and low emission, with a transmission characteristic of −0.39 dB/m in the 10-GHz band.

In future application to automated vehicles, it is necessary to install various sensors, e.g., high-quality inter-vehicle cameras [45–50] that requires transmission speeds on the order of several Gbps [51] with high security. Conventional wire harnesses cannot tolerate external noise in transfers on the order of several Gbps. Because the influence of noise increases with transmission speed, we believe that it is necessary to review the transmission line design. As shown in **Figure 7**, the proposed waveguide is laid from the front to the back to transmit a camera image. The camera image was transmitted inside the waveguide by using high-speed communication between sensors.

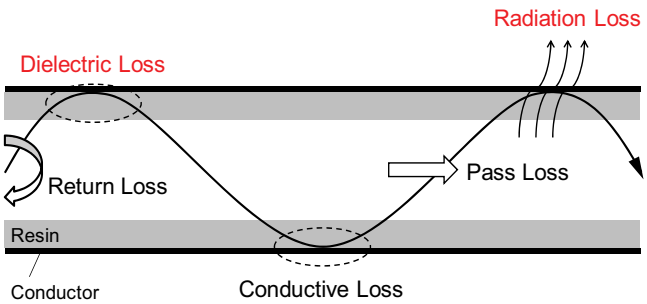

Figure 5. Loss factors in the resin waveguide.

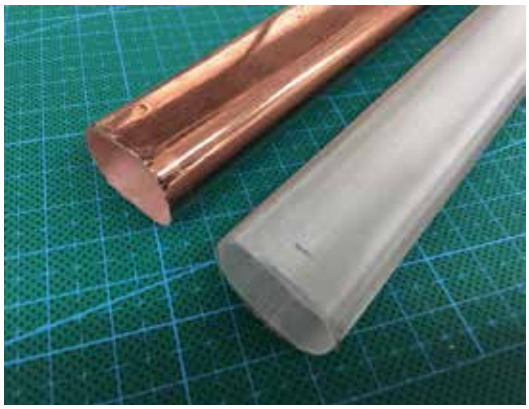

Figure 6. Hose-type waveguides.

3.3. Sheet-type waveguide

Research on two-dimensional communication by using electromagnetic waves that propagate in a thin sheet is progressing [52, 53]. It is assumed that the communication distance is up to several meters. Moreover, by placing a type of antenna known as a coupler at an arbitrary point in the sheet form, close proximity communication inside and outside the seat can be made possible (**Figure 8**). It uses evanescent waves that ooze out of the sheet. The evanescent wave is an electromagnetic wave propagating only near the surface of the sheet. In this way, the sheet-shaped waveguide does not require wiring for each sensor terminal and does not radiate electromagnetic waves to space. In addition to contribute to improving communication security, a relatively large power can be transmitted without exposing people or objects that are not close to the seat to a strong electromagnetic field. Applications for wireless power transmission are also under consideration. Moreover, in the case of Japan, standard specifications for wireless power transfer in the seat are also in place [54]. For future applications, a power supply for a car while in motion and wearable sensor devices are being considered [55].

3.4. DC waveguide

The conventional waveguide is a high-pass filter and cannot transmit bands below the cutoff frequency. However, if the structure can be revised for direct current (DC) propagation, then

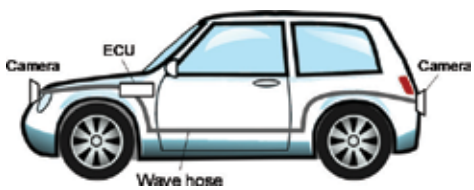

Figure 7. Inter-vehicle communication system.

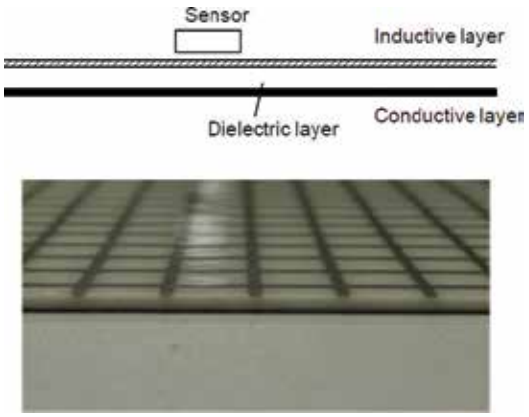

Figure 8. Sheet-type waveguide [52].

high-power transmission becomes possible with a sufficient pipe thickness. We also consider that if a stop band sufficiently far from the pass band can be transmitted, then we can achieve low-frequency communication and sharing in addition to broadband communication. We propose a waveguide with a divided structure that operates not only in a conventional (**Figure 9a**) but also in DC (**Figure 9b**) and parallel line (**Figure 9c**) modes. Subsequently, we investigated whether the waveguide realizes DC in DC mode and can transmit the stop band in a parallel line mode. The conventional mode is a TE10 mode, and the parallel line mode is a TEM mode. It is known as DC waveguide [56].

Although the result (**Figure 10**) differs from simulation results, transmission in the stop band was, at least to some extent, experimentally confirmed. In DC mode, the resistance was approximately 0 Ω, confirming that high-efficiency DC transmission is also possible.

In future work, we will assess the performance of the waveguide in industrial applications. Such plural transmission modes are desired for high-power transmission and broadband communications in automatic driving.

3.5. Substrate integrated waveguide (SIW)

A conventional waveguide is a non-planar three-dimensional circuit, and it is a challenge to fabricate such a waveguide in bulk. SIWs act as an alternative option to conventional waveguides

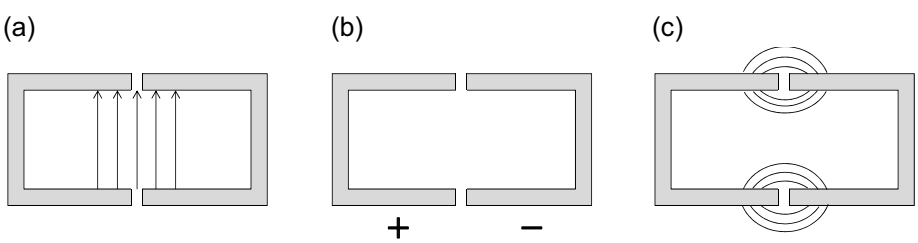

Figure 9. Propagation modes of the split waveguide.

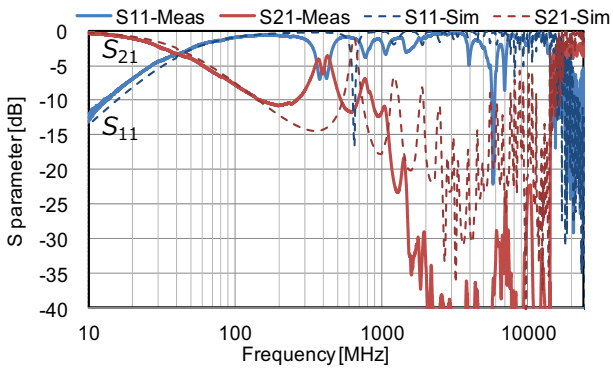

Figure 10. Measured results of DC waveguide.

[57–62]. SIWs are planar structures fabricated using metallic via-hole arrays connecting the top and bottom ground planes of a dielectric substrate (**Figure 11**). A non-planar conventional waveguide can be modeled into a substrate integrated circuit. They are compact, lightweight, cost-effective, and easy to fabricate. Microfabrication of SIW of several microns is also possible, and usage in the terahertz-band order is also expected to be promising.

An example in which a resonance structure is provided in a tube like a conventional waveguide to form a band-pass filter has also been reported [63–66]. We also report an example of fabricating band-stop filters with stacked waveguide structures by SIW [67].

When the microwave is input to the SIW filter, reflection occurs due to a mismatch of the characteristic impedance at the input portion. The microwave input to the filter is distributed at a distribution ratio in the microstrip layer and the waveguide layer. Microwaves entering the microstrip layer ideally do not reflect and propagate. When the microwave entering the waveguide layer is at the frequency of the cutoff region of the waveguide, it propagates while attenuating. Thus, the attenuated portion becomes a reflected wave. Subsequently, at the output of the multilayer substrate filter, microwaves output from the microstrip layer and the waveguide layer are synthesized. Therefore, due to the phase difference of the microwaves output from each layer, propagation waves are canceled at a certain frequency, resulting in reflection. This is the principle that enables an SIW to function as a band-stop filter.

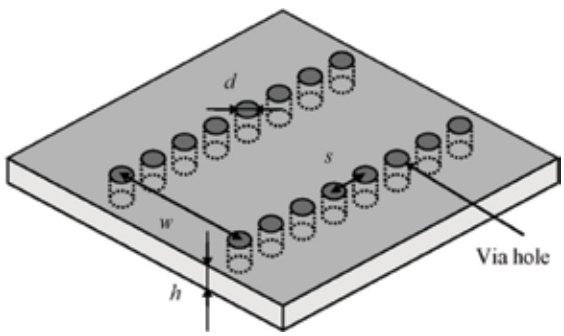

Figure 11. Configuration of an SIW structure synthesized using metallic via-hole arrays [57].

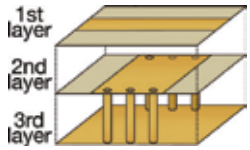

Figure 12. Multilayer SIW filter [67].

In this way, a SIW can easily realize a complicated circuit like a laminated structure. Structures and characteristics that were impossible with a stereo waveguide are obtained and can be expected to be used in various applications. The use of the band-stop filter as the harmonic circuit of the F-class amplifier [68–70] and rectifier [71, 72] are being studied. It can be expected that the efficiency of the microwave circuit can be improved, thus contributing to a low-fuel-consumption society (**Figure 12**).

4. Conclusion

This chapter introduced the novel waveguide technology. The conventional waveguide is characterized as being a large mass of metal, but the proposed waveguide is light, thin, cheap, can change its shape. Thus, waveguides are drastically renewed by the proposed novel technology. Thus, it is time for classic circuits to make a big leap forward.

In addition, along with the technical improvement to the machining technology, a waveguide circuit with a new function can also be realized. We will continue to fuse semiconductor and micro electro mechanical systems (MEMS) processes to develop fine and precise circuit technologies. In addition, we also introduced some application examples. From the microwave band to the terahertz band, the waveguide will be widely used more than ever. In order to realize a sustainable wireless society, the proposed waveguide will prove to be a key component.

Acknowledgements

I am grateful to Dr. Farzad Ebrahimi (University of Tehran, Iran) of the book editor who gave me the opportunity to write this chapter. Moreover, I respect the great achievements of my predecessors whose studies I have cited.

Author details

Shotaro Ishino

Address all correspondence to: shotaroh.ishino.qx@furuno.co.jp

Furuno Electric, Nishinomiya, Hyōgo Prefecture, Japan

References

[1] Maxwell JC. A dynamical theory of the electromagnetic field. Philosophical Transactions. Royal Society of London. 1865;**155**:459-512

[2] Herth HR. Ueber sehr schnelle electrische Schwingungen. Leipzig: Barth; 1887

[3] Telegraphing without Wires. Chicago, IL: Chicago Eagle; 1897. p. 10

[4] Baker WJ. A History of the Marconi Company 1874-1965. London: Methuen; 1970. pp. 28-29

[5] Record of the Development of Wireless Telegraphy, The Year Book of Wireless Telegraphy and Telephony. London, Pub. for the Marconi Press Agency Ltd., by the St. Catherine Press; 1922. p. 27

[6] Shinohara N. Wireless Power Transfer via Radiowaves (Wave Series). Great Britain and United States: John Wiley & Sons, Inc., 2014. ISBN: 978-1-84821-605-1

[7] Suh Y-H, Chang K. A high-efficiency dual-frequency rectenna for 2.45- and 5.8-GHz wireless power transmission. IEEE Transactions on Microwave Theory and Techniques. 2002;**50**(7):1784-1789

[8] Shinohara N. Power without wires. IEEE Microwave Magazine. 2011;**12**(7):S64-S73

[9] Popovic Z. Cut the cord: Low-power far-field wireless powering. IEEE Microwave Magazine. 2013;**14**(2):55-62

[10] Brown WC. The history of power transmission by radio waves. IEEE Transactions on Microwave Theory and Techniques. 1984;**32**(9):1230-1242

[11] Doig A. Off-grid electricity for developing countries. IEE Review. 1999;**45**(1):25-28

[12] Mateu L, Moll F. Review of energy harvesting techniques and applications for micro-electronics. In: VLSI Circuits and Systems II; 2005. pp. 359-373

[13] Arrawatia M, Baghini MS, Kumar G. RF energy harvesting system at 2.67 and 5.8GHz. In: IEEE Asia-Pacific Microwave Conference; 2010. pp. 900-903

[14] Furuta T, Ito M, Nambo N, Ito K, Noguchi K, Ida J. The 500MHz band low power rectenna for DTV in the Tokyo area. In: IEEE Wireless Power Transfer Conf.; 2016

[15] Want R. An introduction to RFID technology. IEEE Pervasive Computing. 2006;**5**(1):25-33

[16] Karthaus U, Fischer M. Fully integrated passive UHF RFID transponder IC with 16.7-μW minimum RF input power. IEEE Journal of Solid-State Circuits. 2003;**38**(10):1602-1608

[17] McSpadden JO, Mankins JC. Space solar power programs and microwave wireless power transmission technology. IEEE Microwave Magazine. 2002;**3**(4):46-57

[18] Matsumoto H. Research on solar power satellites and microwave power transmission in Japan. IEEE Microwave Magazine. 2002;**3**(4):36-45

[19] Shinohara N. Wireless Power Transfer via Radiowaves (Wave Series). IEEE MTT-S Distinguished Microwave Lecture. 2017

[20] Friis HT. A note on a simple transmission formula. Proceedings of the IRE. 1946;**34**(5): 254-256

[21] Hogg DC. Fun with the Friis free-space transmission formula. IEEE Antennas and Propagation Magazine. 1993;**35**(4):33-35

[22] Thomson JJ. Note on Recent Researches in Electricity and Magnetism. Oxford: Clarendon; 1968. pp. 344-347

[23] Lang VV. Interferenversuch mit elekrischen Wellen. Wied. Ann. 1896;**57**:430

[24] Becker A. Interferenröhren fürelektrische Wellen. Annalen der Physik. 1902;**8**(4):22

[25] Kalähne A. Elektrische Schwingungen in ringförmigen Metallröhren. Annalen der Physik. 1905;**18**(4):92

[26] Rayleigh L. On the passage of electric waves through tubes, or the vibrations of dielectric cylinders. Philosophical Magazine. 1897;**XLIII**:125-132

[27] Weber RH. Elektromagnetische Schwingungen Metallröhren. Annalen der Physik. 1902;**8**(4):721

[28] Silberstein L. Electromagnetic waves in a prefectly conducting tube. Proc. Roy. Soc. 1915;**91**:170

[29] McLachlan NW. Theory and Application of Mathieu Functions. London: Oxford University Press. 1964;8

[30] Packard KS. The origin of waveguides: A case of multiple rediscovery. IEEE Transactions on Microwave Theory and Techniques. 1984;**32**(9):961-969

[31] Gardiol FE. Introduction to Microwaves. Dedham, Mass.: Artech House; 1984

[32] Hoogenboom R, Wilims TFA, Erdmenger T, Schubert US. Microwave assisted chemistry: A closer look at heating efficiency. Australian Journal of Chemistry. 2009;**62**:236-243

[33] Meredith RJ. Engineers' Handbook of Industrial Microwave Heating, Institution of Electrical Engineers. 1998.

[34] Kashimura K, Nagata K, Sato M. Concept of furnace for metal refining by microwave heating - A design of microwave smelting furnace with low CO_2 emission. Materials Transactions. 2010;**51**(10):1847-1853

[35] Hara K, Hayashi M, Sato M, Nagata K. Pig iron making by focused microwave beams with 20 kW at 2.45 GHz. ISIJ International. 2012;**52**(12):2149-2157

[36] Marcuvitz N. Waveguide Handbook. (Iee Electromagnetic Waves Series). The Institution of Engineering and Technology. 1951

[37] Kodama H. Automatic method for fabricating a three-dimensional plastic model with photo-hardening polymer. Review of scientific instruments. 1981;**52**(11): 1770-1773

[38] Herbert AJ. Solid object generation. Journal of Applied Photographic Engineering. 1982;**8**(4):185-188

[39] McKerricher G, Nafe A, Shamim A. Lightweight 3D printed microwave waveguides and waveguide slot antenna. In: Antennas and Propagation & USNC/URSI National Radio Science Meeting; 2015

[40] Liang M, Xin H. 3D printed microwave and THz components. In: Proc. Asia-Pacific Microw. Conf.; 2015

[41] Zhang B, Linnér P, Kärnfelt C, Tam PL, Södervall U, Zirath H. Attempt of the metallic 3D printing technology for millimeter-wave antenna implementations. In: Proc. Asia-Pacific Microw. Conf.; 2015

[42] Shen J, Aiken M, Abbasi M, Parekh D, Zhao X, Dickey M, Ricketts D. Rapid prototyping of low loss 3D printed waveguides for millimeter-wave applications. In: IEEE MTT-S Int. Microw. Symp.; 2017

[43] Peverini O, Lumia M, Addamo G, Caligano F, Virone G, Ambrosio E, Manfredi D, Tascone R. Integration of RF functionalities in microwave waveguide components through 3D metal printing. In: IEEE MTT-S Int. Microw. Symp.; 2017

[44] Ishino S, Yano K, Matsumoto S, Kashiwa T, Shinohara N. Development of a novel 10 GHz-band hose-type soft resin waveguide. In: IEEE MTT-S Int. Microw. Symp.; 2017

[45] Erico G. How google's self-driving car works. IEEE Spectrum Online. 2011:1-4

[46] Jensen C. Volvo Crash Prevention System Receives High Marks From Insurance Institute. ed. New York, NY, USA: The New York Times. 2011

[47] Motro M et al. Communications and Radar-Supported Transportation Operations and Planning: Final Report. Center for Transportation Research, The University of Texas at Austin No. FHWA/TX-16/0-6877-1. 2017

[48] Lim HT, Krebs B, Volker L, Zahrer P. Performance evaluation of the inter-domain communication in a switched Ethernet based in-car network. In: 2011 IEEE 36th Conf. on Local Computer Networks; 2011. pp. 101-108

[49] Lim HT, Volker L. Challenges in a future IP/Ethernet-based in-car network for real-time applications. In: Design Automation Conf.; 2011. pp. 7-12

[50] Tuohy S, Glavin M, Hughes C, Jones E, Trivedi M, Kilmartin L. Intra-vehicle networks: A review. IEEE Transactions on Intelligent Transportation Systems. 2015;**16**:534-545

[51] Wang J, Lan Z, Pyo CW, Baykas T, Sum CS, Rahman MA, Gao J, Funada R, Kojima F, Harada H, Kato S. Beam codebook based beamforming protocol for multi-Gbps millimeter-wave WPAN systems. IEEE Journal on Selected Areas in Communications. 2009;**27**(8):1390-1399

[52] Shinoda H, Makino Y, Yamahira N, Itai H. Surface sensor network using inductive signal transmission layer. In: Proc. INSS07; 2007. pp. 201-206

[53] Noda A, Shinoda H. Selective wireless power transmission through high-Q flat waveguide-ring resonator on 2-D waveguide sheet. IEEE Transactions on Microwave Theory and Techniques. 2011;**59**(8):2158-2167

[54] ARIB STD-T113 ver. 1.1 (in Japan); 2015

[55] Noda A, Shinoda H. Frequency-division-multiplexed signal and power transfer for wearable devices networked via conductive embroideries on a cloth. In: IEEE MTT-S Int. Microw. Symp.; 2017

[56] Ishino S, Yano K, Matsumoto S, Kashiwa T, Shinohara N. Study of a novel DC, stop band, and pass band compatibility three-mode waveguide (in Japanese). In: IEICE General Conf.; 2017

[57] Xu F, Wu K. Guided-wave and leakage characteristics of substrate integrated waveguide. IEEE Transactions on Microwave Theory and Techniques. 2005;**53**(1):66-73

[58] Hirokawa J, Ando M. Single-layer feed waveguide consisting of posts for plane TEM wave excitation in parallel plates. IEEE Transactions on Antennas and Propagation. 1998;**46**(5):625-630

[59] Deslandes D, Wu K. Integrated transition of coplanar to rectangular waveguides. In: IEEE MTT-S Int. Microw. Symp.; 2001. pp. 619-622

[60] Zeid A, Baudrand H. Electromagnetic scattering by metallic holes and its applications in microwave circuit design. IEEE Transactions on Microwave Theory and Techniques. 202;**50**(4):1198-1206

[61] Cassivi Y, Perregrini L, Arcioni P, Bressan M, Wu K, Conciauro G. Dispersion characteristics of substrate integrated rectangular waveguide. IEEE Microwave and Wireless Components Letters. 2002;**12**:333-335

[62] Deslande D, Wu K. Single-substrate integration technique of planar circuits and waveguide filters. IEEE Transactions on Microwave Theory and Techniques. 2003;**51**(2):593-596

[63] Chen X-P, Hong W, Cui T, Hao Z, Wu K. Substrate integrated waveguide elliptic filter with transmission line inserted inverter. Electronics Letters. 2005;**41**:851-852

[64] Chen X-P, Hong W, Chen J, Wu K. Substrate integrated waveguide elliptic filter with high mode. In: Asia–Pacific Microw. Conf.; 2005

[65] Chang C-Y, Hsu W-C. Novel planar, square-shaped, dielectric-waveguide, single-, and dual-mode filters. IEEE Transactions on Microwave Theory and Techniques. 2002;**50**(11):2527-2536

[66] Chen X-P, Wu K. Substrate integrated waveguide cross-coupled filter with negative coupling structure. IEEE Transactions on Microwave Theory and Techniques. 2008;**56**(1):142-149

[67] Wright P et al. Highly efficient operation modes in GaN power transistors delivering upwards of 81% efficiency and 12 W output power. In: IEEE MTT-S Int. Microw. Symp.; 2008

[68] Kim H, et al. A high-efficiency inverse class-F power amplifier using GaN HEMT. Microwave and Optical Technology Letters. 2008;**50**(9):2420-2423

[69] Kuroda K, Ishikawa R, Honjo K. Parasitic compensation design technique for a C-band GaN HEMT Class-F Amplifier. IEEE Trans. Microw. Theory Tech. 2010;**58**(11):2741-2750

[70] Raab F. Class-E, Class-C, and Class-F power amplifiers based upon a finite number of harmonics. IEEE Transactions on Microwave Theory and Techniques. 2001;**49**(8):1462-1468

[71] Roberg M, Falkenstein E, Popović Z. High-efficiency harmonically-terminated rectifier for wireless powering applications. In: IEEE MTT-S Int. Microw. Symp.; 2011

[72] Hatano K, Shinohara N, Mitani T, Nishikawa K, Seki T, Hiraga K. Development of class-F load rectennas. In: IEEE MTT-S Int. Microw. Symp.; 2010

Chapter 2

Properties and Applications of Love Surface Waves in Seismology and Biosensors

Piotr Kiełczyński

Additional information is available at the end of the chapter

http://dx.doi.org/10.5772/intechopen.75479

Abstract

Shear horizontal (SH) surface waves of the Love type are elastic surface waves propagating in layered waveguides, in which surface layer is "slower" than the substrate. Love surface waves are of primary importance in geophysics and seismology, since most structural damages in the wake of earthquakes are attributed to the devastating SH motion inherent to the Love surface waves. On the other hand, Love surface waves found benign applications in biosensors used in biology, medicine, and chemistry. In this chapter, we briefly sketch a mathematical model for Love surface waves and present examples of the resulting dispersion curves for phase and group velocities, attenuation as well as the amplitude distribution as a function of the depth. We illustrate damages due to Love surface waves generated by earthquakes on real-life examples. In the following of this chapter, we present a number of representative examples for Love wave biosensors, which have been already used to DNA characterization, bacteria and virus detection, measurements of toxic substances, etc. We hope that the reader, after studying this chapter, will have a clear idea that deadly earthquakes and a beneficiary biosensor technology share the same physical phenomenon, which is the basis of a fascinating interdisciplinary research.

Keywords: Love waves, biosensors, earthquakes, surface acoustic waves, wireless sensors, dispersion curves

1. Introduction

It is interesting to note that many outstanding physicists (Kelvin, Michelson, and Jolly) expressed in the second half of the nineteenth century an opinion that classical physics (how we name it nowadays) is in principle completed and nothing interesting or significant rests to be discovered. Needless to say, forecasting development of future events was always and

still is a very risky business, especially in physical sciences and engineering. Indeed, in these disciplines of human endeavors, one must take into account not only an inherently volatile human factor but also the impact of potential discoveries of unknown yet laws of nature, which often open new unanticipated possibilities and horizons. We may try to justify such an obvious complacency, attributed to the abovementioned scientists, by the historical spirit of the Belle Époque (1870–1914), that believed in harmony, good taste, optimism, unlimited progress and generally in positivistic philosophical ideas.

Anyway, not waiting for the revolution heralded by quantum mechanics (1900) or general theory of relativity (1917), classical physics was already shaken by the emergence of the theory of chaos (Poincaré 1882 and Hadamard 1898), which later on in the twentieth century will effectively eliminate deterministic description from many physical problems, such as weather forecasting, etc. Another new significant achievement of the classical physics (although not revolutionary) was the discovery of surface waves. At first, elastic surface waves were discovered in solids (Rayleigh 1885 and Love 1911) and then in electromagnetism (Zenneck 1907 and Sommerfeld 1909).

In fact, the existence of surface waves in solids was predicted mathematically by the celebrated British scientist Lord Rayleigh in 1885, who showed that elastic surface waves can propagate along a free surface of a semi-infinite body. By contrast to bulk waves, the amplitude of surface waves is confined to a narrow area adjacent to the guiding surface. Since surface waves are a type of guided waves, they can propagate often longer distances than their bulk counterparts and in addition, they are inherently sensitive to material properties in the vicinity of the guiding surface. It will be shown in the following of this chapter that these two properties of surface waves are of crucial importance in geophysics and sensor technology.

First, seismographs were constructed by British engineers in 1880, working in Japan for Meiji government. Consequently, the first long distance seismogram was registered in 1889 by German astronomer Ernst von Rebeur-Paschwitz in Potsdam (Germany), who was able to detect seismic signals generated by an earthquake occurred in Japan, some 9000 km away from Potsdam (Berlin). It was obvious soon that long distance seismograms display two different phases. First (preliminary tremor), a relatively weak signal arriving with the velocity of bulk waves (P and S) and second (main shock) with a much higher amplitude arriving with the velocity close to that of Rayleigh surface waves. However, this Rayleigh wave hypothesis was not satisfactory, since large part of the main shock energy was associated with the shear horizontal (SH) component of vibrations, absent by definition in Rayleigh surface waves composed of shear vertical (SV) and longitudinal (L) displacements. This dilemma was resolved in 1911 by the British physicist and mathematician Augustus Edward Hough Love by a brilliant stroke of thought [1]. Firstly, Love postulated that the SH component in the main shock is due to the arrival of a new type of surface waves (named later after his name) with only one SH component of vibrations. Secondly, Love assumed that SH surface waves are guided by an extra surface layer existing on the Earth's surface, with properties different than those in the Earth's interior. Using contemporary language, we can say that he made a direct hit.

It is noteworthy that the existence of Rayleigh and Love surface waves was first predicted mathematically prior to their experimental confirmation. This shows how beneficial can be the mutual interaction between the theory and experiment. Indeed, the theory indicates directions of future experimental research and the experiment confirms or renders the theory obsolete. It is worth noticing that the existence of a new type of electromagnetic surface waves was predicted mathematically quite recently, i.e., in 1988, and soon confirmed experimentally.

It is interesting to note that Love surface waves have direct counterparts in electromagnetism (optical planar waveguides) and quantum mechanics (particle motion in a quantum well). By contrast, a similar statement is not true for Rayleigh surface waves, which therefore remain a unique phenomenon within the frame of the classical theory of elasticity.

Surface waves of the Love type have a number of unique features. Firstly, they have only one SH component of vibrations. As a result, Love surface waves are insensitive to the loading with liquids of zero or negligible viscosities. Thus, Love surface waves can propagate long distances without a significant attenuation. Indeed, Love waves propagating many times around the Earth's circumference have been observed experimentally. On the other hand, it was discovered much later (1981) that Love waves are very well suited for measurements of viscoelastic properties of liquids. Secondly, the mathematical description of Love surface waves is much simpler than that for Rayleigh surface waves. A relative simplicity of the mathematical model enables for direct physical insight in the process of Love wave propagation, attenuation, etc.

The idea to employ Love surface waves for measurements of viscoelastic properties of liquids was presented for the first time in 1981 by Kiełczyński and Płowiec in their Polish patent [2]. In 1987, the theory of the new method was presented by Kiełczyński and Pajewski on the international arena at the European Mechanics Colloquium 226 in Nottingham, UK [3]. In 1988, they presented this new method with equations and experimental results at the IEEE 1988 Ultrasonic Symposium in Chicago [4]. In 1989, Kiełczyński and Płowiec published a detailed theory and experimental results in the prestigious Journal of the Acoustical Society of America [5]. It is noteworthy that subsequent publications on Love wave sensors for liquid characterization appeared in USA not earlier than in 1992 [6], but nowadays, we witness about 100 publications per year on that subject [7].

We hope that the reader, after studying this chapter, will agree that the nature has many different faces and that the same physical phenomenon can be sometimes deadly (earthquakes) and in different circumstances, can be beneficiary (biosensor technology). As a consequence, SH surface waves of the Love type are an interesting example of an interdisciplinary research.

This chapter is organized as follows. Section 2 presents main characteristics and properties of Love surface waves, including basic mathematical model and examples of dispersion curves and amplitude distributions. More advanced mathematical treatment of the Love surface waves can be found, for example, in [8]. Section 3 shows the importance of Love surface waves in geophysics and seismology. Section 4 describes applications of Love surface waves in biosensors used in biology, medicine, chemistry, etc. Section 5 contains discussion of the chronological development of SH ultrasonic sensors starting from bulk wave sensors and then first surface

wave sensors. We show also that the results of research conducted in Seismology and geophysics can be transferred to biosensor technology and vice versa. Conclusions and propositions for future research in biosensor technology employing Love surface waves are given in Section 6.

In addition to biosensors, Love surface waves are used in chemosensors, in non-destructive testing (NDT) of materials, and in sensors of various physical quantities such as:

1. humidity of air [9];
2. spatial distribution of elastic parameters in solid functionally graded materials (FGM) [10];
3. elastic parameters of nanolayers [11];
4. porosity of the medium [12]; and
5. dielectric constant of liquids [13].

Recently, Love surface waves were also employed in the construction of the magnetic field sensor system with outstanding characteristics (sensitivity, dynamic range, etc.) [14].

2. Properties of Love surface waves

Shear horizontal (SH) surface waves of the Love type are elastic waves propagating in a surface waveguide, which is composed of a surface layer rigidly bonded to an elastic substrate, see **Figure 1**. The existence of an elastic surface layer is a necessary condition for propagation of Love surface waves, since it can be easily shown that on an elastic half-space alone, SH

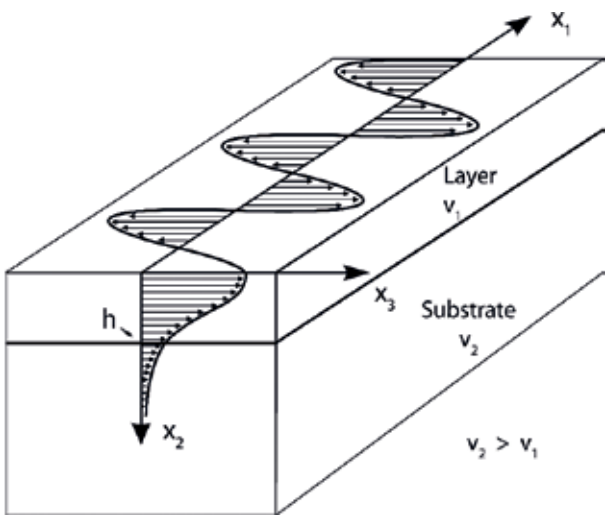

Figure 1. Basic structure of a free Love wave waveguide, not loaded with a viscoelastic liquid. An elastic surface layer of thickness "h" and a shear velocity v_1 is rigidly bonded to the underlying semi-infinitive substrate with a shear velocity v_2.

surface waves cannot exist. The extra surface layer must also be "slower" than the substrate, i.e., the following condition must hold [15]:

$$v_1 < v_2 \tag{1}$$

where v_1 and v_2 are phase velocities of bulk shear waves in the surface layer and substrate, respectively. In fact, the condition expressed by Eq. (1) allows for entrapment of partial waves in the surface layer due to the total reflection phenomenon occurring at the layer-substrate interface ($x_2 = h$). By contrast, if the condition given by Eq. (1) is not satisfied ($v_1 > v_2$), then Love waves are evanescent in the direction of propagation x_1 and, on average, no net power is transmitted along the surface waveguide.

2.1. Dispersion equation of the Love surface wave

Mechanical displacement u_3 of a time-harmonic Love surface wave propagating in the direction x_1 has the following form:

$$u_3(x_1, x_2, t) = f(x_2)\, exp\left[j(k\, x_1 - \omega t)\right] \tag{2}$$

where the function $f(x_2)$ describes the amplitude of the Love wave as a function of the depth (x_2 axis), $k = \omega/v_p$ is the wavenumber of the Love wave, $\omega = 2\pi f$ is its angular frequency, v_p is the phase velocity of the Love wave and $j = \sqrt{-1}$. Since the surface waveguide is assumed to be lossless, the wavenumber k in Eq. (2) is a real quantity.

Substitution of Eq. (2) into Newton's equation of motion leads to the Helmholtz differential equation for the transverse amplitude $f(x_2)$. Solutions of the resulting Helmholtz differential equation have the following form [16]:

$$f(x_2) = \begin{cases} A\,\dfrac{cos(q_1\, x_2)}{cos(q_1\, h)}, & for\ 0 \le x_2 < h\ (surface\ layer) \\ A\, e^{-q_2(x_2-h)}, & for\ h \le x_2\ (substrate) \end{cases} \tag{3}$$

where

$$\begin{aligned} q_1^2 &= k_1^2 - k^2 \\ -q_2^2 &= k_2^2 - k^2 \end{aligned} \tag{4}$$

$$\begin{aligned} k_1^2 &= \frac{\omega^2}{v_1^2} \\ k_2^2 &= \frac{\omega^2}{v_2^2} \end{aligned} \tag{5}$$

and A is an arbitrary constant. In isotropic solids, Love surface waves have two stress components, τ_{23} *and* τ_{13}, associated with the SH displacement u_3. From Eq. (3), it follows that stress τ_{23} can be expressed by the following formula:

$$\tau_{23}(x_2) = \mu_{1,2}\frac{\partial f(x_2)}{\partial x_2} = \begin{cases} -\mu_1 q_1 A\dfrac{\sin(q_1 x_2)}{\cos(q_1 h)}, & for\ 0 \le x_2 < h\ (surface\ layer) \\ -\mu_2 q_2 A\, e^{-q_2(x_2-h)}, & for\ h \le x_2\ (substrate) \end{cases} \tag{6}$$

where μ_1 *and* μ_2 are shear moduli of elasticity in the surface layer and substrate, respectively.

The mechanical displacement u_3 and the associated stress τ_{23} must satisfy the appropriate boundary conditions, i.e., the continuity of u_3 and τ_{23} at interfaces $x_2 = 0$ (free guiding surface) and $x_2 = h$ (the interface between the surface layer and the substrate). Substituting Eqs. (3) and (6) into the boundary conditions at $x_2 = 0$ and $x_2 = h$, one obtains the following dispersion relation [16], for Love surface waves propagating in a planar waveguide shown in **Figure 1**:

$$F[\omega, k(\omega)] = \mu_1 q_1 \tan(q_1 h) - \mu_2 q_2 = 0 \tag{7}$$

Using Eq. (4), one can rewrite Eq. (7) in a more explicit form as:

$$F[\omega, k(\omega)] = \mu_1\left(\sqrt{\frac{1}{v_1^2}-\frac{1}{v_p^2}}\right)\tan\left[2\pi\left(\sqrt{\frac{1}{v_1^2}-\frac{1}{v_p^2}}\right)(fh)\right] - \mu_2\left(\sqrt{\frac{1}{v_p^2}-\frac{1}{v_2^2}}\right) = 0 \tag{8}$$

Eq. (8) shows that the unknown phase velocity v_p of the Love surface wave is de facto an explicit function of the normalized product frequency-thickness (fh), with v_1 and v_2, being parameters. This property does not, however, hold for lossy Love wave waveguides where the elastic moduli μ_1, μ_2 as well as the velocities v_1 and v_2 are implicit functions of the frequency f and are obviously independent of the surface layer thickness h.

The dispersion relation Eq. (8) is a transcendental algebraic equation for the unknown phase velocity v_p and therefore can be solved only numerically using, for example, the Newton-Raphson iterative method [17].

2.2. Modal structure of the Love surface wave

The dispersion relation [Eq. (8)] reveals that phase velocity v_p of the Love surface wave is a function of frequency. Hence, Love surface waves are dispersive. Moreover, since the function tangent in Eq. (8) is periodic, i.e., $\tan(q_1 h) = \tan(q_1 h + n\pi)$, where $n = 0, 1, 2, \ldots$, etc., Love surface waves display a multimode structure.

The amplitude $f(x_2)$ of the fundamental $(n = 0)$ mode of the Love surface wave, as a function of the distance x_2 from the guiding surface $x_2 = 0$, is shown in **Figure 2**. It is clear that for sufficiently high frequencies, the energy of the Love wave is concentrated mostly in the surface layer in the vicinity of the guiding surface $x_2 = 0$. By differentiation of Eq. (3), it is easy to show that the maximum of the amplitude $f(x_2)$ occurs exactly at the free surface $x_2 = 0$. By contrast, the associated stress τ_{23} vanishes at $x_2 = 0$, i.e., at the free surface of the waveguide.

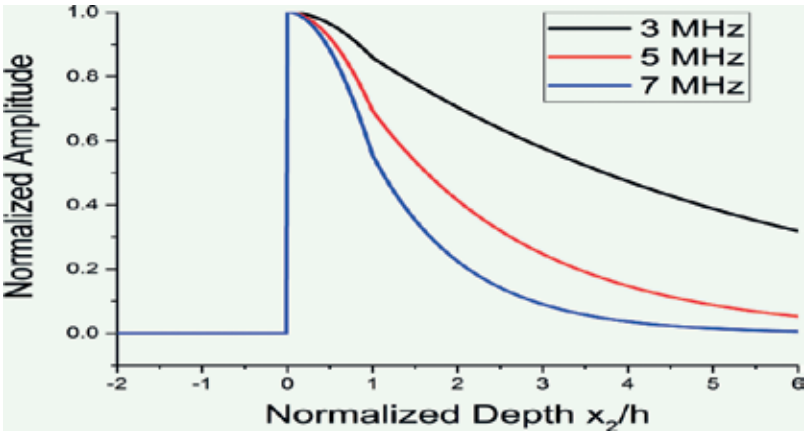

Figure 2. Amplitude of the fundamental (n = 0) Love wave mode, as a function of the normalized depth x_2/h, in a copper-steel waveguide, for different wave frequencies f = 3, 5, and 7 MHz, and surface layer thickness h = 100 μm.

2.3. Phase and group velocity of the Love surface wave

The total derivative of the implicit function $F[\omega, k(\omega)]$ in the dispersion relation [Eq. (7)] with respect to the angular frequency ω equals:

$$\frac{\partial}{\partial \omega} F[\omega, k(\omega)] + \frac{\partial}{\partial k} F[\omega, k(\omega)] \frac{dk(\omega)}{d\omega} = 0 \tag{9}$$

Since group velocity v_g of the Love surface wave, which describes the speed at which pulse envelope of the Love surface wave propagates, is defined as $\frac{d\omega}{dk}$ from Eq. 9, it is clear that:

$$v_g = \frac{d\omega}{dk} = -\frac{\frac{\partial}{\partial k} F[\omega, k(\omega)]}{\frac{\partial}{\partial \omega} F[\omega, k(\omega)]} \tag{10}$$

As a consequence, using Eqs. (7) and (10), one can show [8, 15–19] that group v_g and phase v_p velocities of the Love surface wave are connected via the following algebraic equation:

$$\frac{v_g v_p}{v_2^2} = \frac{\mu_1 q_2 h \left[\frac{\sin(2 q_1 h)}{2 q_1 h} + 1\right] + \mu_2 \cos^2(q_1 h)}{\mu_1 q_2 h \left(\frac{v_2}{v_1}\right)^2 \left[\frac{\sin(2 q_1 h)}{2 q_1 h} + 1\right] + \mu_2 \cos^2(q_1 h)} \tag{11}$$

Eqs. (7) and (11) show that phase v_p and group v_g velocities of the Love surface wave in the low ($f \to 0$) and high ($f \to \infty$) frequency limits are the same and equal, respectively, v_2 and v_1.

The phase velocity resulting from the solution of Eq. (8) and the group velocity determined by Eq. (11) of the fundamental mode of Love surface waves, as a function of the normalized frequency fh, are given in **Figure 3**. From **Figure 3**, it is evident that for low frequencies, the

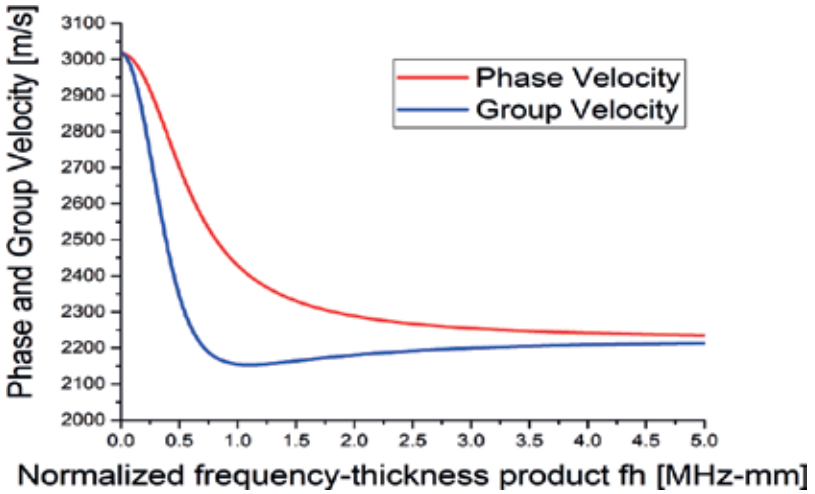

Figure 3. Phase v_p and group v_g velocities of the fundamental mode of the Love surface wave propagating in a copper-stainless steel waveguide, as a function of the normalized frequency-thickness product fh [MHz-mm], $v_1 = 2223.5\ m/s$, and $v_2 = 3017\ m/s$.

phase and group velocities of Love surface waves approach asymptotically that of bulk shear waves v_2 in the substrate. On the other hand, at high frequency limit, the phase and group velocities of the Love wave tend to the velocity v_1, namely to the velocity of bulk shear waves in the surface layer.

2.4. Influence of a viscoelastic liquid loading Love wave waveguides

It is noteworthy that in waveguides loaded with a lossy, viscoelastic liquid, the wavenumber k of the Love surface wave is a complex quantity, i.e., $k = \omega/v_p + j\alpha$, where α is the coefficient of attenuation of the Love wave. Three most popular viscoelastic liquids are described by Kelvin-Voigt, Newton and Maxwell models, respectively [20]. The dispersion relation of Love surface waves propagating in waveguides loaded with a viscous liquid can be found in [21]. In lossy waveguides, the group velocity of Love waves cannot be rigorously defined [22]. As a result, the formula 11 is valid only approximately in lossy Love wave waveguides. As a matter of fact, in a waveguide loaded with a viscoelastic liquid, the amplitude of the Love wave is non-zero in a thin layer of the liquid adjacent to the surface layer of the waveguide. The penetration of the Love wave energy into the adjacent liquid is of crucial importance in understanding the operation of Love wave biosensors. Indeed, if Love wave energy was not penetrating in the measured liquid, the parameters of the Love wave might not be affected by the liquid and the operation of the whole sensor would be essentially impossible.

3. Love surface waves in seismology

Since Love surface waves were originally discovered in seismology, we give here a brief description of their applications in seismic and geophysical research.

Propagation of Love surface waves on the Earth's surface is made possible by layered structure of the Earth. The outermost layer of the Earth, the crust, is made of solid rocks composed of lighter elements. Thickness of the crust varies from 5 to 10 km under oceans (oceanic crust) to 30–70 km under continents (continental crust). The crust sits on mantle, which in turn covers the outer and inner core. The destructive power of earthquakes is mainly due to waves traveling in this thin crustal layer [23].

As predicted by Love, the velocity of SH bulk waves increases with depth [24], i.e., as a function of distance from the free surface of the Earth.

The frequency of Love waves generated by earthquakes is rather low comparing to that used in sensor technology and ranges typically from 10 mHz to 10 Hz.

3.1. Investigation of the Earth's interior with Love surface waves

Love and Rayleigh surface waves travel along great circle paths around the globe. Surface waves from strong earthquakes may travel several times around the Earth without a significant attenuation. They are termed global Rayleigh wave impulses [25]. An example of surface waves traveling multiply around the Earth [26] is given in **Figure 4**.

Seismic waves, generated both by natural earthquakes and by man-made sources, have delivered an enormous amount of information about the Earth's interior (subsurface properties of Earth's crust). In classical seismology, Earth is modeled as a sequence of uniform horizontal layers (or spherical shells) having different elastic properties and one determines these properties from travel times and dispersion of seismic waves [27].

Love surface waves have been successfully employed in a tomographic reconstruction of the physical properties of Earth's upper mantle [28] as well as in diamond, gold, and copper exploration in Australia, South America, and South Africa [29].

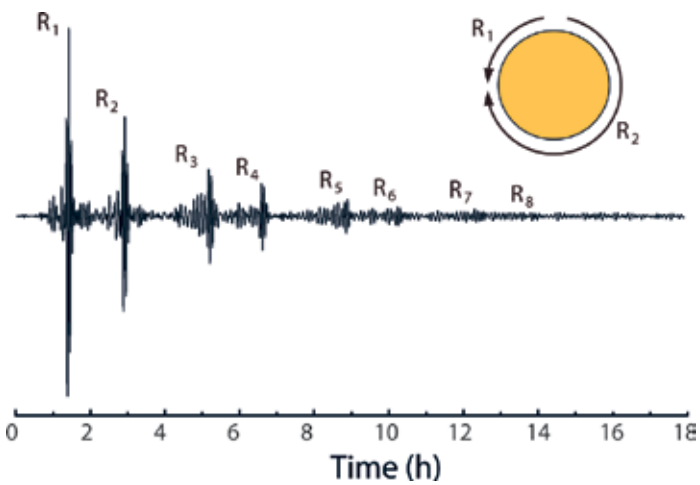

Figure 4. Illustration of a seismogram of Rayleigh surface waves triggered by an earthquake. Note that, Rayleigh wave packet traveled 8 times around the Earth's circumference.

Surface waves generated by earthquakes or man-made explosions were used in quantitative recovery of Earth's parameters as a function of depth. These seismic inverse problems helped to discover many fine details of the Earth's interior [30–32].

It is noteworthy that many theoretical methods were initially originated in seismology and geophysics before their transfer to the surface wave sensor technology (see **Table 1** in Section 5.5).

3.2. Structural damages due to Love surface waves generated by earthquakes

An example of structural damages made by surface waves of the Love type is shown in **Figure 5**. It is apparent that railway tracks were deformed by strong shear horizontal SH forces parallel to the Earth's surface. Love surface waves together with Rayleigh surface waves are the most devastating waves occurring during earthquakes.

3.3. Application of metamaterials to minimize devastating effects of Love surface waves in the aftermath of earthquakes

It is interesting to note that recently developed earthquake engineered metamaterials open a new way to counterattack seismic waves [33, 34]. The metamaterials actively control the seismic waves by providing an additional shield around the protected building rather than reconstructing the building structure. Compared with common engineering solutions, the advantage of the metamaterial method is that it can not only attenuate seismic waves before they reach critical targets, but also protect a distributed area rather than an individual building. The

Developments	Seismology	Biosensors
Basic theory	Love [1]	Kiełczyński [3]
Multilayered waveguides (transfer matrix method)	Haskell [72]	Kiełczyński [8]
Viscoelastic waveguides (theoretical analysis)	Sezawa [73]	Kiełczyński [74]
Inverse problems	Dorman [76]	Kiełczyński [77]
Nonlinear waves	Kalyanasundarm [78]	—
Phased arrays	Frosch [79]	—
Tomography	Nakanishi [80]	—
Higher-order modes	Haskell [81]	—
Solitary waves	Bataille [82]	—
Energy harvesting	Qu [83]	—
Waveguides with nanomaterials	—	Penza [84]
Piezoelectric waveguides	—	Kovacs [6]
Resonators	—	Kovacs [67]
Delay lines	—	Tournois [19]

Table 1. Chronology of developments in Love wave biosensors and Love wave seismology.

Figure 5. Twisted railroad tracks, an example of structural damages due to SH displacement of Love surface waves in the aftermath of an earthquake.

periodic arrangement of metamaterial structure creates frequency band gaps, which effectively prevent surface waves propagation on the Earth's surface via a Bragg scattering mechanism.

4. Biosensors employing Love surface waves

A biosensor can be described as a device which can generate a signal (usually electrical) that is proportional to the concentration of a particular biomaterial or chemicals in the presence of a number of interfering species [35]. This can be accomplished using biological recognition elements such as enzymes, antibodies, receptors, tissues, and microorganisms as sensitive materials because of their selective functionality for target analytes along with an appropriate transducer.

4.1. Confinement of the energy of Love surface waves near the free surface of the waveguide

High sensitivity of Love surface wave sensors can be explained by spatial concentration of the energy of Love waves. Indeed, it was shown in Section 2 that the energy of Love surface waves is localized mostly in the vicinity of the free guiding surface (**Figure 1**), looking in both sides from it. Moreover, the amplitude of Love surface waves reaches maximum at the free guiding surface $x_2 = 0$ (**Figure 2**). Therefore, we can expect that propagation of Love surface waves will be to a lesser or higher extent perturbed by a material (such as liquid) being in contact with the guiding surface. This feature of Love waves was exploited in the construction of various biosensors used for detection and quantification of many important parameters of biological and chemical substances [21, 36–40].

4.2. Correlation between concentration of the measured analyte and parameters of the Love surface wave

Surface waves of the Love type are especially suited to measure parameters of viscoelastic liquids, polymers, gels, etc., providing that they can form a good mechanical contact

(absorption and adhesion) with free surface of the waveguide. Since Love surface waves are, in principle, mechanical waves, they can measure the following mechanical parameters of an adjacent medium: density, modulus of elasticity, and viscosity. In waveguides composed of piezoelectric elements (substrate and/or surface layer), dielectric constant of the adjacent medium will also affect the propagation of Love surface waves. In practice, we are interested in detection and quantification other more specific properties of biological and chemical materials, such as concentration and presence of proteins, antibodies, toxins, bacteria, viruses, size and shape of DNA, etc. Therefore, the next step in the development of Love wave sensors is to correlate (experimentally or analytically) the abovementioned specific properties of the measured analytes with changes in density, viscosity, and elastic moduli of the surface (sensing) layer. Finally, we have to measure changes in phase velocity and attenuation of Love surface waves, which are due to changes in density, viscosity, and elastic moduli of this surface layer. It should be noticed that part of Love wave energy enters into the measured liquid to some distance (penetration depth) from the guiding surface. Such an energy redistribution changes certainly the phase velocity and attenuation of the Love surface wave. In practice, we often adopt a more empirical approach, i.e., we measure directly changes in phase velocity and attenuation of Love waves, as a function of the aforementioned specific properties of the measured material, such as the concentration of proteins and so on, without referring to changes in density, viscosity or elastic modulus of the measured material. However, the former step is indispensable during modeling, design, and optimization of Love surface wave sensors.

4.3. Parameters of the Love surface wave measured

As with other types of wave motion, we can measure in principle two parameters of Love surface waves, i.e., their phase and amplitude. Polarization of SH surface waves of the Love type is constant and therefore does not provide any additional information about the medium of propagation. Phase $\Phi(x_1, t)$ measurements in radians are directly related to the phase velocity v_p of Love surface waves via the following equation:

$$\Phi(x_1, t) = k x_1 - \omega t = \omega\left(\frac{x_1}{v_p} - t\right) \tag{12}$$

Similarly, amplitude A measurements are correlated with the coefficient of attenuation α (in Np/m) of Love surface waves as follows:

$$\alpha = \frac{1}{(x_2 - x_1)} ln\left(\frac{A_1}{A_2}\right) [Np/m] \tag{13}$$

where A_1 and A_2 are two amplitudes of the wave measured at points x_1 and x_2, respectively ($x_2 > x_1$). In order to obtain the coefficient of attenuation in dB/m, the coefficient α given by Eq. (13) must be multiplied by $20\,log(e) \approx 8.686$.

4.4. Sensors working in a resonator and delay line configurations

Phase and amplitude characteristics of Love surface waves can be measured in a closed loop configuration by placing Love wave delay line in a feedback circuit of an electrical oscillator (resonator). Another possibility is to use network analyzer, which provides phase shift and insertion loss of the Love wave sensor working in an open loop configuration, due to the load of the sensor with a measured material. The typical frequency range used by Love wave sensors is from 50 MHz to 500 MHz [7].

The structure and cross section of a typical Love wave biosensor is shown in **Figure 6a** and **b**. A relatively thick (0.5–1.0 mm) substrate provides mechanical support for the whole sensor. Often the substrate material is piezoelectric (AT-cut quartz material [41]). In this case, a pair of interdigital transducers (IDTs) can be deposited on the substrate to form a delay line of the sensor. The guiding layer (SiO_2, ZnO, PMMA, etc.), deposited directly on the substrate, provides entrapment for surface wave energy. The sensing layer, made of gold (Au) or a polymer, usually very thin (~50-100 nm), serves as an immobilization area for the measured biological material. This thin-sensing layer interacts directly with the measured material (liquid) and serves often as a selector of the specific target substance, such as antigen, to be measured.

4.5. Sensors controlled remotely by wireless devices

An interesting solution for Love wave sensors was proposed in [42], where the Love wave sensor works in a wireless configuration without an external power supply. This design has many unique advantages, i.e., the sensor can be permanently implanted in a patient body to monitor continuously the selected property of a biological liquid. Readings of the sensor can be made on demand, totally noninvasively by a reading device connected to a broader computer system of patient monitoring. Another implementation of a remotely controlled wireless Love wave sensor was presented in [43]. The proposed sensor can measure simultaneously two different analytes using Love surface waves with a frequency of 440 MHz.

Wireless bioelectronics sensors may be used in a variety of fields including: healthcare, environmental monitoring, food quality control, and defense.

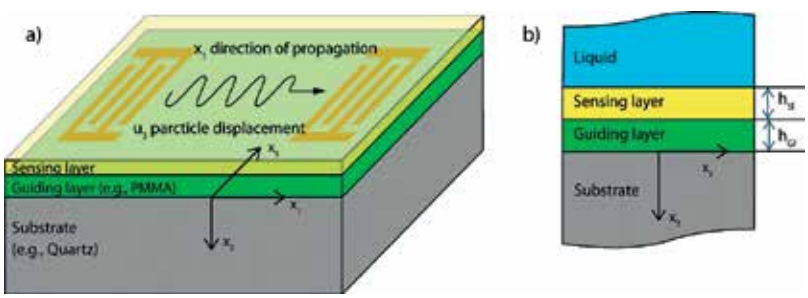

Figure 6. a) Layered structure of a typical Love wave sensor not yet connected to the external driving circuit and b) cross-section of this sensor structure + loading liquid.

4.6. Examples of laboratory and industrial grade Love wave sensors

To apply the measured analyte to the Love wave sensor, the sensor is often equipped with a flow cell, which separates interdigital transducers from sensing area of the waveguide [44]. A laboratory grade Love wave sensor equipped with a flow cell is shown in **Figure 7**.

A prototype of an commercial ready Love wave sensor was presented in 2015 in Ref. [45]. A 250 MHz delay line Love wave immunosensor was designed on the ST quartz substrate with a thin gold layer of thickness ~90 nm used as a guiding and sensing area, for antibodies or antigens can be easily immobilized on a gold surface. The changes of Love wave velocity and attenuation were due to antibodies-antigens interactions. A disposable test cassette with embedded Love wave immunosensor is connected to a handheld electronic reader, which in turn is connected wirelessly via bluetooth to a smartphone or a computer. This device is a strong candidate for clinical and personnel healthcare applications.

4.7. Examples of analytes measured by Love wave biosensors

Love wave biosensors have been used in measurement and detection of a large number of substances (analytes) [44]. As representative examples, we can mention the following:

- concentration of bovine serum albumin [46];
- real-time detection of antigen-antibody interactions in liquids (immunosensor) [47];
- simultaneous detection of Legionella and *E. coli* bacteria [48];
- virus and bacteria detection in liquids [49];
- detection of pathogenic spores *Bacillus anthracis* below inhalation infectious levels [50];
- investigation of lipid specificity of human antimicrobial peptides [51];
- Sin Nombre Virus detection at levels lower than those typical for human patients suffering from hantavirus cardiopulmonary syndrome [52];

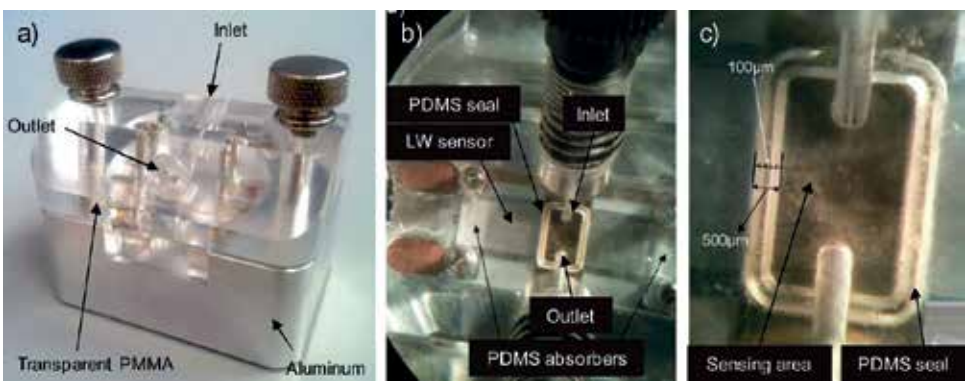

Figure 7. An example of a laboratory grade Love wave sensor with a flow cell [42].

- detection of nanoparticles in liquid media [53];
- okadaic acid detection [54];
- study of protein layers [55];
- antibody binding detection [56];
- toxicity of heavy metals [57];
- size and shape of DNA [58];
- real-time detection of hepatitis B [59];
- liquid chromatography [60];
- immunosensors for detection of pesticide residues and metabolites in fruit juices [61];
- detection of cocaine [62]; and
- detection of carbaryl pesticide [63].

4.8. Desired characteristics (features) of industrial grade Love wave sensors

This rather impressive list of achievements in R&D activities on biosensor technology suggests that biosensors employing Love surface waves have a huge potential. However, in order to compete with other types of biosensors, such as optical sensors based on the surface plasmon resonance [64], the biosensors employing Love surface waves should possess the following characteristics:

- high sensitivity to the measured property (measurand);
- high selectivity to the measured property (measurand);
- low limit of detection;
- zero temperature coefficient (high-thermal stability);
- high repeatability and stability;
- possibility of multiple reuse; and
- cost-effectiveness.

At present, none of the above targets have been fully achieved. Love wave biosensors are, in general, still in the laboratory research phase, where most developments are focused on the proof of concept and construction of a working prototype. Only one European company offers today commercially available Love wave sensors [7]. Nevertheless, as it was shown in this section, Love wave biosensors can be used to measurements of a surprisingly large number of biological substances (analytes) with a quite remarkable accuracy and sensitivity. Therefore, in our opinion, Love wave biosensors will reach soon an industrial grade level with numerous real-life applications in biology, medicine (clinical practice), and chemistry.

5. Discussion

5.1. Older sensors using bulk SH waves

It is interesting to note that first acoustic sensors for measurements of viscoelastic properties of liquids used to this end bulk (not surface) SH waves propagating in a solid buffer, loaded on one side with a measured viscoelastic liquid. This idea appeared in 1950 in works of such prominent ultrasonic scientists Mason and McSkimmin [65]. However, the main drawback of the bulk wave sensors was their inherent low sensitivity. For example, to perform measurements with a water-loaded sensor, one had to observe about 50 consecutive reflections in the solid buffer.

5.2. Emergence of new sensors using SH surface waves of the Love type

The breakthrough came with a proposition to employ to this end SH surface waves of the Love and Bleustein-Gulyaev types. This idea was first articulated by Kiełczyński and Płowiec in 1981 in their Polish patent no 130040 [2]. In 1987, the theory of the new method was presented by Kiełczyński and Pajewski on the international arena at the European Mechanics Colloquium 226 in Nottingham, UK [3]. In 1988, this new method, with equations and experimental results, was presented by Kiełczyński and Pajewski at IEEE 1988 Ultrasonic Symposium in Chicago [4]. In 1989, Kiełczyński and Płowiec published detailed theory and experimental results in the prestigious Journal of the Acoustical Society of America [5]. Their theory [3–5] was based on the Auld's perturbative technique [66] and gave satisfactory results for liquids of viscosities up to ~10 Pas. The main advantage of the Love surface wave sensors is their very high sensitivity, namely the sensitivity of a few orders of magnitude (10^2 to 10^4) higher than that of their bulk SH waves counterparts [3–5]. As a result, measurements of the viscosity of water (~1 mPas) and other biological substances (based largely on water) was no longer a challenge, what was the case with bulk SH wave sensors. In other words, due to the employment of SH surface waves, the way for development of the corresponding biosensors was widely open.

It should be noticed that next publications on the Love wave sensors for liquid characterization appeared in the open literature not earlier than in 1992 [6]. In fact, in papers published in 1992, Kovacs and Venema [67], and, in 1993, Gizeli et al. [68] confirmed our earlier discovery [3–5] that Love surface waves are much more sensitive to viscous loading than other types of SH waves. In another paper published in 1992, Gizeli et al. [69] developed theoretical analysis for Love wave sensors, using the same Auld's perturbative technique [66] as that employed by us in papers [3–5].

It is interesting to note that two other types of SH waves, i.e., leaky SH SAW waves and plate SH waves, were also tried to measure viscosity of liquids. Leaky SH SAW waves were proposed in 1987 [70] by Moriizumi et al. and SH plate waves in 1988 by Martin et al. [71]. However, these two types of SH waves were quickly abandoned, since the corresponding

viscosity sensors were of inherently low sensitivity, difficult in practical realization and difficult in theoretical analysis (leaky SH SAW waves). In fact, the energy of SH plate waves is uniformly distributed across the whole thickness of the plate. Therefore, SH plate waves are not so sensitive to viscous loading as Love surface waves, whose energy is highly concentrated in the surface layer of the waveguide. On the other hand, leaky SH SAW waves are not pure SH waves and contains in principle all three components of vibrations, not only the SH one. In particular, the component perpendicular to free surface of the waveguide will continuously radiate energy into the adjacent liquid. This will cause an additional attenuation for leaky SH SAW waves, which will be indistinguishable from that due to the viscous loading measured.

5.3. Mathematical apparatus and numerical methods used in analysis of Love surface waves

R&D activities in seismology and biosensor technology using Love surface waves focus inevitably on different problems and challenges. The main reason for these differences is the nature and scale of Love surface waves used in seismology and biosensor technology, i.e., in seismology, they are a natural phenomenon and in biosensors, they are controlled within man-made devices. It is instructive to compare the chronology of developments made in seismology and in biosensor technology (see **Table 1**). In fact, the theory of Love waves published in 1911 [1] was developed for the simplest surface wave waveguide, namely for that composed of linear, isotropic, and lossless materials (surface layer on a substrate). Since loading viscoelastic liquids are always lossy, the corresponding theory of Love wave sensors had to use perturbative [3] or numerical methods [37]. The theory of Love waves in multilayered waveguides, developed in Seismology [72], uses a conventional transfer-matrix method based on the elementary matrix algebra. By contrast, the theory developed for biosensors extends the transfer-matrix method to a more advanced formalism of matrix differential equations with eigenvectors and eigenvalues and operator functions [8]. First theories of Love waves propagating in viscoelastic waveguides, were developed in Seismology [73], long before the advent of modern fast digital computers. By contrast, the corresponding theory developed for biosensors [74] in 2016 heavily relates on numerical methods.

5.4. Milestones in developments of Love wave seismology and Love wave biosensors

Examination of **Table 1** reveals that a number of R&D activities already well established in Seismology were not yet initiated in biosensor technology. As examples, one can mention the applications of nonlinear Love waves, higher-order Love wave modes or solitary waves. This suggests that in future research, it may be advantageous to employ higher-order modes, nonlinear Love waves, metamaterials, etc., to increase biosensors sensitivity [75] or lower their limit of detection. Other technologies not yet used in biosensor technology are phased array

and tomography. Indeed, applied to biosensors they may allow for a 2D characterization of the analyte distribution, electronic beam steering, focusing, etc. These indications for future research in biosensor technology show clearly advantages of multidisciplinary R&D activities, in this case seismology and biosensor technology. Indeed, it is much easier to adapt an existing technology already developed in other fields to a new domain than to invent a new technology from scratch without any prior feedback.

5.5. Novelty of the present chapter

Despite the fact that the first theory of Love surface waves was published as early as in 1911 [1], surprisingly, a large number of problems concerning the theory of Love surface waves have not yet been solved.

This chapter contains theoretical foundations and calculation results regarding the propagation of the Love wave in various media. A new interpretation of the Love wave dispersion equation was given. This equation is presented in the form of an implicit function of two variables, i.e., (ω, k). This allowed to evaluate the analytical dependencies on group velocity of Love wave propagating in a wide class of layered waveguides, e.g., in graded waveguides. This problem will be the subject of future author's works.

The obtained results can be employed in the design and optimization of not only biosensors but also chemosensors and sensors of physical quantities that use Love waves. In addition, the obtained results can be used in seismology and geophysics for the interpretation of seismograms and determining the distribution of elastic parameters of the Earth's crust.

This chapter contains also a novel comparison of milestones in developments made in Love wave seismology and Love wave biosensors (see Section 5.4). Since Love wave biosensors appeared exactly 70 years [2] after emergence of Love surface waves in seismology [1], it is not surprising that many discoveries and developments were made first in seismology and then transferred to biosensors (see **Table 1**). This cross-pollination between the two seemingly distant branches of science is very beneficial and can significantly accelerate developments made in either of them.

6. Conclusions

In this limited space chapter, it was impossible to address or even mention all interesting problems relevant to the properties and applications of Love surface waves in seismology and biosensor technology. Instead, we tried to present only main properties of the Love surface waves, such as their dispersive nature, phase and group velocities, amplitude distribution, etc., as well as their most iconic applications in seismology and biosensor technology. We think that presentation of the Love surface waves R&D activities in a broader historical

perspective gives an invaluable insight in the process of developments made in this fascinating interdisciplinary domain of research.

In this chapter, we attempted to present a variety of aspects that can be attributed to SH surface waves of the Love type. As a matter of fact, Dr. Jekyll and Mr. Hyde Love surface waves possess simultaneously two diametrically different faces, i.e., first benign (biosensors) and second deadly (earthquakes). The good news is that developments made in one of these domains can be easily transferred to the second one and vice versa. In fact, Love surface waves were first discovered in seismology (1911). They finally enabled for precise interpretation of seismograms registered in the aftermath of earthquakes. Beneficiary applications (biosensors) of Love surface waves were announced exactly 70 years later (1981) in a Polish patent.

Since earthquake is a natural phenomenon, we have little or no influence on its occurrence and dynamics. By contrast, the construction and the operation of biosensors can be optimized by mathematical modeling and experimental studies. At present, the mathematical modeling of Love wave biosensors is an active domain of research. On the other hand, progress in electronics and computer technology will lead to development of new compact and reliable instrumentation working in conjunction with Love wave biosensors.

Despite their centennial heritage, Love surface waves are subject of an intensive research activity. For example, one can mention the application of inverse problem techniques to recover material parameters of surface layers from measurements of velocity and attenuation of Love surface waves. Inverse problem techniques have been successfully employed in seismology and geophysics [25] and recently also pioneered by the authors [74, 77, 85] and others [86, 87] in the biosensor technology.

Other open problems in the theory and technique of Love surface waves are non-linear Love waves, extremely slow Love waves [88], Love waves in layered nanostructures [89], energy harvesting with Love waves, and metamaterial-based seismic shielding, [33, 34], etc.

Finally, coming back to the idea expressed at the beginning of the introduction in this chapter, we want to assure the reader that there exist still many significant unresolved problems in the theory and technique of the Love surface waves, which deserve to be addressed in future R&D activities. We hope that this chapter may be helpful in this endeavor.

Author details

Piotr Kiełczyński

Address all correspondence to: pkielczy@ippt.pan.pl

Institute of Fundamental Technological Research, Polish Academy of Sciences, Warsaw, Poland

References

[1] Love AEH. Some Problems of Geodynamics. UK: Cambridge University Press; 1911. pp. 89-104 and 149-152

[2] Kiełczyński P, Płowiec R. Polish patent no. 130040; 1981

[3] Kiełczyński P, Pajewski W. Determination of the rheological parameters of viscoelastic liquids using shear surface waves. In: Parker DF, Maugin GA, editors. Recent Developments in Surface Acoustic Waves. In: Proceedings of European Mechanics Colloquium 226; University of Nottingham, UK; Springer Series on Wave Phenomena 7; September 2-5, 1987. Berlin: Springer-Verlag; 1988. pp. 317-321

[4] Kiełczyński P, Pajewski W. A new method for the determination of the shear impedance of viscoelastic liquids. IEEE1988 Ultrasonic Symposium Proceedings; USA. 1988. pp. 323-326

[5] Kiełczyński P, Płowiec R. Determination of the shear impedance of viscoelastic liquids using Love and Bleustein-Gulyaev surface waves. Journal of Acoustical Society of America. August 1989;**86**(2):818-827

[6] Kovacs G, Lubking GW, Vellekoop MJ, Venema A. Love waves for (bio)chemical sensing in liquids. In: Ultrasonics Symposium Proceedings; IEEE; Tucson, USA. 1992. pp. 281-285

[7] Gronewold TMA. Surface acoustic wave sensors in the bioanalytical field: Recent trends and challenges. Analytica Chimica Acta. 2007;**603**:119-128

[8] Kiełczyński P, Szalewski M, Balcerzak A, Wieja K. Propagation of ultrasonic love wave in non-homogeneous elastic functionally graded materials. Ultrasonics. 2016;**65**:220-227

[9] Lan XD, Zhang SY, Fan L, Wang Y. Simulation of SAW humidity sensors based on $(11\bar{2}0)$ ZnO/R-sapphire structures. Sensors. 2016;**16**:1112. DOI: 10.3390/s16111112

[10] Kiełczyński P, Szalewski M, Balcerzak A, Wieja K. Group and phase velocity of Love waves propagating in elastic functionally graded materials. Archives of Acoustics. 2015;**40**:273-281

[11] Zhang S, Gu B, Zhang H, Feng XQ, Pan R, Alamusi, Hu N. Propagation of Love waves with surface effects in an electrically-shorted piezoelectric nanofilm on a half-space elastic substrate. Ultrasonics. 2016;**66**:65-71

[12] Wang YS, Zhang ZM. Propagation of Love waves in a transversely isotropic fluid-saturated porous layered half-space. Journal of the Acoustical Society of America. February 1998;**103**(2):695-701

[13] Xia Q, Chen Z, Wang M. The system design of a love wave sensor for measuring liquid dielectric constant. IEEE International Ultrasonics Symposium (IUS); 18-21 October 2011; Orlando, FL, USA. DOI: 10.1109/ULTSYM.2011.0571

[14] Kittmann A, Durdaut P, Zabel S, Reermann J, Schmalz J, Spetzler B, Meyners D, Sun NX, McCord J, Gerken M, Schmidt G, Höft M, Knöchel R, Faupel F, Quandt E. Wide band low noise love wave magnetic field sensor system. Scientific Reports. 2018;**8**:278. DOI: 10.1038/s41598-017-18441-4

[15] Auld BA. Acoustics Fields and Waves in Solids, Vol. II. Florida: Krieger Publishing Company; 1990. p. 95

[16] Royer D, Dieulesaint E. Elastic Waves in Solids I. Berlin: Springer; 2000. p. 306

[17] Press WH, Teukolsky SA, Vetterling WT, Flannery BP. Numerical Recipies. 3rd ed. New York: Cambridge Univeristy Press; 2007. p. 456

[18] Kiełczyński P, Szalewski M, Balcerzak A, Wieja K. Group and phase velocities of Love waves propagating in elastic functionally graded materials. Archives of Acoustics. 2015;**40**(2):273-281

[19] Tournois P, Lardat C. Love wave-dispersive delay lines for wide-band pulse compression. IEEE Transactions on Sonics and Ultrasonics. 1969;**16**(3):107-117

[20] Christensen RM. Theory of Viscoelasticity. 2nd ed. Academic Press; 1982

[21] Kiełczyński P, Szalewski M, Balcerzak A. Effect of a viscous loading on Love wave propagation. International Journal of Solids and Structures. 2012;**49**:2314-2319

[22] Auld BA. Acoustics Fields and Waves in Solids, Vol. I. Florida: Krieger Publishing Company; 1990. p. 227

[23] Fowler CMR. The Solid Earth: An Introduction to Global Geophysics. 2nd ed. The Edinburgh Building, Cambridge, UK: Cambridge University Press; 2005

[24] http://www.tulane.edu/~sanelson/eens1110/earthint.htm

[25] Bormann P, Engdahl ER, Kind R. Chapter 2: Seismic wave propagation and earth models. IASPEI New Manual of Seismological Observatory Practice. ftp://ftp.ingv.it/pub/elisabetta.danastasio/grot/manual_seismological_observatory-2002.pdf

[26] Romanowicz B. Inversion of Surface Waves, A Review, International Handbook of Earthquake & Engineering Seismology, Part A, Vol. 81A. 1st ed. Part II. 2002. p. 149

[27] Haney M, Douma H. Inversion of Love wave phase velocity, group velocity and shear stress ratio using finite elements. SEG San Antonio 2011 Annual Meeting

[28] Foster A, Ekstrom G, Nettles M. Surface wave phase velocities of western unites states from a two-station method. Geophysical Journal International. 2014;**196**(2):1189-1206

[29] Fishwick S, Rowlinson N. 3-D structure of the Australian lithosphere from evolving seismic datasets. Australian Journal of Earth Sciences. 2012;**59**:809-826

[30] The seismic reflection inverse problem. Inverse Problems, Vol. 25(12). IOP Publishing Ltd; 2009. WW Symes Published

[31] Haney MM, Tsai VC. Nonperturbational surface-wave inversion: A Dix-type relation for surface waves. Geophysics. November-December 2015;**80**(6):EN167-EN177

[32] Lai CK, Wilmanski K, editors. Surface Waves in Geomechanics: Direct and Inverse Modelling for Soils and Rocks. New York: Springer; 2005

[33] Qiujiao D, Yi Z, Huang G, Yang H. Elastic metamaterial-based seismic shield for both lamb and surface waves. AIP Advances. 2017;**7**:075015

[34] Palermo A et al. Engineered metabarrier as shield from seismic surface waves. Scientific Reports. 2016;**6**:39356. DOI: 10.1038/srep39356

[35] Thévenot DR, Toth K, Durst RA, Wilsond GS. Electrochemical biosensor: Recommended definitions and classification. Biosensors and Bioelectronics. 2001;**16**:121-131

[36] Tada K, Nozawa T, Kondoh J. Real-time monitoring of methanol concentration using a shear horizontal surface acoustic wave sensor for direct methanol fuel cell without reference liquid measurement. Japanese Journal of Applied Physics. 2017;**56**:07JD15

[37] Kiełczyński P. Attenuation of Love waves in low-loss media. Journal of Applied Physics. 1997;**82**:5932-5937

[38] Caliendo C, Sait S, Boubenider F. Love-mode MEMS devices for sensing applications in liquids. Micromachines. 2016;**7**:15

[39] Wang W, He S. Sensitivity evaluation of a Love wave sensor with multi-guiding-layer structure for biochemical application. Sensors & Transducers Journal. September 2008; **96**(9):32-41

[40] Li S, Wan Y, Fan C, Su Y. Theoretical study of monolayer and double-layer waveguide Love wave sensors for achieving high sensitivity. Sensors. 2017;**17**:653

[41] Royer D, Dieulesaint E. Elastic Waves in Solids I. Berlin: Springer; 2000. p. 207

[42] Wang W, He S. A Love wave reflective delay line with polymer guiding layer for wireless sensor application. Sensors. 2008;**8**:7917-7929

[43] Haekwan O, Chen F, Kim K, Lee K. Wireless and simultaneous detections of multiple biomolecules in a single sensor using Love wave biosensor. Sensors. 2014;**14**:21660-21675

[44] Gaso MIR, Jiménez Y, Francis LA, Arnau A. Love wave biosensors: A review, state of the art in biosensors—General aspects, Chapter 11. In: Rinken T, editor. InTech, Chapters published March 13, 2013 under CC BY 3.0 license. DOI: 10.5772/45832 Edited Volume, Open Access; ISBN 978-953-51-1004-0, 360 pages

[45] Yatsuda H, Kano K, Kogai T, Yoshimura N, Goto M. Rapid diagnostic test using SH-SAW immunosensor. In: Six International Symposium on Acoustic Wave Devices for Future Mobile Communication Systems; November 24-25 2015; Chiba University, Japan

[46] Goto M, Yatsuda H, Kondoh J. Effect of viscoelastic film for shear horizontal surface acoustic wave on quartz. Japanese Journal of Applied Physics. 2015;**54**:07HD02

[47] Harding GL, Du J, Dencher PR, Barnett D, Howe E. Love wave acoustic immunosensor operation in liquid. Sensors and Actuators, A: Physical. 1997;**61**(1-3):279-286

[48] Howe E, Harding G. A comparison of protocols for the optimisation of detection of bacteria using a surface acoustic wave (SAW) biosensor. Biosensors & Bioelectronics. 2000;**15**(11-12):641-649

[49] Tamarin O, Comeau S, Déjous C, Moynet D, Rebière D, Bezian J, Pistré J. Real time device for biosensing: Design of a bacteriophage model using Love acoustic wave. Biosensors & Bioelectronics. 2003;**18**:755-763

[50] Branch DW, Brozik SM. Low-level detection of a bacillus anthracis simulant using Love-wave biosensors on 36° YX $LiTaO_3$. Biosensors & Bioelectronics. 2004;**19**:849-848

[51] Andrä J, Böhling A, Gronewold TMA, Schlecht U, Perpeet M, Gutsmann T. Surface acoustic wave biosensor as a tool to study the interactions of antimicrobial peptides with phospholipid and lipopolysaccharide model membranes. Langmuir. 2008;**24**(16):9148-9153

[52] Bisoffi M, Hjelle B, Brown DC, Branch DW, Edwards TL, Brozik SM, Bondu-Hawkins VS, Larson RS. Detection of viral bioagents using a shear horizontal surface acoustic wave biosensor. Biosensors and Bioelectronics. 2008;**23**(9):1397-1403

[53] El Fissi L, Friedt J-M, Luzet V, Chérioux F, Martin G, Ballandras S. A Love-wave sensor for direct detection of biofunctionalized nanoparticles. In: Proceedings from the IEEE frequency Control Symposium. 2009:861-865

[54] Fournel F, Baco E, Mamani-Matsuda M, Degueil M, Bennetau B, Moynet D, Mossalayi D, Vellutini L, Pillot J-P, Dejous C, Rebiere D. Love wave biosensor for real-time detection of okadaic acid as DSP phycotoxin. In: Proceedings of the Eurosensors XXIV. Austria: Linz. p. 2010

[55] Saha K, Bender F, Rasmusson A, Gizeli E. Probing the viscoelasticity and mass of a surface-bound protein layer with an acoustic waveguide device. Langmuir. 2003;**19**:1304-1311

[56] Kardous F, El Fissi L, Friedt J-M, Bastien F, Boireau W, Yahiaoui R, Manceau JF, Ballandras S. Integrated active mixing and biosensing using low frequency vibration mixer and Love-wave sensor for real time detection of antibody binding event. Journal of Applied Physics. 2011;**109**:1-8

[57] Gammoudi I, Tarbague H, Lachaud JL, Destor S, Othmane A, Moyenet D, Kalfat R, Rebiere D, Dejous C. Love wave bacterial biosensors and microfluidic network for detection of heavy metal toxicity. Sensor Letters. 2011;**9**(2):816-819

[58] Tsortos A, Papadakis G, Mitsakakis K, Melzak KA, Gizeli E. Quantitative determination of size and shape of surface-bound DNA using an acoustic wave sensor. Biophysical Journal. 2008;**94**:2706-2715

[59] Lee HJ, Namkoong K, Cho EC, Ko C, Park JC, Lee SS. Surface acoustic wave immunosensor for real-time detection of hepatitis B surface antibodies in whole blood samples. Biosensors and Bioelectronics. June 2009;**24**(10):3120-3125

[60] Gizeli E, Stevenson AC, Goddard NJ, Lowe CR. A novel Love-plate acoustic sensor utilizing polymer overlayers. IEEE Transactions on Ultrasonics, Ferroelectrics, and Frequency Control. 1992;**39**(5):657-659

[61] March C, Manclús JJ, Jiménez Y, Arnau A, Montoya A. A piezoelectric immunosensor for the determination of pesticide residues and metabolites in fruit juices. Talanta. 2009;**78**(3):827-833

[62] Stubbs DD, Lee S-H, Hunt WD. Investigation of cocaine plumes using surface acoustic wave immunoassay sensors. Analytical Chemistry. 2003;**75**(22):6231-6235

[63] Rocha-Gaso M-I, García J-V, García P, March-Iborra C, Jiménez Y, Francis L-A, Montoya Á, Arnau A. Love wave Immunosensor for the detection of carbaryl pesticide. Sensors. 2014 September;**14**(9):16434-16453

[64] In: Rinken T, editor. State of the Art in Biosensors—General Aspects. 2013. Open Access. DOI: 10.5772/45832

[65] Moore RS, McSkimin HJ. Dynamic shear properties of solvents and polystyrene solutions from 20 to 300 MHz. In: Mason WP, Thurston RN, editors. Physical Acoustics VI. New York: Academic Press; 1970. p. 167

[66] Auld BA. Acoustics Fields and Waves in Solids, Vol. II. Florida: Krieger Publishing Company; 1990. p. 275

[67] Kovacs G, Venema A. Theoretical comparison of sensitivities of acoustic shear wave modes for (bio)chemical sensing in liquids. Applied Physics Letters. 1992;**61**:639-641

[68] Gizeli E, Stevenson AC, Goddard NJ, Lowe CR. Acoustic Love plate sensors: Comparison with other acoustic devices utilizing surface SH waves. Sensors and Actuators B. 1993;**13-14**:638639

[69] Gizeli E, Goddard NJ, Lowe CR, Stevenson AC. A Love plate biosensor utilising a polymer layer. Sensors and Actuators B. 1992;**6**:131-137

[70] Moriizumi T, Unno Y, Shiokawa S. New sensor in liquid using leaky SAW. Proceedings of the Ultrasonics Symposium of IEEE. 1987:579-582

[71] Martin SJ, Ricco AJ, Frye GC. Sensing in Liquids with SH Plate Mode Devices. 1988 Ultrasonics Symposium Proceedings; 1988. pp. 607-611

[72] Haskell NA. The dispersion of surface waves in multilayered media. Bulletin of the Seismological Society of America. 1953;**43**:17-34

[73] Sezawa K. On the decay of waves in visco-elastic solid bodies. Bulletin of the Earthquake Research Institute (Japan). 1927;**3**:43-53

[74] Kiełczyński P, Szalewski M, Balcerzak A, Wieja K. Evaluation of viscoelastic parameters of surface layers by ultrasonic Love waves. 2016 IEEE International Ultrasonics Symposium Proceedings

[75] Xi DM. Resonant second-harmonic generation accompanying nonlinear Love-wave propagation in an anisotropic waveguide. Ultrasonics Symposium of IEEE. 1997. pp. 578-580

[76] Dorman J, Ewing M. Numerical inversion of seismic surface wave dispersion data and crust-mantle structure in the New York-Pennsylvania area. Geophysics. **67**:5227-5241

[77] Kiełczyński P, Szalewski M, Balcerzak A. Inverse procedure for simultaneous evaluation of viscosity and density of Newtonian liquids from dispersion curves of Love waves. Journal of Applied Physics. 2014;**116**:044902

[78] Kalyanasundarm N. International Journal of Engineering Sciences. 1981;**19**:287

[79] Frosch RA, Green PE Jr. The concept of a large aperture seismic array. Proceedings of the Royal Society A. 1966;**290**:368-384

[80] Nakanishi I, Anderson DL. Measurements of mantle wave velocities and inversion for lateral heterogeneity and anisotropy analysis by the single-station method. Geophysical Journal Royal Astronomical Society. 1984;**78**:573-617

[81] Haskell NA. Crustal reflection of plane *SH* waves. Journal of Geophysical Research. December 1960;**65**(12):4147-4150

[82] Bataille K, Lund F. Nonlinear waves in elastic media. Physica. 1982/83;**6D**(1):95-104

[83] Qu C. Piezoelectric vibration energy harvester actuated by seismic excitation [dissertation]. Politecnico di Milano; 2016

[84] Penza M, Aversa P, Cassano G, Wlodarski W, Kalantarzadeh K, Layered SAW. Gas sensor with single-walled carbon nanotube-based nanocomposite coating. Sensors and Actuators B. 2007;**127**:168-178

[85] Kiełczyński P, Szalewski M. An inverse method for determining the elastic properties of thin layers using Love surface waves. Inverse Problems in Science and Engineering. 2011;**19**:31-43

[86] Guo FL, Wang GQ, Rogerson GA. Inverse determination of liquid viscosity by means of the Bleustein–Gulyaev wave. International Journal of Solids and Structures. 2012;**49**:2115-2120

[87] Ueda K, Kondoh J. Estimation of liquid properties by inverse problems analysis based on shear horizontal surface acoustic wave sensor responses. Japanese Journal of Applied Physics. 2017;**56**:07 JD08

[88] Chen X, Jiu Hui W, Kuan L, Cao P. Slow light and stored light of Love wave within a thin film. Optik. 2017;**132**:329-336

[89] Zhang S, Bin G, Zhang H, Feng X-Q, Pan R, Alamusi NH. Propagation of Love waves with surface effects in an electrically-shorted piezoelectric nanofilm on a half-space elastic substrate. Ultrasonics. 2016;**66**:65-71

Chapter 3

Dyakonov Surface Waves: Anisotropy-Enabling Confinement on the Edge

Carlos J. Zapata-Rodríguez, Slobodan Vuković,
Juan J. Miret, Mahin Naserpour and Milivoj R. Belić

Additional information is available at the end of the chapter

http://dx.doi.org/10.5772/intechopen.74126

Abstract

The title "Dyakonov surface waves: anisotropy enabling confinement on the edge" plainly sets the scope for this chapter. The focus here is on the formation of bounded waves at the interface of two distinct media, at least one of them exhibiting optical anisotropy, which are coined as Dyakonov surface waves (DSWs) in recognition to the physicist who reported their existence for the first time. First, the general aspects of the topic are discussed. It also treats the characterization of bounded waves in isotropic-uniaxial multilayered structures, allowing not only the derivation of the dispersion equation of DSWs but also that of surface plasmons polaritons (SPPs), for instance. Furthermore, the interaction of such surfaces waves, with the possibility of including guided waves in a given planar layer and external sources mimicking experimental setups, can be accounted for by using the transfer matrix formalism introduced here. Finally, special attention is devoted to hyperbolic media with indefinite anisotropy-enabling hybridized scenarios integrating the prototypical DSWs and SPPs.

Keywords: surface waves, anisotropy, transfer matrix formulation

1. Introduction

The planar interface of two dissimilar materials plays a relevant role in many optical phenomena. In recent years, particularly, evanescent waves have been used in newly developing technologies such as near-field spectroscopy. The electromagnetic surface wave, which is intimately tied to the interface, travels in a direction parallel to the interface but, on either side of the interface, its amplitude is imperceptible after a certain distance from the interface. The notion of an electromagnetic surface wave made a significant appearance in 1907 when

Zen-neck [1] authored a theoretical paper exploring the possibility of a wave guided by the interface of the atmosphere and either Earth or a large body of water. His focus was on radio waves, a region of the electromagnetic spectrum far from the optical regime in which we are particularly interested, but the principles involved are the same, owing to the scale invariance of the Maxwell postulates.

Yet, nearly a century later, a unique type of wave, the surface plasmon polariton (SPP) wave, that dominates the nanotechnology scene, at least at optical frequencies, resulted in wonderful developments with the creation of extremely sensitive bio/chemical sensors, and improvements in this mature technology continue to this day [2]. Even in this highly developed application, the two partnering materials which meet at the interface may be simple: one is a typical metal, a plasmonic material at optical frequencies, and the other is a homogeneous, isotropic, dielectric material. While the interface of a plasmonic material and a polarizable material supports SPPs, a variety of other types of surface waves can be supported by the interface of two polarizable materials. Since polarizable materials such as dielectric materials are less dissipative, in general, than plasmonic materials such as metals, the advantage of these materials for long-range propagation of surface waves is apparent.

The interface of two homogeneous dielectric materials of which at least one is anisotropic may support surface-wave propagation of another type, even though the real parts of all components of the permittivity dyadics of both materials are positive. Interest in surface waves guided by the interface of two dielectric materials began to take after Dyakonov in 1988 [3] explored the propagation of a surface wave guided by the interface of a uniaxial dielectric material and an isotropic dielectric material. The Dyakonov surface wave (DSWs) is the focus of this chapter.

In this chapter, we perform a thorough analysis of DSWs taking place in semi-infinite anisotropic media. Basic concepts related to the propagation of electromagnetic waves in homogeneous media will be introduced, including isotropic and anisotropic materials. Birefringent metal-dielectric (MD) lattices will be also considered as a contribution of meta-materials in the development of DSWs [4]. Special emphasis will be put when the effective-medium approaches induce unsatisfactory results, which occur in most experimental configurations. Practical cases will be analyzed including dissipative effects due to Ohmic losses of the metal.

2. Wave propagation in bulk media and interfaces

In this section we introduce the basic concepts related to the propagation of electromagnetic waves in homogeneous media, including isotropic and anisotropic materials. We describe in detail complex multilayered structures. For that purpose, we introduce a transfer matrix formulation that applies to isotropic and uniaxial media simultaneously. Finally, we discuss the conditions that give rise to surface waves at the interface of two isotropic media; the case of dealing with anisotropic media is considered in Section 5. Moreover, we obtain the dispersion equation for SPPs, which appears at the interface between a dielectric and a metal.

2.1. Wave propagation in isotropic media

In this section, we consider the propagation of electromagnetic waves in linear, homogeneous, and isotropic dielectrics. Under these conditions, the relative permittivity ϵ relating **E** and **D** is a scalar constant. Considering that the medium is free of electric charges and currents, and taking into account the medium equation $\mathbf{B} = \mu_0\mathbf{H}$, Maxwell's equations can be written as

$$\nabla\times\mathbf{H} = \epsilon\epsilon_0\frac{\partial\mathbf{E}}{\partial t}, \tag{1a}$$

$$\nabla\times\mathbf{E} = -\mu_0\frac{\partial\mathbf{H}}{\partial t}, \tag{1b}$$

$$\nabla\cdot\mathbf{E} = 0, \tag{1c}$$

$$\nabla\cdot\mathbf{H} = 0. \tag{1d}$$

Now, each of the scalar components of **E** and **H** satisfies the wave equation $\nabla^2 u - c^{-2}\partial_t^2 u = 0$, where u represents any one of the six scalar components of the electromagnetic field and c is the speed of the waves in the medium.

When the electromagnetic wave is plane and monochromatic, all components of the electric and magnetic fields are harmonic functions in time and space at the time frequency ω and spatial frequency $\mathbf{k} = (k_x, k_y, k_z)$, respectively. Particularly they may be set as

$$\mathbf{E}(\mathbf{r},\mathrm{t}) = \mathbf{E}_0\ \exp(i\mathbf{k}\cdot\mathbf{r})\exp(-i\omega t), \tag{2a}$$

$$\mathbf{H}(\mathbf{r},\mathrm{t}) = \mathbf{H}_0\ \exp(i\mathbf{k}\cdot\mathbf{r})\exp(-i\omega t), \tag{2b}$$

where $\mathbf{E}_0(\mathbf{r})$ and $\mathbf{H}_0(\mathbf{r})$ are the complex amplitudes of the electric and magnetic fields. If we substitute the vector wave fields of Eqs. (2) in Maxwell's equations (1), with the help of the transformations $\nabla \to i\mathbf{k}$ and $\partial_t \to -i\omega$, we might attain a simplified expression of $\mathbf{k}\times(\mathbf{k}\times\mathbf{E}_0)$, enabling to obtain the following wave equation: $\mathbf{M}\cdot\mathbf{E}_0 = 0$, where $\mathbf{M} \equiv \mathbf{k}\otimes\mathbf{k} - k^2\mathbf{I} + k_0^2\epsilon\mathbf{I}$. Here **I** is the 3×3 identity matrix, and k is the modulus of the wavevector **k** and $k_0 = \omega/c_0$. In order to obtain the dispersion equation, we look for nontrivial solutions of the electric field $\mathbf{E}_0$ by imposing that $\det(M) = 0$. Its solution leads to $k^2 = \omega^2/c^2$. The electric field amplitude $\mathbf{E}_0$ can be written as a linear combination of the following vectors

$$\widehat{e}_1 = (0, k_z, -k_y), \tag{3a}$$

$$\widehat{e}_2 = \left(k_y^2 + k_z^2, -k_y k_x, -k_z k_x\right). \tag{3b}$$

We point out that $\widehat{e}_1$ is associated with TE^{x} modes and that $\widehat{e}_1.\widehat{e}_2 = 0$. Although not demonstrated here, $\widehat{e}_2$ is related to TM^{x}-polarized plane waves. Note also that Eqs. (1c) and (1d) lead to the following orthogonality relations-hips: $\mathbf{k}\cdot\hat{e}_1 = \mathbf{k}\cdot\hat{e}_2 = 0$. As a result, the vectors $\{\hat{e}_1, \hat{e}_2, \mathbf{k}\}$ form an orthogonal trihedron.

2.2. Wave propagation in uniaxial media

Uniaxial crystals are media with certain symmetries that make them have two equal principal refractive indices: $n_x = n_y \equiv n_o$ (ordinary index) and $n_z \equiv n_e$ (extraordinary index). The crystal is to be a positive uniaxial if $n_e > n_o$ and negative uniaxial if $n_e < n_o$. The z axis of a uniaxial crystal is called the optic axis. We call it the ordinary polarization direction if the wave has an eigenindex of refraction n_o and extraordinary, if the wave has an eigenindex of refraction n_e. In **Table 1** we show the values of n_o and n_e for some natural birefringent materials (uniaxial crystals).

Let us now consider the propagation of wave planes in uniaxial media. To obtain the eigenvalues associated with plane-wave propagation, we proceed in a similar way as in Section 2.1 for isotropic media, but taking into account that now the relative permittivity $\boldsymbol{\epsilon} = \epsilon_x(\mathbf{x}\otimes\mathbf{x} + \mathbf{y}\otimes\mathbf{y}) + \epsilon_z(\mathbf{z}\otimes\mathbf{z})$ is a tensor. Therefore, we solve $\det(\mathbf{M}) = 0$, where the matrix $\mathbf{M} \equiv \mathbf{k}\otimes\mathbf{k} - k^2\mathbf{I} + k_0^2\boldsymbol{\epsilon}$. Then, after solving the abovementioned determinant, we obtain two solutions. The first of them is $k_x^2 + k_y^2 + k_z^2 = \epsilon_x k_0^2$ which corresponds to the dispersion equation of the ordinary plane waves. The electric field for this kind of plane waves is proportional to the vector $\widehat{e}_o = \left(-k_y, k_x, 0\right)$. As a consequence, ordinary plane waves are TE^z-polarized waves. The second solution gives us the dispersion equation of the extraordinary plane waves:

$$\frac{k_x^2 + k_y^2}{\epsilon_z} + \frac{k_z^2}{\epsilon_x} = k_0^2. \tag{4}$$

In this case, the electric field is proportional to the vector $\hat{e}_e = \left(k_x k_z, k_y k_z, k_z^2 - \epsilon_x k_0^2\right)$.

2.3. Matrix formulation for multilayered media

In this section we look at the case of multilayered media composed of different nonmagnetic materials which are separated by planar parallel interfaces, displaced on $x = x_i$ as shown in **Figure 1**. In particular, we deal with either uniaxial or isotropic materials, including metals. We make a detailed description of the electromagnetic fields inside a given medium "i", which lies in $x_{i-1} < x < x_i$. Our objective is the analysis of the appropriate conditions for the propagation of surface waves at the abovementioned interfaces.

Birefringent material	n_o	n_e	$\Delta n = n_e - n_o$
Crystal quartz	1.547	1.556	0.009
MgF	1.3786	1.3904	0.0118
YVO_4	1.9929	2.2154	0.2225
Rutile (TiO_2)	2.65	2.95	0.3
E7 liquid crystal	1.520	1.725	0.205
Calomel (Hg_2Cl_2)	1.96	2.62	0.68

Table 1. Birefringence Δn of some natural materials [5].

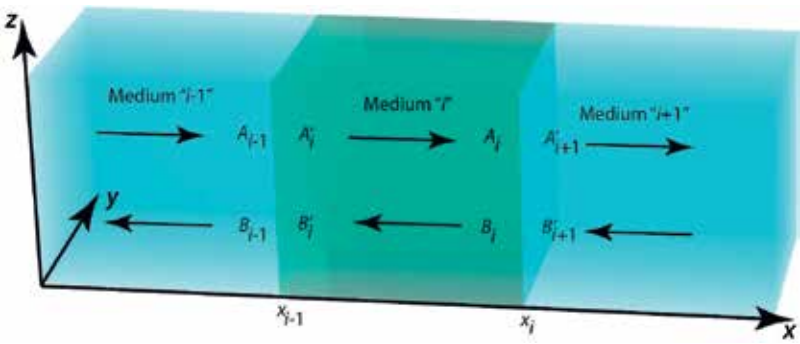

Figure 1. Schematic arrangement of the multilayered media. The amplitudes A_i and A'_i (B_i and B'_i) correspond to waves propagating along the positive (negative) x-axis. These amplitudes characterize a given state of polarization: For uniaxial media we may deal with ordinary (for example, A_{oi}) and extraordinary (A_{ei}) waves. For isotropic materials we have TE-polarized (A_{TEi}) and TM-polarized (A_{TMi}) waves.

2.3.1. Electromagnetic fields in a uniaxial elementary layer

Let us first consider a multilayered media of uniaxial materials. For simplicity, let us take into account only relative permittivities of the form $\boldsymbol{\epsilon}_i = \epsilon_{xi}(\mathbf{x}\otimes\mathbf{x} + \mathbf{y}\otimes\mathbf{y}) + \epsilon_{zi}(\mathbf{z}\otimes\mathbf{z})$ for a given medium "i." As we demonstrated in Section 2.2, the dispersion equation for extraordinary waves propagating in bulk uniaxial media is given by Eq. (4). Due to the boundary conditions at the interfaces between different media, the components of the wave vector k_y and k_z are conserved, but not its projection upon the x-axis. More specifically, if we rename $k_{xi} \equiv k_{oi}$ for ordinary waves, we can write

$$k_{oi} = \sqrt{\epsilon_{xi}k_0^2 - \left(k_y^2 + k_z^2\right)}, \tag{5}$$

and for extraordinary waves (here $k_{xi} \equiv k_{ei}$)

$$k_{ei} = \sqrt{\epsilon_{zi}k_0^2 - \left(k_y^2 + \frac{\epsilon_{zi}k_z^2}{\epsilon_{xi}}\right)}, \tag{6}$$

taken from Eq. (4).

The total electric field of the elementary layer "i" is set as

$$\mathbf{E}_{tot}^{(i)} = \mathbf{E}^{(i)}(x)\exp\left(ik_y y + ik_z z - i\omega t\right). \tag{7}$$

The part of the electric field that varies along with the spatial coordinate x can be written as

$$\begin{aligned}\mathbf{E}^{(i)}(x) = \; & A_{oi}\hat{a}_{oi}\exp\left[ik_{oi}(x-x_i)\right] + B_{oi}\hat{b}_{oi}\exp\left[-ik_{oi}(x-x_i)\right] \\ & + A_{ei}\hat{a}_{ei}\exp\left[ik_{ei}(x-x_i)\right] + B_{ei}\hat{b}_{ei}\exp\left[-ik_{ei}(x-x_i)\right],\end{aligned} \tag{8}$$

where the amplitude A_{oi} (and A_{ei}) corresponds to propagating ordinary (and extraordinary) waves, and B_{oi} (and B_{ei}) is related with counter-propagating ordinary (and extraordinary)

waves. Note that all these amplitudes have zero dephase at $x = x_i$. Finally, the vectors $\hat{a}_{oi}$ and $\hat{a}_{ei}$ are rewritten as:

$$\hat{a}_{oi} = \left(-k_y, k_{oi}, 0\right), \tag{9a}$$

$$\hat{a}_{ei} = \left(k_{ei}k_z, k_y k_z, k_z^2 - \epsilon_{xi}k_0^2\right). \tag{9b}$$

In the case of counter-propagating waves, we take into consideration that $k_{xi} = -k_{oi}$ for ordinary waves and $k_{xi} = -k_{ei}$ for extraordinary waves. This fact leads us to introduce the vector fields

$$\hat{b}_{oi} = \left(-k_y, -k_{oi}, 0\right), \tag{10a}$$

$$\hat{b}_{ei} = \left(-k_{ei}k_z, k_y k_z, k_z^2 - \epsilon_{xi}k_0^2\right). \tag{10b}$$

The vector fields $\hat{a}_{oi}$ and $\hat{b}_{oi}$ can be given in units of k_0, whereas $\hat{a}_{ei}$ and $\hat{b}_{ei}$ can be expressed in units of k_0^2.

For convenience, the field function $\mathbf{E}^{(i)}$ can be set in terms of the wave amplitudes A'_{oi}, A'_{ei} and B'_{oi} and B'_{ei} with zero dephase at $x = x_{i-1}$, namely:

$$\begin{aligned}\mathbf{E}^{(i)}(x) = {} & A'_{oi}\hat{a}_{oi}\exp\left[ik_{oi}(x - x_{i-1})\right] + B'_{oi}\hat{b}_{oi+1}\exp\left[-ik_{oi}(x - x_{i-1})\right] \\ & + A'_{ei}\hat{a}_{ei}\exp\left[ik_{ei}(x - x_{i-1})\right] + B'_{ei}\hat{b}_{ei}\exp\left[-ik_{ei}(x - x_{i-1})\right].\end{aligned} \tag{11}$$

The complete set of amplitudes is A_{qi}, A'_{qi} and B_{qi} and B'_{qi} where $q = \{o, e\}$ satisfies the following relationships:

$$A'_{qi} = A_{qi}\exp\left[-ik_{qi}(x_i - x_{i-1})\right], \tag{12a}$$

$$B'_{qi} = B_{qi}\exp\left[ik_{qi}(x_i - x_{i-1})\right]. \tag{12b}$$

For completeness we calculate the magnetic field in a given elementary layer "i." By using the Maxwell's equation $\mathbf{H}_{tot}^{(i)} = \left(i\omega\mu_0\right)^{-1}\nabla\times\mathbf{E}_{tot}^{(i)}$, and considering that the magnetic field may be written as $\mathbf{H}_{tot}^{(i)} = \mathbf{H}^{(i)}(x)\exp\left(ik_y y + ik_z z - i\omega t\right)$, we finally obtain the following expression for the variation of the field along the x direction, namely:

$$\begin{aligned}\omega\mu_0\mathbf{H}^{(i)}(x) = {} & A_{oi}\hat{c}_{oi}\exp\left[ik_{oi}(x - x_i)\right] + B_{oi}\hat{d}_{oi}\exp\left[-ik_{oi}(x - x_i)\right] \\ & + A_{ei}\hat{c}_{ei}\exp\left[ik_{ei}(x - x_i)\right] + B_{ei}\hat{d}_{ei}\exp\left[-ik_{ei}(x - x_i)\right].\end{aligned} \tag{13}$$

In the previous equations, the new vector fields are set as

$$\hat{c}_{oi} = -\left(k_{oi}k_z, k_y k_z, k_z^2 - \epsilon_{xi}k_0^2\right), \tag{14a}$$

$$\hat{c}_{ei} = \epsilon_{xi}k_0^2\left(-k_y, k_{ei}, 0\right), \tag{14b}$$

$$\hat{d}_{oi} = -\left(-k_{oi}k_z, k_y k_z, k_z^2 - \epsilon_{xi}k_0^2\right), \tag{14c}$$

$$\hat{d}_{ei} = -\epsilon_{xi}k_0^2\left(k_y, k_{ei}, 0\right). \tag{14d}$$

We point out that the vector fields $\hat{c}_{oi}$ and $\hat{d}_{oi}$ can be given in units of k_0^2, whereas $\hat{c}_{ei}$ and $\hat{d}_{ei}$ can be expressed in units of k_0^3.

2.3.2. Boundary conditions for anisotropic layered media

Once we have a complete description of the wave fields in every elementary layer of our metamaterial, we have to impose some boundary conditions at the interfaces $x = x_i$. The components of the electric field $\mathbf{E}_{tot}^{(i)}$ and the magnetic field $\mathbf{H}_{tot}^{(i)}$ lying on the planes $x = x_i$ must be continuous. Particularly these boundary conditions may be expressed in a matrix form as

$$\mathbf{D}_i \mathbf{v}_i = \mathbf{D}_{i+1} \mathbf{v'}_{i+1}. \tag{15}$$

We defined the following matrix, explicitly given as

$$\mathbf{D}_i = \begin{bmatrix} k_{oi} & -k_{oi} & k_y k_z & k_y k_z \\ 0 & 0 & k_z^2 - \epsilon_{xi}k_0^2 & k_z^2 - \epsilon_{xi}k_0^2 \\ -k_y k_z & -k_y k_z & \epsilon_{xi}k_0^2 k_{ei} & -\epsilon_{xi}k_0^2 k_{ei} \\ -k_z^2 + \epsilon_{xi}k_0^2 & -k_z^2 + \epsilon_{xi}k_0^2 & 0 & 0 \end{bmatrix}. \tag{16}$$

On the other hand, we introduced the amplitude column vectors

$$\mathbf{v}_i = \begin{bmatrix} A_{oi} \\ B_{oi} \\ A_{ei} \\ B_{ei} \end{bmatrix}, \mathbf{v'}_i = \begin{bmatrix} A'_{oi} \\ B'_{oi} \\ A'_{ei} \\ B'_{ei} \end{bmatrix}. \tag{17}$$

The matrix formulation can also be used to relate the amplitude vector $\mathbf{v}_i$ with zero-phase shift at $x = x_i$ with the amplitude vector $\mathbf{v'}_i$ exhibiting zero dephase at $x = x_{i-1}$, previously established in Eq. (12a), (12b). For that purpose, we introduce the propagation matrix $\mathbf{P}_i$, which takes into account the amplitude dephasing between the boundaries of each layer. Explicitly we may write

$$\mathbf{v'}_i = \mathbf{P}_i \cdot \mathbf{v}_i, \tag{18}$$

being

$$\mathbf{P}_i = \begin{bmatrix} e^{-ik_{oi}w_i} & 0 & 0 & 0 \\ 0 & e^{ik_{oi}w_i} & 0 & 0 \\ 0 & 0 & e^{-ik_{ei}w_i} & 0 \\ 0 & 0 & 0 & e^{ik_{ei}w_i} \end{bmatrix}, \tag{19}$$

where $w_i = x_i - x_{i-1}$ denotes the width of the elementary layer "i." We note that equivalent matrix formulations for anisotropic multilayered media can be found elsewhere [6, 7].

2.3.3. Electromagnetic fields in layered isotropic media

At this point, once we have described the electromagnetic fields in uniaxial media, let us study a multilayered media composed of isotropic materials. Considering an isotropic medium of relative permittivity ϵ_i, once again, the projection of the wave vector along the positive x direction is set as

$$k_{TEi} = k_{TMi} = \sqrt{\epsilon_i k_0^2 - \left(k_y^2 + k_z^2\right)}. \tag{20}$$

Formally, k_{TMi} applies to TM-polarized waves and k_{TEi} corresponds to TE-polarized waves. The total electric field of the elementary layer "i" can be set, again, as given in Eq. (7). The part of the electric field that varies along with the spatial coordinate x can be written using the amplitude A_{TEi} (and A_{TMi}), which corresponds to propagating TE (and TM) waves and B_{TEi} (and B_{TMi}) that is related with counter-propagating TE (and TM) waves. This finally reads as

$$\begin{aligned}\mathbf{E}^{(i)}(x) = {} & A_{TEi}\,\hat{a}_{TEi}\exp\left[ik_{TEi}(x - x_i)\right] + B_{TEi}\,\hat{b}_{TEi}\exp\left[-ik_{TEi}(x - x_i)\right] \\ & + A_{TMi}\,\hat{a}_{TMi}\exp\left[ik_{TMi}(x - x_i)\right] + B_{TMi}\,\hat{b}_{TMi}\exp\left[-ik_{TMi}(x - x_i)\right].\end{aligned} \tag{21}$$

Note that all these amplitudes have zero dephase at $x = x_i$. Finally, the vectors $\hat{a}_{TEi}$ and $\hat{a}_{TMi}$ are given in Eq. (3a), (3b) by $\hat{e}_1$ and $\hat{e}_2$, respectively, which we rewrite as

$$\hat{a}_{TEi} = \hat{b}_{TEi} = \left(0, k_z, -k_y\right), \tag{22a}$$

$$\hat{a}_{TMi} = \left(k_y^2 + k_z^2, -k_y k_{TMi}, -k_z k_{TMi}\right), \tag{22b}$$

$$\hat{b}_{TMi} = \left(k_y^2 + k_z^2, k_y k_{TMi}, k_z k_{TMi}\right). \tag{22c}$$

In Eq. (22a) and (22c) we have included the field vectors $\hat{b}_{TEi}$ and $\hat{b}_{TMi}$ which are associated with counter-propagating waves. Again, we point out that the vector fields $\hat{a}_{TEi}$ and $\hat{b}_{TEi}$ can be given in units of k_0, and the vectors $\hat{a}_{TMi}$ and $\hat{b}_{TMi}$ can be expressed in units of k_0^2. Similarly as performed in the previous section, the field function $\mathbf{E}^{(i)}$ can also be set in terms of the wave amplitudes A'_{TEi}, A'_{TEi}, B'_{TMi}, and B'_{TMi} with zero dephase at $x = x_{i-1}$. As in the previous section, the amplitudes A_{qi}, A'_{qi}, B_{qi}, and B'_{qi}, where $q = \{\mathrm{TE}, \mathrm{TM}\}$, are related by $A'_{qi} = A_{qi}\exp\left(-ik_{qi}w_i\right)$ and $B'_{qi} = B_{qi}\exp\left(ik_{qi}w_i\right)$. Following the same procedure seen earlier, we calculate the magnetic field in every elementary layer "i." We finally obtain the following expression for the variation of the field along the x direction, namely

$$\begin{aligned}\omega\mu_0\mathbf{H}^{(i)}(x) = {} & A_{TEi}\,\hat{c}_{TEi}\exp\left[ik_{TEi}(x - x_i)\right] + B_{TEi}\,\hat{d}_{TEi}\exp\left[-ik_{TEi}(x - x_i)\right] \\ & + A_{TMi}\,\hat{c}_{TMi}\exp\left[ik_{TMi}(x - x_i)\right] + B_{TMi}\,\hat{d}_{TMi}\exp\left[-ik_{TMi}(x - x_i)\right].\end{aligned} \tag{23}$$

In the previous equation we introduced the vector fields

$$\hat{a}_{TEi} = \hat{b}_{TEi} = \left(0, k_z, -k_y\right), \tag{24a}$$

$$\hat{a}_{TMi} = -\hat{c}_{TEi} = -\left(-k_y^2 - k_z^2, k_y k_{TEi}, k_z k_{TEi}\right), \tag{24b}$$

$$\hat{b}_{TMi} = -\hat{d}_{TEi} = \left(k_y^2 + k_z^2, k_y k_{TEi}, k_z k_{TEi}\right), \tag{24c}$$

$$\hat{c}_{TMi} = \hat{d}_{TMi} = \epsilon_i k_0^2 \left(0, k_z, -k_y\right). \tag{24d}$$

Note that $\hat{c}_{TMi} = \epsilon_i k_0^2 \hat{a}_{TEi}$. We conclude that the amplitudes A_{TEi} and B'_{TEi} are associated with TE-polarized waves along the x-axis, that is, TE^x waves, and A_{TMi} and B'_{TMi} are field amplitudes of TM^x waves.

2.3.4. Application of the boundary conditions

At a given interface $x = x_i$, the electromagnetic fields should accomplish the continuity boundary conditions. Note that we can write the four equations derived from the boundary conditions in the following matrix form:

$$\mathbf{D}_i \mathbf{v}_i = \mathbf{D}_{i+1} \mathbf{v'}_{i+1}. \tag{25}$$

In the previous matrix equation, we introduced the element

$$\mathbf{D}_i = \begin{bmatrix} k_z & k_z & -k_y k_{TMi} & k_y k_{TMi} \\ -k_y & -k_y & -k_z k_{TMi} & k_z k_{TMi} \\ k_y k_{TEi} & -k_y k_{TEi} & \epsilon_i k_0^2 k_z & \epsilon_i k_0^2 k_z \\ k_z k_{TEi} & -k_z k_{TEi} & -\epsilon_i k_0^2 k_y & -\epsilon_i k_0^2 k_y \end{bmatrix}. \tag{26}$$

Finally, the amplitude vectors now are represented as

$$\mathbf{v}_i = \begin{bmatrix} A_{TEi} \\ B_{TEi} \\ A_{TMi} \\ B_{TMi} \end{bmatrix}, \mathbf{v'}_i = \begin{bmatrix} A'_{TEi} \\ B'_{TEi} \\ A'_{TMi} \\ B'_{TMi} \end{bmatrix}. \tag{27}$$

The matrix formulation can also be used to relate the amplitude vector $\mathbf{v}_i$ with zero-phase shift at $x = x_i$ with the amplitude vector $\mathbf{v'}_i$ exhibiting zero dephase at $x = x_{i-1}$. For that purpose, we introduce the propagation matrix for the TE^x and TM^x modes

$$\mathbf{P}_i = \begin{bmatrix} e^{-ik_{TEi}w_i} & 0 & 0 & 0 \\ 0 & e^{ik_{TEi}w_i} & 0 & 0 \\ 0 & 0 & e^{-ik_{TMi}w_i} & 0 \\ 0 & 0 & 0 & e^{ik_{TMi}w_i} \end{bmatrix}, \tag{28}$$

which takes into account the amplitude phase shift due the finite width $w_i = x_i - x_{i-1}$ of each layer. Explicitly we will write $\mathbf{v'}_i = \mathbf{P}_i \cdot \mathbf{v}_i$, which is formally the same as Eq. (18), previously derived for uniaxial media.

3. Surface modes in isotropic media

The main purpose of this chapter is the analysis of Dyakonov surface waves, which originally was formulated for an isotropic medium and a uniaxial crystal. However, this analysis is developed in Section 5. Here we introduce the most well-known surface waves arisen at the interface between isotropic media of different dielectric constants. In addition, these surface waves will play a relevant role when dealing with metal-dielectric multilayered structures.

The so-called surface plasmon polaritons are waves that propagate along the surface of a conductor, usually a metal [2, 8, 9]. These are essentially light waves that are trapped on the surface, evanescently confined in the perpendicular direction and caused by their interaction with the free electrons of the conductor, the latter oscillating in resonance with the electromagnetic field. To describe these wave fields, we use the matrix formalism applied in the vicinity of a single interface between two isotropic media with different dielectric permittivities.

Let us consider the propagation of bound waves on the interface between two semi-infinite media, which are denoted as medium 1 and medium 2 with dielectric permittivities ϵ_1 i ϵ_2, respectively. This interface is located at $x_1 = 0$. For medium 1, the electric and magnetic fields varying along the x-axis are given by Eqs. (22a), (22b), (22c) and (24a), (24b), (24c), (24d) respectively.

As we are only interested in bound states; the elements of the remaining field vectors read as

$$\mathbf{v}_1 = \begin{bmatrix} 0 \\ B_{TE1} \\ 0 \\ B_{TM1} \end{bmatrix} \text{ and } \mathbf{v'}_2 = \begin{bmatrix} A'_{TE2} \\ 0 \\ A'_{TM2} \\ 0 \end{bmatrix}. \tag{29}$$

The values of the amplitudes A_{TE1}, A_{TM1}, B'_{TE2}, and B'_{TM2} are identically zero in case of lack of interaction with external sources, as we assume here. Since we are dealing with bound states, the wavenumbers k_{TE1}, k_{TM1}, $k_{TE2,}$, and k_{TM2} are purely imaginary. The application of the boundary conditions, $\mathbf{D}_1\mathbf{v}_1 = \mathbf{D}_2\mathbf{v'}_2$, gives us the following two equations:

$$0 = \frac{\epsilon_2 k_{TM1} + \epsilon_1 k_{TM2}}{2\epsilon_1 k_{TM1}} A'_{TM2}, \tag{30a}$$

$$B_{TM1} = \frac{\epsilon_2 k_{TM1} - \epsilon_1 k_{TM2}}{2\epsilon_1 k_{TM1}} A'_{TM2}. \tag{30b}$$

To accomplish Eq. (30a), the following equation must be satisfied, $k_{TM2}/k_{TM1} = -\epsilon_2/\epsilon_1$. This is the dispersion equation of the TM^x-polarized surface modes. As k_{TM1} and k_{TM2} have a vanishing real part and a positive imaginary part, this requires that $\epsilon_2/\epsilon_1 < 0$, that is, one of the relative permittivities must be negative. Once we have obtained the relationship between the relative permittivities and the purely imaginary wavenumbers, we may obtain a new ligature involving the field amplitudes, $B_{TM1} = (\epsilon_2/\epsilon_1)A'_{TM2}$, which have been derived from Eq. (30b). We may rewrite the dispersion equation, making use of the definition of k_{TMi} given in Eq. (20), resulting:

$$k_{SPP} = k_0\sqrt{\frac{\epsilon_1\epsilon_2}{\epsilon_1+\epsilon_2}}, \tag{31}$$

where $k_{SPP} = \sqrt{k_y^2 + k_z^2}$ is the SPP wavenumber. In **Figure 2** we represent Eq. (31) giving the dispersion relation for TM-bounded modes at frequencies lower than the surface plasmon frequency:

$$\omega_{SPP} = \frac{\omega_p}{\sqrt{1+\epsilon_1}}. \tag{32}$$

At $\omega \to 0$ the SPP wavenumber tends to zero; however, when $\omega \to \omega_{SPP}$ we find that $k_{SPP} \to \infty$. In addition, radiative modes may arise at higher frequencies, typically $\omega \geq \omega_p$; in such cases, the wave field is not confined near the interface and it will lose its energy by radiation.

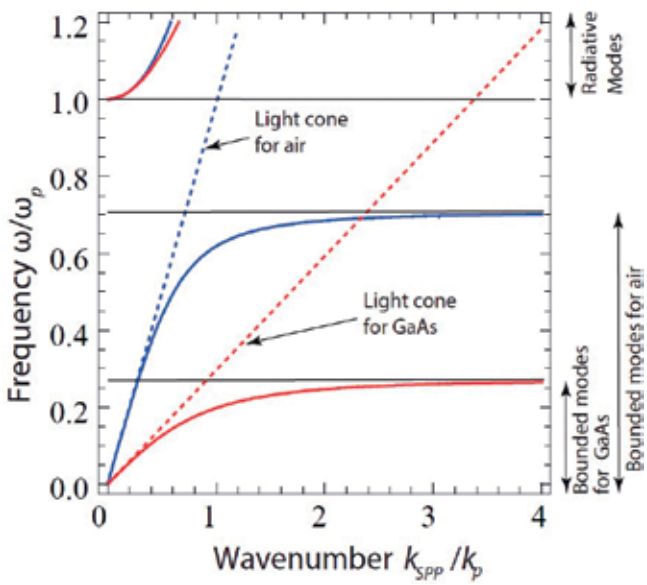

Figure 2. SPP dispersion relation at the interface between a lossless Drude metal ($\epsilon_2(\omega) = 1 - \omega_p^2/\omega^2$) and a dielectric: air in blue ($\epsilon_1 = 1$) and GaAs in red ($\epsilon_1 = 11.55$). Note that $k_p = \omega_p/c$.

4. Multilayered plasmonic lattices

Wave propagation in periodic media can be treated as the motion of electrons in crystalline solids. In fact, formulation of the Kronig-Penney model used in the elementary band theory of solids is mathematically identical to that of the electromagnetic radiation in periodic layered media. Thus, some of the physical concepts used in material physics such as Bloch waves, Brillouin zones, and forbidden bands can also be used here. A periodic layered medium is equivalent to a one-dimensional lattice that is invariant under lattice translation.

Here we will treat the propagation of electromagnetic radiation in a simple periodic layered medium that consists of alternating layers of transparent nonmagnetic materials with different electric permittivities. The layers are set in a way that the x-axis points along the perpendicular direction of the layers. The permittivity profile is given by ϵ_1, for $x_0 < x < x_1$, and ϵ_2, for $x_1 < x < x_2$. In addition, the relative permittivity satisfies the condition of periodicity, $\epsilon(x) = \epsilon(x + \Lambda)$, where $w_1 = x_1 - x_0$ ($w_2 = x_2 - x_1$) is the thickness of the layers of permittivity ϵ_1 (ϵ_2) and $\Lambda = w_1 + w_2$ represents the period of the structure.

According to the Floquet theorem, solutions of the wave equation for a periodic medium may be set in the form $\mathbf{E}^{(i+2)}(x + \Lambda) = \mathbf{E}^{(i)}(x) \cdot \exp(iK\Lambda)$. The constant K is known as the Bloch wavenumber. The problem is thus that of determining K and $\mathbf{E}^{(i)}(x)$. Finally, the equation

$$\cos(K_q \Lambda) = \frac{1}{2}\mathrm{tr}_q. \tag{33}$$

represents the dispersion relation for TE and TM modes, written in a compact way. Representing K_{TE} (K_{TM}), the Bloch wavenumber K associated with the mode TE (TM), and writing

$$\mathrm{tr}_{TE} = 2\cos(w_1 k_{\mathrm{TE}1})\cos(w_2 k_{\mathrm{TE}2}) - \frac{\left(k_{\mathrm{TE}1}^2 + k_{\mathrm{TE}2}^2\right)}{k_{\mathrm{TE}1} k_{\mathrm{TE}2}} \sin(w_1 k_{\mathrm{TE}1}) \sin(w_2 k_{\mathrm{TE}2}), \tag{34a}$$

$$\mathrm{tr}_{TM} = 2\cos(w_1 k_{\mathrm{TM}1})\cos(w_2 k_{TM2}) - \frac{\left(\epsilon_2^2 k_{TM1}^2 + \epsilon_1^2 k_{TM2}^2\right)}{\epsilon_1 \epsilon_2 k_{TM1} k_{TM2}} \sin(w_1 k_{TM1}) \sin(w_2 k_{TM2}). \tag{34b}$$

we find the dispersion equation of a binary periodic medium for each polarization.

Neglecting losses in the materials, regimes where $|tr_q| < 2$ correspond to real K_q and thus to propagating Bloch waves, when $|tr_q| > 2$; however, $K_q = m\pi/\Lambda + iK_{qi}$, where m is an integer and K_{qi} is the imaginary part of K_q, which gives an evanescent behavior to the Bloch wave. These are the so-called forbidden bands of the periodic medium. The band edges are set for $|tr_q| = 2$.

In **Figure 3**, the transverse wavenumber reads as

$$k_t = \sqrt{k_y^2 + k_z^2}. \tag{35}$$

For ultra-thin metallic layers, for instance, $w_m = 3$ nm, the curves resembles ellipses and circumferences for TM and TE modes, respectively. In the particular case of TM modes, a secondary curve surges, in relation with the excitation of SPPs. For increasing values of the

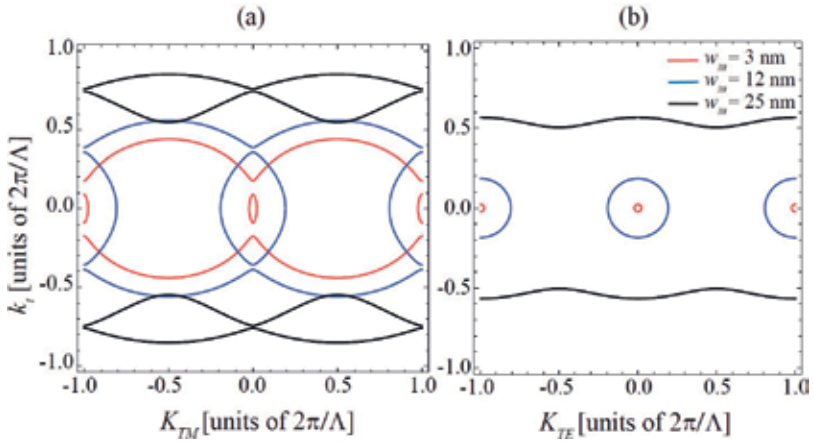

Figure 3. Exact dispersion curves derived from Eq. (33) for a lossless Drude metal/GaAs composite medium with $\lambda = 1.55\,\mu$ m, $\omega_p = 13.94\,\text{fs}^{-1}$ and $\epsilon_1 = 11.55$, for (a) TM modes and (b) TE modes. GaAs layer is always 12 times thicker than the metallic layer.

metal width, some deviations are evident. Reaching a given value of w_m, a large band gap centered at $k_t = 0$ surges. Particularly for TM modes, at $K_{TM} = 0$, the two curves collapse. This fact may be understood as that the symmetric and antisymmetric surface modes in the metallic layer approach for SPP in a single metal-dielectric interface, giving $k_t \to k_{SPP}$ [see Eq. (31)]. For illustration, the wavenumber of the SPP propagating on the interface of our Drude metal/GaAs materials yields $k_{SPP} = 0.746 \cdot 2\pi/\Lambda$, assuming that $\Lambda = 325\,\text{nm}$ (associated with the period of a multilayer with metal thickness $w_m = 25$ nm).

4.1. Effective medium approach

For near-infrared and visible wavelengths, nanolayered metal-dielectric compounds enable a simplified description of the medium by using the long-wavelength approximation, which involves a homogenization of the structured metamaterial [10, 11]. The effective medium approach (EMA), as Rytov exposed in his seminal paper [12], involves representing MD multilayered metamaterial as an uniaxial plasmonic crystal, whose optical axis is normal to the layers (in our case, the x-axis is the optical axis), a procedure that requires the metallic elements to have a size of a few nanometers. This is caused by the fact that transparency of noble metals is restrained to a propagation distance not surpassing the metal skin depth. In Ref. to this point, recent development of nanofabrication technology makes it possible to create such subwavelength structures. Under this condition, the plasmonic lattice behaves as a uniaxial crystal characterized by a relative permittivity tensor $\boldsymbol{\epsilon} = \epsilon_{\parallel}(\mathbf{x}\otimes\mathbf{x}) + \epsilon_{\perp}(\mathbf{y}\otimes\mathbf{y} + \mathbf{z}\otimes\mathbf{z})$, where

$$\epsilon_{\parallel} = \frac{\epsilon_1\epsilon_2}{(1-f)\epsilon_2 + f\epsilon_1}, \tag{36}$$

gives the permittivity along the optical axis, and $\epsilon_{\perp} = (1-f)\epsilon_1 + f\epsilon_2$ corresponds to the permittivity in the transversal direction. In the previous equations, $f = w_2/(w_1 + w_2)$, denotes the

filling factor of medium "2" providing the metal rate in a unit cell. The dispersion equations given by the EMA are $k_x^2 + k_t^2 = \epsilon_\perp k_0^2$, corresponding to TE (*o*-) waves, where k_x represents the Bloch wavenumber K_{TE}, and for TM (*e*-) waves, we have

$$\frac{k_x^2}{\epsilon_\perp} + \frac{k_t^2}{\epsilon_\parallel} = k_0^2, \tag{37}$$

being now k_x, the Bloch wavenumber K_{TM}.

The validity of the EMA is related on the assumption that the period Λ is much shorter than the wavelength, that is, $\Lambda \ll \lambda_0$. Apparently, Eq. (33) is in good agreement with the EMA in the vicinity of $k_x = 0$ for TM^x waves only. In contrast, propagation along the x-axis, where $k_y = k_z = 0$, results in large discrepancies. Even small-filling factors of the metallic composite lead to enormous birefringences. Such metamaterials enlarge the birefringence of the effective-uniaxial crystal at least in one order of magnitude in comparison with values shown in **Table 1**. However, the size of birefringence displayed by extraordinary waves is reduced if w_2 increases. On the other hand, the isotropy of the isofrequency curve is practically conserved for ordinary waves.

4.2. Hyperbolic media

As we have seen in Section 3.3, nanolayered metal-dielectric compounds behave like plasmonic crystals enabling a simplified description of the medium by using the long-wavelength approximation [10–12]. Under certain conditions, the permittivity of the medium set in the form of a second-rank tensor includes elements of opposite signs, leading to a metamaterial of extreme anisotropy [13, 14]. This class of nanostructured media with hyperbolic dispersion is promising metamaterials with a plethora of practical applications from biosensing to fluorescence engineering [15].

Type I hyperbolic media refers to a special kind of uniaxially anisotropic media, that can be described by a permittivity tensor where element $\epsilon_\parallel$ is negative and $\epsilon_\perp$ is positive. In this case, Eq. (37) leads to a two-sheet hyperboloid. Type II hyperbolic media lead to positive $\epsilon_\parallel$ and negative $\epsilon_\perp$, and Eq. (37) gives us a one-sheet hyperboloid [16]. The fulfillment of hyperbolic dispersion allows wave propagation over a wide spatial spectrum that would be evanescent in an ordinary isotropic dielectric. At the optical range, hyperbolic media can be manufactured with metal-dielectric multilayers or metallic nanowires. Multilayered hyperbolic metamaterials at an optical range take advantage of the wide frequency band in which metals exhibit negative permittivity and support plasmonic modes.

The system under analysis is a periodic binary medium, where we take as medium 1 a transparent dielectric medium that is ideally nondispersive. In our three numerical simulations we take a lossless Drude metal where its permittivity is $\epsilon_2 = 1 - \Omega^{-2}$ and dielectric media with permittivities: (a) $\epsilon_1 = 1$, (b) $\epsilon_1 = 2.25$ and (c) $\epsilon_1 = 11.55$. Note that frequencies can be expressed in units of the plasma frequency, $\Omega = \omega/\omega_p$.

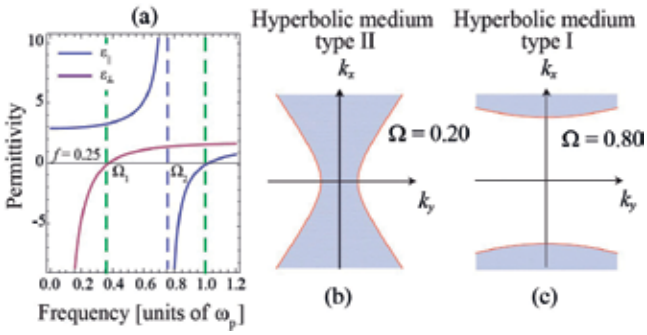

Figure 4. (a) Variation of relative permittivities $\epsilon_{\parallel}$ (blue solid line) and $\epsilon_{\perp}$ (magenta solid line) as a function of normalized frequency Ω, for the plasmonic crystal including a lossless Drude metal and fused silica ($\epsilon_1 = 2.25$) as dielectric material. Ω_1 and Ω_2 yield 0.359 and 0.759, respectively. (b) and (c) plot Eq. (37) in the $k_x k_y$ plane for extraordinary waves (TM^x modes) for a plasmonic effective crystal, including a dielectric of permittivity $\epsilon_1 = 2.25$, in the range $\Omega < 1$. Solid line corresponds to $k_z = 0$ and shaded regions are associated with harmonic waves with $k_z > 0$ (nonevanescent fields).

In **Figure 4(a)**, we represent the permittivities $\epsilon_{\parallel}$ and $\epsilon_{\perp}$ of our plasmonic crystals for a wide range of frequencies. Note that the metal-filling factor takes control on the dissipative effects in the metamaterial; accordingly low values of f are of great convenience. We set $f = 1/4$ in our numerical simulations. For low frequencies, $\Omega \ll 1$, the following approximations can be used: $\epsilon_{\perp} \approx f\epsilon_2 < 0$ and $0 < \epsilon_{\parallel} \approx \epsilon_1/(1-f)$. Therefore, propagating TE^x modes ($E_x = 0$) cannot exist in the bulk crystal since it behaves like a metal in these circumstances. On the other hand, TM^x waves propagate following the spatial dispersion curve of Eq. (37). This is a characteristic of Type II hyperbolic media. As mentioned earlier, Eq. (37) denotes a hyperboloid of one sheet (see **Figure 4(b)** for $\Omega = 0.20$).

Furthermore, the hyperbolic dispersion exists up to a frequency

$$\Omega_1 = \frac{1}{\sqrt{1 + \epsilon_1(1-f)/f}}, \tag{38}$$

for which $\epsilon_{\perp} = 0$. For slightly higher frequencies, both $\epsilon_{\parallel}$ and $\epsilon_{\perp}$ are positive and Eq. (37) becomes an ellipsoid of revolution. Since its minor semi-axis is $\Omega\sqrt{\epsilon_{\perp}}$, the periodic multilayer simulates a uniaxial medium with positive birefringence. Raising the frequency even more, $\epsilon_{\parallel}$ diverges at

$$\Omega_2 = \frac{1}{\sqrt{1 + \epsilon_1 f/(1-f)}}, \tag{39}$$

leading to the so-called canalization regime. In general, $\Omega_1 < \Omega_2$ provided that $f < 1/2$. Beyond Ω_2, Eq. (37) turns to a hyperboloidal shape. In the range $\Omega_2 < \Omega < 1$; however, the dispersion curve has two sheets (Type I hyperbolic medium). **Figure 4(c)** illustrates this case. Note that the upper limit of this hyperbolic band is determined by the condition $\epsilon_{\parallel} = 0$ or in an equivalent way, $\epsilon_2 = 0$, occurring at the plasma frequency.

5. Dyakonov surface waves

Dyakonov surface waves (DSWs) are another kind of surface waves, supported at the interface between an optically isotropic medium and a uniaxial-birefringent material. In the original work by Dyakonov (English version was reported in 1988 [3]), the optical axis of the uniaxial medium was assumed in-plane with respect to the interface. This is the case we deal with here.

The importance of DSWs for integrated optical applications, such as sensing and nano-waveguiding, was appreciated in a series of papers [17, 18]. Indeed Dyakonov-like surface waves also emerge in the case that a biaxial crystal [19] or a structurally chiral material [20] takes the place of the uniaxial medium. The case of metal-dielectric (MD) multilayers as structurally anisotropic media is especially convenient since small-filling fractions of the metallic inclusions enable metamaterials with an enormous birefringence, thus enhancing density of DSWs and relaxing their prominent directivity [21–23].

5.1. Dispersion equation of DSWs

The system under study is the plotted in **Figure 5**, where we have two semi-infinite media, one of them is isotropic and the second one is an MD lattice. In our case, the indices "1" and "2" make reference to the plasmonic lattice and the isotropic medium, respectively. We have previously reported a comprehensive analysis of this case in [4]. As we have seen earlier, the plasmonic lattice can be taken as an effective uniaxial crystal. In this case, the permittivity along its optical axis, $\epsilon_{z1} = \epsilon_{\parallel}$, is given by Eq. (36); also, the permittivity in the transverse direction $\epsilon_{x1} = \epsilon_{y1} = \epsilon_{\perp}$ may be appropriately averaged. From hereon, the permittivity ϵ_2 of the isotropic medium in $x > 0$ will be denoted by ϵ. Note that our analysis serves for natural birefringent materials characterized by permittivities $\epsilon_{\parallel}$ and $\epsilon_{\perp}$.

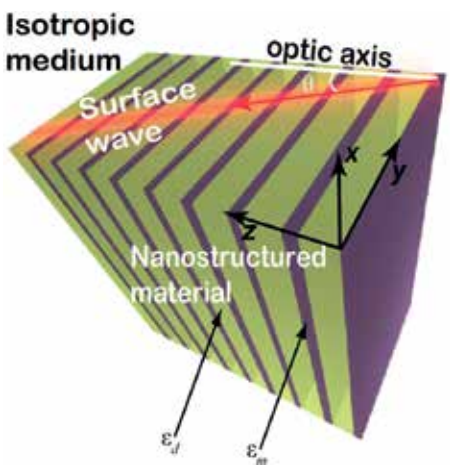

Figure 5. Schematic setup under study, consisting in a semi-infinite dielectric-metal superlattice ($x < 0$) and an isotropic substrate ($x > 0$).

Since we treat the plasmonic lattice as a uniaxial crystal, we may establish analytically the diffraction equation that gives the 2D wave vector $\mathbf{k}_D = \left[0, k_y, k_z\right]$ in $x = 0$. For that purpose, we follow Dyakonov [3] by considering hybrid-polarized surface modes. In the isotropic medium we consider TE^x ($E_x = 0$) and TM^x ($H_x = 0$) waves whose wave vectors have the same real components k_y and k_z in the plane $x = 0$. Therefore the electric field in both media may be set as

$$\mathbf{E}_{tot} = \mathbf{E}(x) \exp\left(ik_y y + ik_z z - i\omega t\right). \tag{40}$$

Moreover, these fields are evanescent in the isotropic medium and in the superlattice. In the anisotropic medium ($x < 0$) the evanescent electric amplitude can be written as

$$\mathbf{E}(x) = B_{o1}\, \hat{b}_{o1} \exp\left(-ik_{o1}x\right) + B_{e1}\, \hat{b}_{e1} \exp\left(-ik_{e1}x\right), \tag{41}$$

where the ordinary and extraordinary waves in the effective uniaxial medium decay exponentially with rates given by $\kappa_o = -ik_{o1}$ and $\kappa_e = -ik_{e1}$, respectively. Taking the formulation given in Section 2.3.1, the amplitudes A_{o1} and A_{e1} are identically zero. In the isotropic medium ($x > 0$) the amplitude of the electric field is

$$\mathbf{E}(x) = A'_{TE2}\, \hat{a}_{TE2} \exp\left(ik_{TE2}x\right) + A'_{TM2}\, \hat{a}_{TM2} \exp\left(ik_{TM2}x\right), \tag{42}$$

where the evanescent decay for TE and TM modes is $\kappa = -ik_{TE2} = -ik_{TM2}$. Now the amplitudes B'_{TE2} and B'_{TM2} are zero.

Once we have the amplitudes in both sides of the interface, we apply the boundary conditions at $x = 0$, $\mathbf{D}_1 \cdot \mathbf{v}_1 = \mathbf{D}_2 \cdot \mathbf{v}'_2$, where $\mathbf{D}_1$ is provided by Eq. (16), $\mathbf{D}_2$ from Eq. (26), $\mathbf{v}_1$ from Eq. (17), and $\mathbf{v}'_2$ from Eq. (27). This equation reduces to:

$$\begin{bmatrix} 0 \\ B_{o1} \\ 0 \\ B_{e1} \end{bmatrix} = \mathbf{M}_h \begin{bmatrix} A'_{TE2} \\ 0 \\ A'_{TM2} \\ 0 \end{bmatrix}, \tag{43}$$

where the transmission matrix $\mathbf{M}_h = \mathbf{D}_1^{-1} \cdot \mathbf{D}_2$ establishes a relationship between the amplitudes of *hybrid* polarization modes. Using the elements M_{ij} of the matrix $\mathbf{M}_h$, and defining $\mathbf{M}_i$ and $\mathbf{M}_a$ as

$$\mathbf{M}_i = \begin{bmatrix} M_{11} & M_{13} \\ M_{31} & M_{33} \end{bmatrix} = \begin{bmatrix} -\dfrac{ik_z(\kappa_o + \kappa)}{2\left(k_z^2 - k_0^2\epsilon_\perp\right)} & \dfrac{k_0^2 k_y(\epsilon\kappa_o + \kappa\epsilon_\perp)}{2\kappa_o\left(k_z^2 - k_0^2\epsilon_\perp\right)} \\ -\dfrac{(\kappa_e + \kappa)k_y}{2\kappa_e\left(k_z^2 - k_0^2\epsilon_\perp\right)} & -\dfrac{ik_z\left(\kappa\kappa_e\epsilon_\perp + \epsilon\kappa_o^2\right)}{2\kappa_e\epsilon_\perp\left(k_z^2 - k_0^2\epsilon_\perp\right)} \end{bmatrix}, \tag{44a}$$

$$\mathbf{M}_a = \begin{bmatrix} M_{21} & M_{23} \\ M_{41} & M_{43} \end{bmatrix} = \begin{bmatrix} \dfrac{ik_z(\kappa_o - \kappa)}{2\left(k_z^2 - k_0^2\epsilon_\perp\right)} & \dfrac{k_0^2 k_y(\epsilon\kappa_o - \kappa\epsilon_\perp)}{2\kappa_o\left(k_z^2 - k_0^2\epsilon_\perp\right)} \\ \dfrac{(\kappa - \kappa_e)k_y}{2\kappa_e\left(k_z^2 - k_0^2\epsilon_\perp\right)} & -\dfrac{ik_z\left(\kappa\kappa_e\epsilon_\perp - \epsilon\kappa_o^2\right)}{2\kappa_e\epsilon_\perp\left(k_z^2 - k_0^2\epsilon_\perp\right)} \end{bmatrix}. \tag{44b}$$

Eq. (43) can be rewritten as a set of two independent matrix equations, namely

$$\begin{bmatrix} 0 \\ 0 \end{bmatrix} = \mathbf{M}_i \cdot \begin{bmatrix} A'_{TE2} \\ A'_{TM2} \end{bmatrix}, \tag{45a}$$

$$\begin{bmatrix} B_{o1} \\ B_{e1} \end{bmatrix} = \mathbf{M}_a \cdot \begin{bmatrix} A'_{TE2} \\ A'_{TM2} \end{bmatrix}. \tag{45b}$$

Note that $\mathbf{M}_i$ governs the amplitudes A'_{TE2} and A'_{TM2} of the isotropic medium, and $\mathbf{M}_a$ (also $\mathbf{M}_h$) may be used to determine the amplitudes B_{o1} and B_{e1} of the *anisotropic* medium.

Dyakonov equation is obtained by means of letting the determinant of $\mathbf{M}_i$ equal to zero, giving

$$k_0^2 k_y^2 \epsilon_\perp (\kappa + \kappa_e)(\epsilon\kappa_o + \epsilon_\perp \kappa) = \kappa_o k_z^2 (\kappa + \kappa_o)\left(\epsilon\kappa_o^2 + \epsilon_\perp \kappa\kappa_e\right), \tag{46}$$

which provides a spectral map of allowed values (k_y, k_z). After fairly tedious algebraic transformations we can reduce Eq. (46) to a more convenient form [3].

$$(\kappa + \kappa_e)(\kappa + \kappa_o)(\epsilon\kappa_o + \epsilon_\perp \kappa_e) = \left(\epsilon_\parallel - \epsilon\right)(\epsilon - \epsilon_\perp) k_0^2 \kappa_o. \tag{47}$$

Assuming that $\epsilon_\parallel$, $\epsilon_\perp$ and all decay rates are positive, the additional restriction $\epsilon_\perp < \epsilon < \epsilon_\parallel$ can be deduced for the existence of surface waves. As a consequence, positive birefringence is mandatory to ensure a stationary solution of Maxwell's equations. Therefore, layered superlattices supporting Dyakonov-like surface waves cannot be formed by all dielectric materials [21].

5.2. DSWs in nano-engineered materials

To illustrate the difference between using conventional birefringent materials and plasmonic crystals, we solve Eq. (47) for liquid crystal E7 with $\epsilon_\parallel = 2.98$ i $\epsilon_\perp = 2.31$ at a wavelength of $\lambda_0 = 1.55\,\mu$ m and N-BAK1 substrate of dielectric constant $\epsilon = 2.42$. In this case, DSWs propagate in a narrow angular region $\Delta\theta = \theta_{max} - \theta_{min}$, where θ stands for the angle between the in-plane vector (k_y, k_z) and the optical axis. More specifically, the angular range yields $\Delta\theta = 0.92^\circ$ around the mean angle $\overline{\theta} = 26.6^\circ$. It appears that the resulting angular range $\Delta\theta$ is short. But this range would become much smaller when using other optical crystals like quartz, exhibiting a common birefringence. In order to gain in angular extent $\Delta\theta$, we consider a GaAs-Ag crystal ($\epsilon_1 = 12.5$ and $\epsilon_2 = -103.3$, where we neglect losses) that leads to values of $\epsilon_\parallel = 14.08$, derived from Eq. (36), and $\epsilon_\perp = 0.92$ with a metal-filling factor $f = 0.10$. Form birefringence now yields $\Delta n = 2.79$. Moreover, solutions to Eq. (47) can be found in the region of angles comprised between $\theta_{min} = 39.0^\circ$ and $\theta_{max} = 71.3^\circ$. It is important to point out that the total angular range of existence of DSWs, $\Delta\theta = 32.3^\circ$, grows by more than an order of magnitude. **Figure 6** shows the dispersion curve for DSWs; one can observe that θ_{min} is attained under the condition $\kappa = 0$ (red solid line), where TE^x and TM^x waves are uniform in

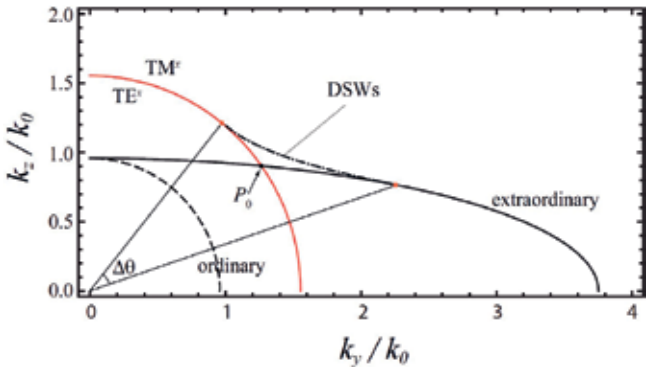

Figure 6. Dispersion Eq. (47) for DSWs (dotted-dashed line) propagating on the interface of a semi-infinite dielectric-metal lattice with metal filling factor f = 0.1. The solid elliptical line and the black dashed line are associated with homogeneous extraordinary waves ($\kappa_e = 0$) and homogeneous ordinary waves ($\kappa_o = 0$), respectively. The isofrequency curve ($\kappa = 0$) of isotropic N-BAK1 are represented in by the red solid line, which applies for TE^x and TM^x waves. Adapted with permission from [4] of copyright ©2013 IEEE photonics society.

the substrate $x > 0$. Looking at the other side of the dispersion curve, θ_{max} is established by $k_e = 0$, shown as a black solid line, for which the extraordinary wave will not decay spatially at $x \to -\infty$.

Consequently, the solution for Eq. (47) can be traced near the curves $\kappa = 0$ and $\kappa_e = 0$; thus, DSWs are always found close to the crosspoint $P_0(k_{y0}, k_{z0})$ of both curves.

5.2.1. Nonlocal effects

As we discussed in Section 4.1, the EMA is limited to metallic slabs' width $w_m \ll \lambda_0$. However, this condition must be taken into account with care, since the skin depth of noble metals is extremely short, $\delta \approx c/\omega_p$. For instance, we estimate $\delta = 24$ nm in the case of silver. If the metal thickness is comparable to its skin depth, the EMA will substantially deviate from exact calculations. Note that experimental studies from multilayer optics rarely incorporate metallic slabs with a thickness below 10 nm.

We emphasize that moderate changes in the birefringence of the plasmonic crystal will substantially affect the existence of DSWs. More specifically, an enlargement of $\epsilon_\perp$ driven by increasing w_m, provided f is fixed (see Section 4.1), will lead to a significant modification of the DSW dispersion curves. Ultimately, this phenomenon is clearly attributed to nonlocal effects in the effective-medium response of nanolayered metamaterials [24], which is associated with a strong variation of the fields on the scale of a single layer.

We conclude that, in order to excite DSWs, one may counterbalance the decrease of birefringence in the plasmonic lattice by means of a dielectric substrate of higher index of refraction. To illustrate this matter, the dispersion Eq. (47) for DSWs is represented in **Figure 7**, in addition to using the values of $\epsilon_\parallel$ and $\epsilon_\perp$ from nonlocal estimators [4]. When w_m grows but f is kept fixed, the dispersion curve of the Dyakonov surface waves tends to approach the optic axis.

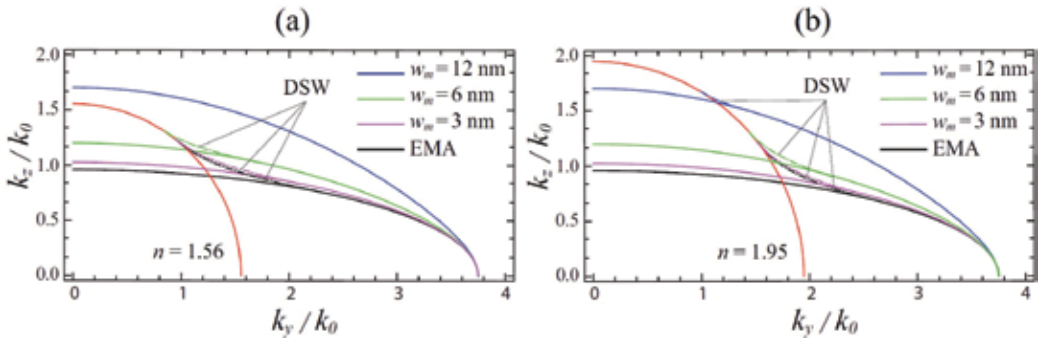

Figure 7. Solutions to Dyakonov equation, drawn in dotted-dashed lines, for a MD lattice with the same filling factor $f = 0.10$ but different w_m, using estimates from the nonlocal birefringence approach described in [4]. Note that the red solid line designates the isofrequency curve of isotropic substrate (a) N-BAK1 and (b) P-SF68. Adapted with permission from [4] of copyright ©2013 IEEE photonics society.

For an N-BAK1 substrate, as shown in **Figure 7(a)**, $\theta_{max} = 68.2^\circ$ and 58.7° for $w_m = 3$ nm and 6 nm, respectively. Also, $\theta_{min} = 37.6^\circ$ and 32.1° for these two cases. As a consequence the angular range $\Delta\theta$ shrinks when w_m increases. In the limit $\epsilon_\perp \to \epsilon$, which occurs for $w_m = 10.3$ nm using a N-BAK1 substrate, DSWs are not supported at the interface of the MD lattice and the isotropic dielectric. A substrate with greater relative permittivity ϵ would be necessary. For example, if we use a substrate with greater relative permittivity ϵ as P-SF68 [see **Figure 7(b)**], DSWs exist for $w_m = 12$ nm with an angular range $\Delta\theta = 12.5^\circ$.

5.2.2. Dissipative effects

Up to now, we have avoided another important aspect of plasmonic devices namely dissipation in metallic elements. In this regard, effective permittivities are fundamentally complex, and consequently the Dyakonov Eq. (47) is expected to give complex values of (k_y, k_z). This procedure has been discussed by Sorni et al. [25] recently. In order to tackle this problem, we evaluate numerically the value of the Bloch wavenumber k_z for a given real value k_y. The spatial frequency k_z becomes complex since $\mathrm{Im}[\epsilon_m] = 8.1$. As a consequence, the surface wave cannot propagate indefinitely, undergoing an energy attenuation given by $l = (2\mathrm{Im}[k_z])^{-1}$. Furthermore, we naturally assume that the real part of the parameters $\kappa, \kappa_o,$ and κ_e are all positive. These positive values correlate with a decay at $|x| \to \infty$ and thus with a confinement of the wave near $x = 0$.

Figure 8(a) depicts the dispersion curve corresponding to dissipative DSWs, for the case of a plasmonic MD lattice with $f = 0.10$ and $w_m = 12$ nm. We used a commercial software (COMSOL Multiphysics) based on the finite-element method (FEM) in order to perform our numerical simulations. We cannot observe surface waves by setting an N-BAK1 substrate with $n = 1.56$, suggesting that this is a retardation effect. More specifically, **Figure 8(a)** shows the isofrequency curves when $n = 1.95$, corresponding to P-SF68.

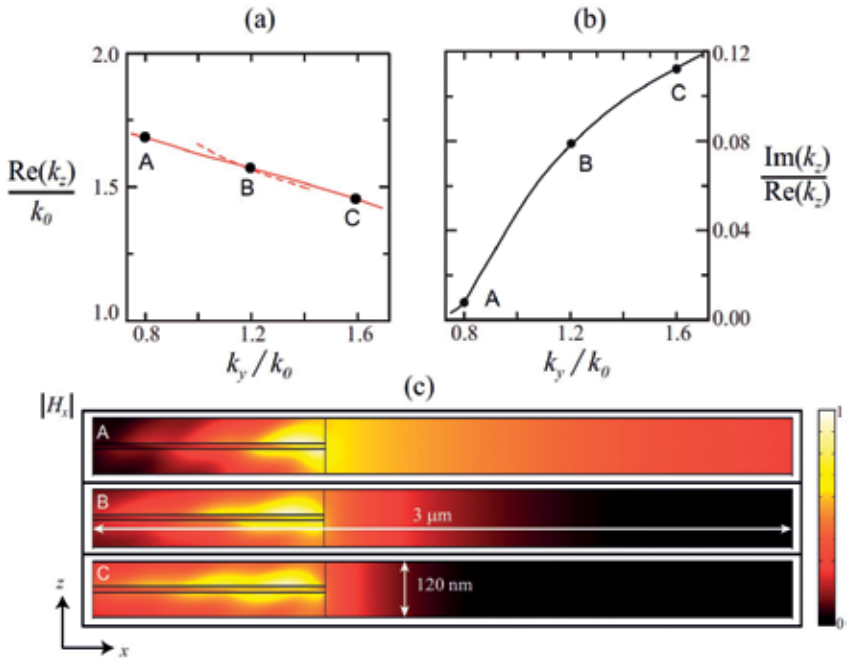

Figure 8. (a) Isofrequency curve that corresponds to hybrid surface waves existing at the boundary between a semi-infinite P-SF68 substrate and a lossy MD superlattice of $f = 0.10$ and $w_m = 12$ nm. (b) Ratio of Im(k_z) over re(k_z) representing dissipation effects in the propagation of DSWs. (c) Three contour plots of the magnetic field $|H_x|$ computed using the finite-element method. The superlattice is set on the left, for which only one period is represented. Capital letters a, B, and C, designate the transverse spatial frequencies $k_y = 0.8k_0$, $1.2k_0$, and $1.6k_0$, respectively. Adapted with permission from [4] of copyright ©2013 IEEE photonics society.

We observe that the dispersion curve for dissipative DSWs is flatter and larger than the curve obtained by neglecting losses. Specifically $\theta_{max} = 49.9^\circ$ and $\theta_{min} = 23.7^\circ$, giving an angular range $\Delta\theta = 26.2^\circ$. **Figure 8(b)** shows Im(k_z)/Re(k_z) in the range of existence of the surface waves. In these two figures, capital letters A, B, and C designate the transverse spatial frequencies $k_y = 0.8k_0$, $1.2k_0$, and $1.6k_0$, respectively. **Figure 8(c)** shows the magnetic field $|H_x|$ for the three different cases denoted by capital letters A, B, and C. Note that in the case of paraxial surface waves, for which k_y reaches a minimum value (case A), one achieves $\mathrm{Im}(k_z) \ll \mathrm{Re}(k_z)$ as depicted in **Figure 8(b)**. This is induced by an enormous shift undergone by the field maximum in the direction to the isotropic medium, as shown in **Figure 8(c)**, where dissipation effects are barely disadvantageous on surface-wave propagation. Moreover, this would be consistent with a condition $\mathrm{Re}(\kappa) \ll \mathrm{Re}(\kappa_e)$. On the other hand, for nonparaxial waves, having the largest values of k_y, the fields show slow energy decay inside the plasmonic superlattice. In case C, the magnetic field $|H_x|$ is localized around the metallic layer and takes significant values far from the boundary of the substrate. As a consequence, losses in the metal translate into a significant rise in the values of Im(k_z).

5.3. New families of DSWs in lossy media

In this section we carry out a thorough analysis of DSWs that takes place in lossy uniaxial metamaterials. Special emphasis is put when the effective-medium approach induces satisfactory results. The introduction of losses leads to a transformation of the isofrequency curves, which deviates from spheres and ellipsoids, as commonly considered by ordinary and extraordinary waves, respectively. As a consequence, one can find two different families of surface waves as reported by Sorni et al. [25]. One family of surface waves is directly related with the well-known solutions derived by Dyakonov [3]. Importantly, the existence of a new family of surface waves is revealed, closely connected to the presence of losses in the uniaxial effective crystal. We point out that the solutions to Dyakonov equation presented earlier are partial ones insofar as the z-component of the wavevector is kept real valued. Nevertheless, the whole set of solutions includes all possible wavevectors that feature a complex-valued k_x.

6. Dyakonov surface waves in hyperbolic media

In this section we perform a thorough analysis of DSWs taking place in semi-infinite MD lattices exhibiting hyperbolic dispersion. Part of this section was previously reported by Zapata-Rodríguez et al. [26]; we point out that recently further studies on DSW in hyperbolic metamaterials have been reported by other authors [27]. Our approach puts emphasis on the EMA. Under these conditions, different regimes can be found including DSWs with nonhyperbolic dispersion. The system under analysis is again as depicted in **Figure 5**. For simplicity, we assume that dielectric materials are nondispersive; indeed, we set $\epsilon = 1$ and $\epsilon_d = 2.25$ in our numerical simulations. Furthermore, Drude metals are included, and frequencies will be expressed in units of its plasma frequency, $\Omega = \omega/\omega_p$. Again, Dyakonov Eq. (47) provides the spectral map of wave vectors $\mathbf{k}_D = \left[0, k_y, k_z\right]$. Note that in this section, spatial frequencies will be expressed in units of k_p.

In the special case of the surface wave propagation perpendicular to the optical axis ($k_z = 0$), Eq. (47) reveals the following solution: $\epsilon\kappa_o + \epsilon_\perp\kappa = 0$. In the case: $\epsilon_\perp < 0$ and $\epsilon < |\epsilon_\perp|$, this equation has the well-known solution

$$k_y = \Omega\sqrt{\frac{\epsilon\epsilon_\perp}{\epsilon + \epsilon_\perp}}, \tag{48}$$

which resembles the dispersion equation of conventional SPPs [see Eq. (31)]. Here we have purely TM^x polarized waves, as expected. Note that no solutions to Eq. (47) can be found, in the form of surface waves, considering wave propagation parallel to the optical axis ($k_y = 0$) for hyperbolic metamaterials: $\epsilon_\perp\epsilon_\parallel < 0$. That means that a threshold value of k_y can be found for the existence of surface waves.

Next we describe a specific configuration governing DSWs, subject to a low value of the refractive index $n = \sqrt{\epsilon}$, namely $\epsilon < \epsilon_\parallel$ ($\epsilon < \epsilon_\perp$) occurring at low and moderate frequencies;

other cases are treated elsewhere [26]. In the effective-uniaxial medium, it is easy to realize that $\kappa < \kappa_o$ and also $\kappa_e < \kappa_o$. Under these circumstances, all brackets in Dyakonov Eq. (47) are positive provided $\epsilon\kappa_o + \epsilon_\perp\kappa_e > 0$. This happens within the spectral band $\Omega_0 < \Omega < \Omega_1$, where

$$\Omega_0 = \frac{1}{\sqrt{1 + \epsilon/f + \epsilon_d(1-f)/f}}. \tag{49}$$

Note that $\Omega_0 = 0.292$ in our numerical simulation.

In **Figure 9(a)** and **(b)**, we illustrate the dispersion equation of DSWs for two different frequencies within the spectral range $0 < \Omega < \Omega_0$. In these cases, the dispersion curve approaches a hyperbola. We find a bandgap around $k_z = 0$ in **Figure 9(a)**, unlike what occurs in (b). Note that hybrid solutions near $k_z = 0$ are additionally constrained to the condition $k_y \geq \Omega\sqrt{\epsilon_\parallel}$ [see also Eq. (48)], which is a necessary condition for κ_e to exhibit real and positive values. We consider the quasi-static regime ($\Omega \to 0$) where $|\mathbf{k}_D| = k_D \gg \Omega$ to determine the asymptotes of the hyperbolic-like DSW dispersion curve. Under this approximation, $\kappa = k_D$, $\kappa_o = k_D$ and $\kappa_e = \Theta k_D$, where

$$\Theta = \sqrt{\cos^2\theta + (\epsilon_\parallel/\epsilon_\perp)\sin^2\theta}, \tag{50}$$

being $k_y = k_D\cos\theta$ and $k_z = k_D\sin\theta$. These asymptotes establish a canalization regime leading to a collective directional propagation of DSW beams [4, 28]. At this point it is necessary to remind that the asymptotes of the *e*-waves dispersion curve, in the k_yk_z plane, have slopes satisfying the condition $\theta_D < \theta_e$, as illustrated in **Figure 9(b)**.

In the high-frequency band $\Omega_2 < \Omega < 1$ we find that $\epsilon_\parallel < 0 < \epsilon_\perp$, as occurs in **Figure 9(c)**. Note the relevant proximity of DSW dispersion curve to $\kappa_e = 0$, the same way we also find in **Figure 9(a)** and **(b)**. Conversely it crosses the *e*-wave hyperbolic curve at two different points,

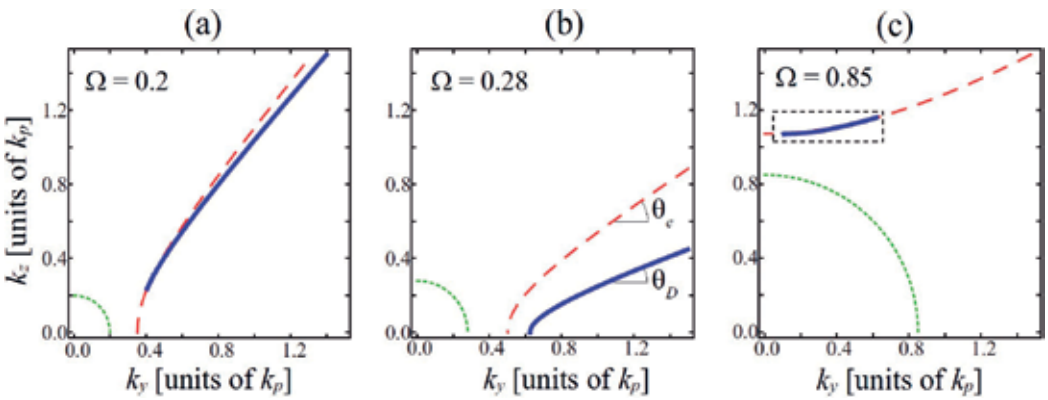

Figure 9. Solutions to Eq. (47), drawn in solid line, providing the spatial dispersion of DSWs which can exist in the arrangement of **Figure 5**, at different frequencies: (a) $\Omega = 0.20$, (b) $\Omega = 0.28$, and (c) $\Omega = 0.85$. Here, the isotropic medium is air and the multi-layered metamaterial has a filling factor $f = 0.25$ and. Also, we include equations $\kappa = 0$ (dotted line) and $\kappa_e = 0$ (dashed line). Adapted with permission from [26] of copyright ©2013 Optical Society of America.

where solutions to the Dyakonov equation begin and end, respectively. It is clear that the angular range of DSWs now turns to be significantly low.

6.1. DSWs in band-gap hyperbolic media

In previous sections we demonstrated that the presence of metallic nano-elements leads to nonlocal effects and dissipation effects which reshape the propagation dynamics of the surface signal. Here, we briefly discuss the extraordinary favorable conditions which may appear in band-gap metal–insulator-layered media for the existence of DSWs. As reported thoroughly by Miret et al. [29], engineering secondary bands by tuning the plasmonic-crystal geometry may lead to a controlled optical anisotropy, which is markedly dissimilar to the prescribed hyperbolic regime that is derived by the EMA, however, assisting the presence of DSWs on the interface between such hyperbolic metamaterial and an insulator.

In particular, a surface wave propagating on an Ag-Ge grating was considered, where the environment medium that is set above the metallic grating is formed by SiO_2. If the metal-filling factor was $f = 0.25$, the effective permittivities of the anisotropic metamaterial would be estimated as $\epsilon_\perp = -11.48 + i2.05$ and $\epsilon_\parallel = 25.96 + i0.14$ at a wavelength of $\lambda_0 = 1550$ nm. Disregarding losses, the DSW dispersion curve describes an incomplete hyperbolic curve, finding an endpoint under the condition $\kappa_e = 0$, where the extraordinary wave breaks its confinement in the vicinities of the isotropic-uniaxial interface [26].

Considering now a realistic nanostructure consisting of Ag layers of $w_2 = 40$ nm interspersed between Ge layers of $w_1 = 120$ nm, thus maintaining a metal-filling factor of $f = 0.25$ as analyzed earlier, a first TM band with hyperbolic-like characteristics dominates at high in-plane frequencies k_t. Additionally, a second band emerges for TM Bloch modes, which exhibits a moderate anisotropy, demonstrating near-elliptical dispersion curves (with positive effective permittivities) and positive birefringence. Furthermore, TE modal dispersion is roughly isotropic. Therefore, satisfactory conditions are found near the second TM band for the existence of Dyakonov-like surface waves. Finally, in order to numerically obtain the dispersion curves and wave fields associated with DSWs, one may follow the same computational procedure followed by Zapata-Rodríguez et al. and [4, 26].

7. Summary

In this chapter we provide several methods to analytically calculate and numerically simulate modal propagation of DSWs governed by material anisotropy. We focused on the spatial properties of DSWs at optical and telecom wavelengths, particularly using uniaxial metamaterials formed of dielectric and metallic nanolayers. We developed an electromagnetic matrix procedure enabling different aspects reviewed in this chapter, specially adapted to complex multilayered configurations. The EMA results are particularly appropriate for the characterization of the form birefringence of a multilayered nanostructure, though limitations driven by the layers width have been discussed. Through a rigorous full-wave analysis, we

showed that hybrid-polarized surface waves may propagate obliquely at the boundary between a plasmonic bilayer superlattice and an isotropic loss-free material. We revealed that realistic widths of the slabs might lead to solutions which deviate significantly from the results derived directly from the EMA and Dyakonov analysis. Finally, we showed that excitation of DSWs at the boundary of an isotropic dielectric and a hyperbolic metamaterial enables a distinct regime of propagation. It is important to note that the properties of the resulting bound states change drastically with the index of refraction of the surrounding medium, suggesting potential applications in chemical and biological sensing and nanoimaging.

This chapter was supported by the Qatar National Research Fund (Grant No. NPRP 8-028-1-001) and the Spanish Ministry of Economy and Competitiveness (Grants No. TEC2014-53727-C2-1-R and TEC2017-86102-C2-1R).

Author details

Carlos J. Zapata-Rodríguez[1]*, Slobodan Vuković[2,3], Juan J. Miret[4], Mahin Naserpour[1,5] and Milivoj R. Belić[3]

*Address all correspondence to: carlos.zapata@uv.es

1 Departament of Optics and Optometry and Vision Science, University of Valencia, Burjassot, Spain

2 Center of Microelectronic Technologies, Institute of Chemistry, Technology and Metallurgy (IHTM), University of Belgrade, Belgrade, Serbia

3 Texas A&M University at Qatar, Doha, Qatar

4 Department of Optics, Pharmacology and Anatomy, University of Alicante, Alicante, Spain

5 Department of Physics, College of Sciences, Shiraz University, Shiraz, Iran

References

[1] Zenneck J. Über die Fortpflanzung ebener elektromagnetischer wellen längs einer ebenen Lieterfläche und ihre Beziehung zur drahtlosen Telegraphie. Annalen der Physik (Leipzig). 1907;**23**:846-866

[2] Maier SA. Plasmonics: Fundamentals and Applications. New York: Springer; 2007

[3] D'yakonov MI. New type of electromagnetic wave propagating at an interface. Sov. Phys. JETP. 1988;**67**:714-716

[4] Zapata-Rodríguez CJ, Miret JJ, Sorni JA, Vuković SM. Propagation of dyakonon wave-packets at the boundary of metallodielectric lattices. IEEE Journal of Selected Topics in Quantum Electronics. 2013;**19**:4601408

[5] Takayama O, Crasovan LC, Johansen SK, Mihalache D, Artigas D, Torner L. Dyakonov surface waves:A review. Electromagnetics. 2008;**28**:126-145

[6] Berreman DW. Optics in stratified and anisotropic media: 4×4 matrix formulation. Journal of the Optical Society of America. 1972;**62**(4):502-510

[7] Hodgkinson IJ, Kassam S, Wu QH. Eigenequations and compact algorithms for bulk and layered anisotropic optical media: Reflection and refraction at a crystal-crystal interface. Journal of Computational Physics. 1997;**133**(1):75-83

[8] Barnes WL, Dereux A, Ebbesen TW. Surface plasmon subwavelength optics. Nature. 2003; **424**(6950):824

[9] Zayats AV, Smolyaninov II, Maradudin AA. Nano-optics of surface plasmon polaritons. Physics Reports. 2005;**408**:131-314

[10] Yariv A, Yeh P. Electromagnetic propagation in periodic stratified media. II. Birefringence, phase matching, and x-ray lasers. Journal of the Optical Society of America. 1977; **67**:438-448

[11] Vuković SM, Shadrivov IV, Kivshar YS. Surface Bloch waves in metamaterial and metal-dielectric superlattices. Applied Physics Letters. 2009;**95**:041902

[12] Rytov SM. Electromagnetic properties of a finely stratified medium. Soviet Physics - JETP. 1956;**2**:466-475

[13] Smith DR, Schurig D, Rosenbluth M, Schultz S. Limitations on subdiffraction imaging with a negative refractive index slab. Applied Physics Letters. 2003;**82**:1506-1508

[14] Smolyaninov II, Hwang E, Narimanov E. Hyperbolic metamaterial interfaces: Hawking radiation from Rindler horizons and spacetime signature transitions. Physical Review B. 2012;**85**:235122

[15] Guo Y, Newman W, Cortes CL, Jacob Z. Applications of hyperbolic metamaterial substrates. Advances in OptoElectronics. 2012;ID 452502

[16] Cortes CL, Newman W, Molesky S, Jacob Z. Quantum nanophotonics using hyperbolic metamaterials. Journal of Optics. 2012;**14**:063001

[17] Takayama O, Crasovan L, Artigas D, Torner L. Observation of Dyakonov surface waves. Physical Review Letters. 2009;**102**:043903

[18] Takayama O, Artigas D, Torner L. Lossless directional guiding of light in dielectric nanosheets using Dyakonov surface waves. Nature Nanotechnology. 2014;**9**:419-424

[19] Walker DB, Glytsis EN, Gaylord TK. Surface mode at isotropic uniaxial and isotropic-biaxial interfaces. Journal of the Optical Society of America. A. 1998;**15**:248-260

[20] Gao J, Lakhtakia A, Lei M. Dyakonov-Tamm waves guided by the interface between two structurally chiral materials that differonly in handedness. Physical Review A. 2010;**81**: 013801

[21] Vuković SM, Miret JJ, Zapata-Rodríguez CJ, Jaksić Z. Oblique surface waves at an interface of metal-dielectric superlattice and isotropic dielectric. Physica Scripta. 2012;**T149**: 014041

[22] Ghasempour Ardakani A, Naserpour M, Zapata Rodríguez CJ. Dyakonov-like surface waves in the THz regime. Photonics and Nanostructures - Fundamentals and Applications. 2016;**20**:1-6

[23] Miret JJ, Zapata-Rodrïguez CJ, Jaksić Z, Vuković SM, Belić MR. Substantial enlargement of angular existence range for Dyakonov-like surface waves at semi-infinite metal-dielectric superlattice. Journal of Nanophotonics. 2012;**6**. DOI: 063525

[24] Elser J, Podolskiy VA, Salakhutdinov I, Avrutsky I. Nonlocal effects in effective-medium response of nanolayered metamaterials. Applied Physics Letters. 2007;**90**:191109

[25] Sorni JA, Naserpour M, Zapata-Rodríguez CJ, Miret JJ. Dyakonov surface waves in lossy metamaterials. Optics Communication. 2015;**355**:251-255

[26] Zapata-Rodríguez CJ, Miret JJ, Vuković S, Belić MR. Engineered surface waves in hyperbolic metamaterials. Optics Express. 2013;**21**:19113-19127

[27] Xiang Y, Guo J, Dai X, Wen S, Tang D. Engineered surface Bloch waves in graphene-based hyperbolic metamaterials. Optics Express. 2014;**22**:3054-3062

[28] Jacob Z, Narimanov EE. Optical hyperspace for plasmons: Dyakonov states in metamaterials. Applied Physics Letters. 2008;**93**:221109

[29] Miret JJ, Sorní JA, Naserpour M, Ghasempour Ardakani A, Zapata-Rodríguez CJ. Nonlocal dispersion anomalies of Dyakonov-like surface waves at hyperbolic media interfaces. Photonics and Nanostructures - Fundamentals and Applications. 2016;**18**:16-22

Chapter 4

Measurement of Sea Wave Spatial Spectra from High-Resolution Optical Aerospace Imagery

Valery G. Bondur and Alexander B. Murynin

Additional information is available at the end of the chapter

http://dx.doi.org/10.5772/intechopen.71834

Abstract

The chapter is devoted to the development of methods for remote measurement of spatial spectra of waves arising on marine and ocean surface. It is shown that in most natural conditions of optical image formation, a nonlinear modulation of the brightness field occurs by slopes of water surface elements. Methods for reconstructing the spectra of surface waves from optical image spectra with allowance for such modulation are proposed. The methods are based on the numerical simulation of water surface taking into account wave formation conditions and conditions of light entering the sea surface from the upper and lower hemispheres. Using the results of numerical simulation, special operators are built to retrieve wave spectra from the spectra of aerospace images. These retrieving operators are presented in the form of analytical expressions, depending on the sets of parameters, which are determined by the conditions for the formation of images. The results of experimental studies of the sea wave spectra in various water areas using satellite optical images of high spatial resolution are presented. In the experimental studies, the spatial spectral characteristics of sea waves estimated from remote sensing data were compared with the corresponding characteristics measured by contact assets under controlled conditions.

Keywords: wave spectra, surface waves, remote sensing, image processing

1. Introduction

Registration of spatial spectra of surface waves is actual in solving many fundamental and applied problems of modern oceanology [1–3]. Obtaining information about such spectra is important for studying various physical processes occurring near the ocean-atmosphere interface, detecting water pollution, and monitoring anthropogenic impacts on the marine areas [1, 4–12].

To obtain two-dimensional spectra of surface waves in large water areas, including hard-to-reach ones, the use of remote sensing methods based on the processing of various images obtained from air carriers and also space images of high spatial resolution is promising [4, 13–15].

An adequate estimation of such spectra formed by image processing obtained in the process of aerospace monitoring of marine areas of the seas and oceans requires the use of reconstructing operators that are functions that allow the spatial spectra of brightness fields recorded in optical aerospace images to be transformed into sea wave spectra [4, 16–18, 24]. These operators are built using numerical simulation methods based on the various conditions for the formation of aerospace images and the characteristics of remote sensing equipment [4, 16–21]. Initially, these methods were used to construct retrieving operators, which allow us to obtain wavelet spectra in the equilibrium interval [16–18]. At the present time, the development of modified retrieving operators, which are a superposition of the high-frequency and low-frequency components, is being developed and is suitable for use in the low-frequency region, including near the spectral maximum [17, 18].

This chapter describes a method for retrieving sea wave spectra from the spectra of aerospace optical images over a wide range of spatial frequencies, including the equilibrium interval, the spectral maximum, and the low-frequency region. To calibrate and verify the adequacy of the developed method, the contact data obtained in synchronous measurements with the help of an array of string wave recorders are used. The results of experimental studies carried out using the developed method are presented.

2. An approach to retrieve marine surface spectra

Rough sea surface is a random field of elevations (wave applications).

$$z = \zeta\,(x, y, t) \tag{1}$$

where $\zeta\,(x, y, t)$ is random function of sea surface elevations (elevation field); (x, y, z) is a rectangular Cartesian coordinate system in which the (x, y) plane coincides with the level of a calm (undisturbed) water surface; t is time.

Fixing the time instant $t = t_0$ in (1), we obtain a two-dimensional random function of spatial coordinates:

$$z = \zeta\,(x, y, t)|_{t=t0} = \xi(x, y) \tag{2}$$

Aerospace images, which are recorded by remote methods, are used to study the characteristics of the sea surface elevation field at a fixed time $z = \xi\,(x, y)$. Two-dimensional signal fields that are represented in aerospace images are associated with the sea surface elevation field and can be used to estimate significant characteristics of this surface.

Since the sea surface elevation field (x, y) is a Gaussian quasistationary field, it is described quite adequately by the spectral density [2]:

$$\Psi(\mathbf{k}) = \mathbf{S}[\xi](\mathbf{k}) \tag{3}$$

where **S** is the spectral density operator, which is proportional to the square of the modulus of the Fourier transform of the field $\xi(x, y)$; $\mathbf{k} = (k_x, k_y)$ is the wave vector.

Since optical images of the sea surface are formed as a result of reflection and refraction of light according to the laws of geometrical optics, for their analysis, the structure of the sea surface along with the field of elevations (x, y) is conveniently characterized by fields of slopes (or gradients) along the axes [2, 4, 17].

$$\xi_x(x, y) = \partial\xi(x, y)/\partial x,\ \xi_y(x, y) = \partial\xi(x, y)/\partial y \tag{4}$$

The gradient of the sea surface in an arbitrary direction ϕ, with allowance for (3), can be expressed as follows:

$$\xi_\phi(x, y) = \cos\phi\xi_x(x, y) + \sin\phi\xi_y(x, y) \tag{5}$$

Taking into account the properties of the Fourier transform, one can associate the spectrum of such a field of slopes with the spectrum of the field of elevations:

$$\Phi(\mathbf{k}) = \left(\cos\phi\ k_x + \sin\phi\ k_y\right)\Psi(\mathbf{k}) \tag{6}$$

The brightness field, recorded by the remote sensing equipment at a fixed time, can be expanded in a power series along the surface slopes and is represented in the form [1, 11, 12]:

$$L(x, y) = C_0 + C_x\xi_x(x, y) + C_y\xi_y(x, y) + N(x, y, \xi_x(x, y), \xi_y(x, y)) \tag{7}$$

where N is the nonlinear component of the signal, containing terms proportional to $(\xi_x(x,y))^2$, $(\xi_y(x,y))^2$, and so on. C_0, C_x, and C_y are coefficients of the linear part of the expansion and $\xi_x(x,y)$ and $\xi_y(x,y)$ are fields of slopes (gradients of the elevation field) of the sea surface.

The contribution to the detected signal of the nonlinear component N (x, y, ξx, ξy) is determined by a number of parameters: lighting conditions, wave state, and recording equipment characteristics [4, 17].

In order to change from the spectrum of the optical image S(**k**), obtained under known conditions, to the slope spectrum of the sea surface Φ(k) in the direction determined by these conditions, the definition of the retrieving operator **R** is introduced as:

$$\Phi(\mathbf{k}) = \mathbf{R}S(\mathbf{k}) \tag{8}$$

As a rule, analytical estimates of the contribution of the nonlinear component of N to the spatial spectrum of the luminosity field are difficult; therefore, the numerical simulation method is used to solve the problem of constructing the recovery operator [1, 11–13].

The method of constructing the retrieving operator developed and described in this chapter is an extension of the method proposed in [1, 5, 6, 10–14]. To construct a retrieving operator corresponding to certain image acquisition conditions, direct numerical modeling of optical

images is performed under a given set of conditions [8–11], after which an approximation of the spatial frequency filter (transfer function) [11–14] is constructed, which allows obtaining a spatial spectrum of sea surface slopes from the aerospace image spectrum.

Parametrization of the spatial-frequency filter using a set of parameters that depends on the experimental conditions was proposed in [21]. The adequacy of the parametrization was experimentally verified in the equilibrium interval using contact data obtained by wave recorders and also by stereoscopic photography from the oceanographic platform [22].

However, the operator obtained in [21] does not allow for reconstructing the wave spectra in the region of low spatial frequencies and near the spectral maximum. To eliminate this shortcoming, an improvement was made to the method of constructing the retrieving operator and its approbation in various conditions [20, 19].

The modified retrieving operator $\mathbf{R}_{\text{mod}}$ is represented as the product of two operators (transfer functions):

$$\mathbf{R}_{\text{mod}}(\mathbf{k}) = \mathbf{R}_{\text{low}}(\mathbf{k})\mathbf{R}_{\text{high}}(\mathbf{k}) \tag{9}$$

where R_{high} is a recovery operator (transfer function) in the high-frequency region; R_{low} is a recovery operator (transfer function) in the low-frequency range.

An approximation of the retrieving operator in the form

$$\mathbf{R}(\mathbf{k}) = a_0\left(\exp\left(a_4 k^{a_5}\right)\right)\left(\cos\left(\varphi - \varphi_c\right)\right)^{a_3} k^{a_1 + a_2\cos\left(\varphi - \varphi_c\right)} \tag{10}$$

where the parameter vector $\boldsymbol{a} = (a_0, a_1, a_2, a_3, a_4, a_5)$ is formed on the basis of experimental data obtained in complex experiments, including remote and in situ measurements of wave spectra.

3. Calibration and verification of the adequacy of remote methods

When verifying the adequacy of remote methods of measuring wave spectra, sea truth data obtained in specially conducted experiments under controlled conditions using reference techniques and means ensuring the measurement of the sea surface spectra with sufficient accuracy should be used. As such methods and means in this chapter, measurements of sea surface elevations made using a grid of string wave recorders, stereo photography from low altitudes, and measurements using wave buoys will be used.

In an experimental verification of the reliability of methods for recording wave spectra from the spectra of satellite images, we will make a quantitative comparison of the results of remote measurements with data obtained by direct measurements by contact methods.

Having obtained under the same conditions the results of remote measurements of instantaneous two-dimensional fields of slopes and elevations, as well as data of direct (contact) measurements of local time series of heights, and also using the method of comparing spatial

and temporal characteristics of sea waves based on the corresponding hydrodynamic models, it is possible to calibrate remote sensing assets for measuring sea surface characteristics.

As sources of information for comparing the results of remote and direct contact measurements of sea surface characteristics, we will use the following types of measurements:

- Measurements in which temporal sequences of elevations of the sea surface are formed using stationary contact sensors.
- Measurements using wave buoys drifting in the space survey area.
- Stereo-photogrammetric measurements performed from close distances and allowing us to directly measure the two-dimensional realizations of the sea surface elevation field with high spatial resolution.

For direct determination of characteristics of sea waves, contact methods usually employ arrays of sensors (wave recorders) measuring the parameters of sea surface (gradient, elevation, and acceleration) at one or several points spaced from each other by some distance. To estimate spatiotemporal spectra from the arrays of wave recorders, indirect iterative calculation methods are widely used, in which some hypotheses about the statistical properties of wave are postulated.

The stereo-photogrammetric processing of synchronously registered optical images of the sea surface from two different points of view (stereopairs) makes it possible to directly measure the realizations of two-dimensional fields of sea surface elevations, and calculate spatial spectra of elevations on the base of these realizations.

The stereo-photogrammetric method allows measuring the shape of rough sea surface. The drawbacks of this method include the greater complexity of processing primary data and high demands on the computing resources used.

To compare the frequency and frequency-directed wave spectra recorded by wave recorders with two-dimensional and one-dimensional spatial spectra of sea surface elevations recorded by remote data, it is necessary to develop a special approach that takes into account the features of gravitational and gravitational-capillary waves.

Taking into account the features considered, the present chapter proposes an approach to comparing satellite and contact measurements, which consists of the following:

- Conducting experiments under controlled conditions, including satellite imagery of sea surface test areas and synchronous measurements using contact equipment and/or stereo-photogrammetric imagery of the sea surface from a low altitude.
- Retrieving sea surface spectra from space images under fixed conditions for obtaining these images.
- Calculation of frequency spectra of waves from contact data obtained by wave recorders.
- Formation of wave spectra from the satellite data of stereo-photogrammetric image processing.

- Comparison of wave spectra obtained remotely with contact and/or stereo-photogrammetric measurements.

Consider the relationship between the spatial spectra of the sea surface, reconstructed from optical images, as well as frequency and frequency-directed wave spectra, measured by contact sensors, and characterize the fluctuations in sea level over time at a fixed point.

The frequency spectrum of sea surface elevations $S_\xi(\omega)$ characterizes the distribution of wave oscillations at a given point along the cyclic frequencies ω, $\omega = 2\pi/\tau$, where τ is the period of the wave oscillation.

The spatial wave spectrum characterizes the energy distribution at a fixed time instant with respect to wave numbers k (or spatial frequencies $\nu = 1/\Lambda$), $k = 2\pi/\Lambda$, where Λ is the length of the surface wave.

Spatial and frequency spectra of waves are functions of different arguments. They have different physical meanings and require the use of different methods of measurement. Therefore, to compare the spectra measured by different methods, a dispersion relation is used that describes the relationship between the time and spatial frequencies of waves, depending on the physical mechanisms that form the surface waves of the range in question. Within the framework of the linear hydrodynamic model, the components of the wave spectrum can be considered as elementary plane waves, for which the dispersion relation of the theory of potential waves of small amplitude that relates the cyclic frequency of the wave (ω) to the wave number k is valid. In deep water (for $kh \gg 1$, where h is the depth), the dispersion relation taking into account the contribution of gravitational and capillary forces to wave formation has the form

$$\omega(k) = \sqrt{gk + (T/\rho)k^3} \tag{11}$$

For gravitational waves (for $\Lambda > 10^{-1}$ m), the relation (11) is simplified and takes the form

$$\omega(k) = \sqrt{gk} \tag{12}$$

The dispersion relation makes it possible to establish a relationship between the spatial spectrum of χ(k) characterizing the total energy of waves with a wave number k propagating in all possible directions and a frequency spectrum S(ω) characterizing the total energy of waves with a cyclic frequency ω propagating in all possible directions

$$\chi(k) = S\,(\omega(k))d\omega(k)\,dk. \tag{13}$$

On the other hand, a one-dimensional spatial spectrum can be obtained from the two-dimensional spectrum of sea surface elevations Ψ(k) by integrating over the azimuth

$$\chi(k) = \int_{-\pi/2}^{\pi/2} \Psi(k\cos\varphi, k\sin\varphi)kd\varphi \tag{14}$$

Thus, the spectrum $\chi(k)$ can be used as a base function and recalculate the spectra obtained by various measurement methods in this spectrum by means of appropriate transformations.

http://dx.doi.org/10.5772/intechopen.71834

4. The results of experimental studies

To solve the problems of validation of the developed methods, the results obtained in three types of experiments were used [19, 22]:

- The first type of experiments consisted of carrying out space surveys and synchronous sea truth measurements of wave spectra near the stationary oceanographic platform.
- The second type of experiments consisted of carrying out a space survey of the investigated water area and simultaneous measurements of wave spectra with the help of drifting wave buoys.
- The third type of experiments consisted of carrying out studies in the short-wave region of wave spectra (Λ = 0.04–1.0 m) with the help of string wave recorders, object photography and stereo survey from the deck of the oceanographic platform.

Let us briefly summarize some experimental results of these types.

Experimental work of the first type was carried out in the area of the oceanographic platform (Katsiveli settlement, Crimea), installed at a distance of about 600 m from the shore.

For the measurement of space-time wave spectra, contact data obtained using a wave measuring unit based on an array of string wave recorders, which were a set of six resistive wave recorders measuring the elevations of the sea surface at points located in the center and at the top of the pentagon, were used.

The distance from the central string to each of the external strings was 25 cm. The main technical characteristics of this complex were as follows:

- Resolution—no worse than 3 mm
- Number of measuring channels—6
- Frequency of interrogation of channels—10, 20, 50, and 100 Hz
- The maximum height of the measured waves was up to 4 m.

During the first type of experiments, a special space imagery was conducted in the vicinity of the oceanographic platform using high-spatial resolution (0.5 m) optic-electronic equipment installed on board the GEOEYE spacecraft. A brief overview of the complex experiments conducted on September 24, 2015 at 11:52 (LT) and on September 12, 2011 at 12:06 is presented below. The presented experiments were characterized by different conditions of wave formation. During the first complex experiment, developing wind waves were observed at a near-surface wind speed of about 4 m/s. During the second complex experiment, the velocity of the near-surface wind varied from 0 to 2 m/s; however, swell waves were present in the experiment zone.

Figures 1 and **2** show the results of a joint analysis of sea wave spectra obtained from satellite and contact data under various wave formation conditions. **Figure 1** shows the results of an experiment conducted on September 24, 2015 under the conditions of developing wind waves, and **Figure 2** shows the results experiment, conducted on September 12, 2012 with weak wind

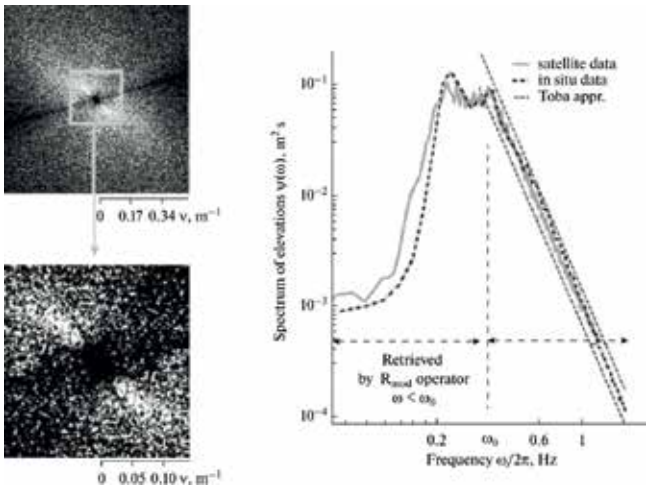

Figure 1. Comparison of the spectra of developing wind waves measured from remote and contact data of the complex experiment. September 24, 2015: (a) and (b) two-dimensional slope spectrum recovered in two intervals of spatial frequencies; (c) comparison of the one-dimensional frequency spectrum of the elevations obtained from the two-dimensional spectrum of slopes by the retrieving operator R, with the spectrum obtained from the data of the string wave recorder. The dashed lines denote the Toba approximation [23].

waves in the presence of swell waves [19, 20]. **Figures 1(a)** and **2(a)** show the reconstructed spatial spectra of sea surface slopes in a wide range of spatial frequencies, and **Figures 1(b)** and **2(b)** show the slope spectra in the region of the spectral maximum and low spatial frequencies are enlarged.

Figures 1(c) and **2(c)** show a comparison of the one-dimensional frequency spectrum of the elevations obtained from the two-dimensional spectrum of slopes with the frequency spectrum of the elevations obtained from the data of the array of string wave recorders. The conjugated spectra conditionally show the boundary ω_0 between the frequency domains corresponding to the regions of action of the high-frequency and low-frequency reconstructing operators included in the formula (9) [20].

The comparison of the graphs of one-dimensional frequency spectra of waves, shown in **Figures 1** and **2**, allows us to visually evaluate the good correspondence between the spectra measured by contact data and spectra reconstructed from remote data.

For the quantitative analysis of the correspondence between the results of remote and contact measurements, a measure of discrepancy was used, calculated from formula

$$\Delta = \sqrt{(1/N)\sum_{n=1}^{N}\left(1 - \Psi_{cn}(\omega_n)/\Psi_{contact}(\omega_n)\right)^2} \tag{15}$$

For the complex experiment carried out on September 24, 2010, the measure of discrepancy estimated by formula (15) was $\Delta \approx 0.07$, and for the experiment conducted on September 12,

http://dx.doi.org/10.5772/intechopen.71834

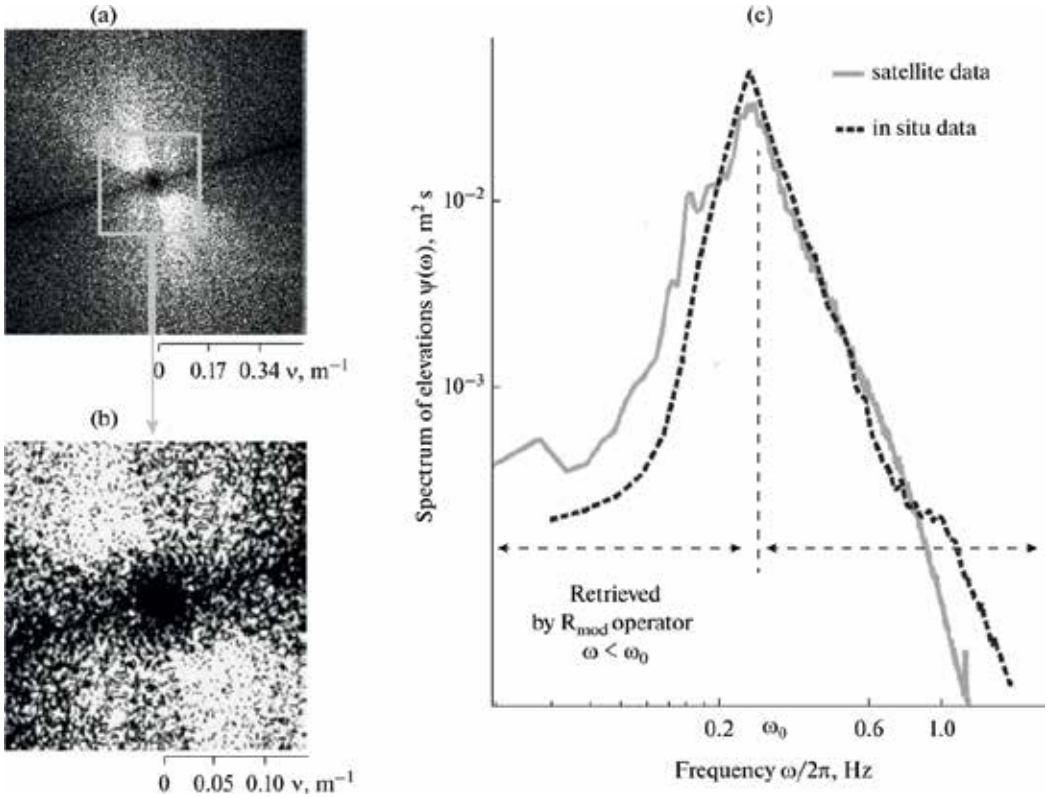

Figure 2. Comparison of the spectra of weak wind waves in the presence of swell waves measured from remote and contact experimental data. September 12, 2012: (a) and (b) two-dimensional slope spectrum recovered in two intervals of spatial frequencies; (c) comparison of the one-dimensional frequency spectrum of the elevations obtained from the two-dimensional spectrum of slopes by the retrieving operator R, with the spectrum obtained from the data of the string wave recorder.

2012, this measure of divergence amounted to $\Delta \approx 0.08$. The obtained results indicate the adequacy of the determination of wave spectra from satellite images of high spatial resolution.

During the experiments of the second type, a space survey was conducted in the vicinity of Oahu Island (Hawaii, USA) from the Ikonos and QuickBird satellites, which provided space images of high spatial resolution (0.65–1.0 m) and synchronous measurements of the frequency-angular wave spectra with the help of two wave buoys, drifting in the space survey area.

The experiments were carried out to assess the anthropogenic impacts on the water area of Mamala bay, using satellite and contact data [19]. In the course of complex experiments, space surveys and synchronous sea truth measurements were carried out, including with the help of drifting wave buoys, which ensure the registration of frequency-angle spectra of surface waves.

The following circumstance was taken into account when processing the data of the complex experiment. IKONOS and QuickBird satellites were photographed in these experiments far from the sunlight, and the resolution of the survey cameras of these satellites allowed us to fix surface waves of the submeter range (0.6–1.0 m). Under such conditions, the nonlinear components of

the brightness field of the sea surface make an insignificant contribution to the spectra of satellite images. In this connection, in the analysis of complex experiment data, it is permissible to use the linear model, according to which the two-dimensional spatial spectra of satellite images S (kx, ky) are linearly related to the spatial spectra of sea wave inclinations Ψ_{φ} (νx, νy).

The results of comparison of the wave spectra obtained on the basis of remote data and drifting buoy data are shown in **Figure 3**.

During the processing, fragments of satellite images with dimensions of 1024 × 1024 or 2048 × 2048 pixels were selected in such a way that the fragment overlapped the wave buoy path at

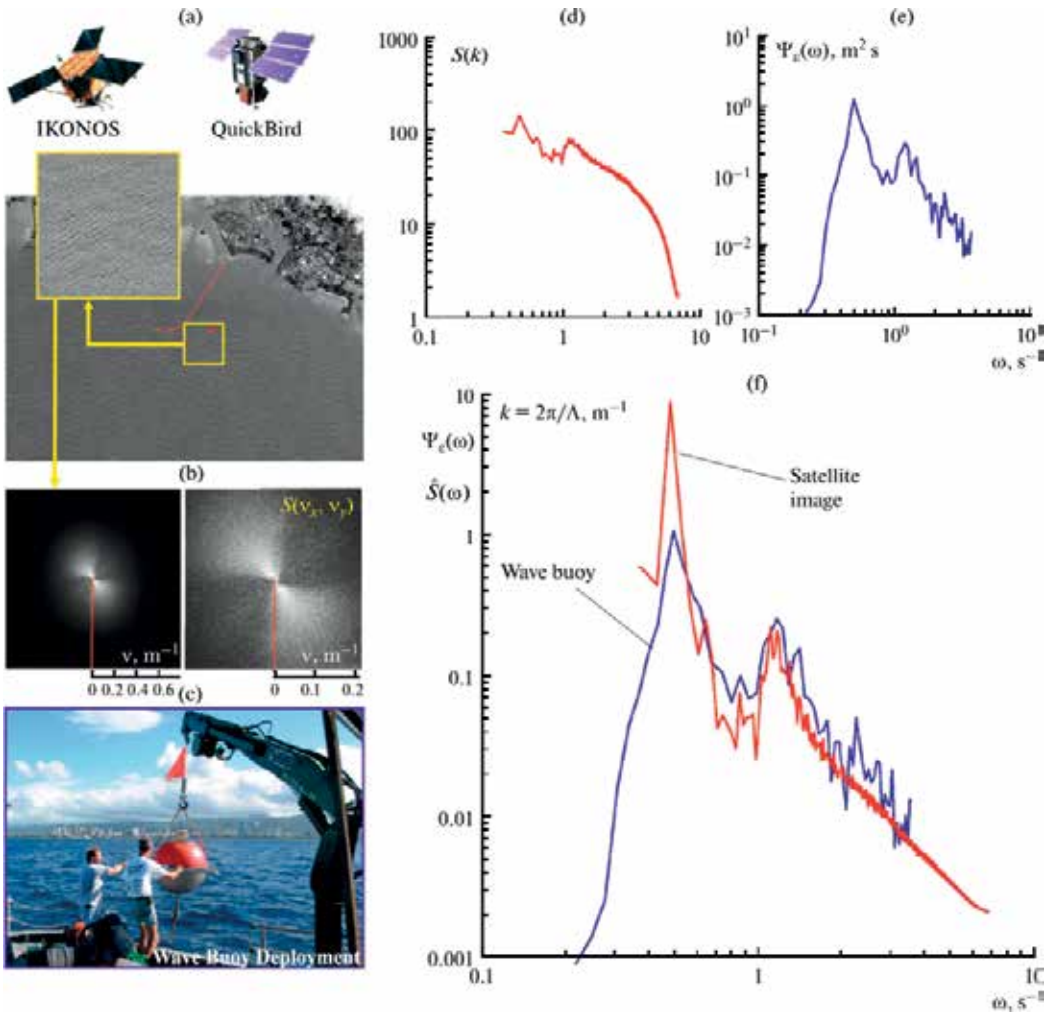

Figure 3. The results of a joint analysis of sea wave spectra obtained from space images and from drifting wave buoys: (a) the initial space image and its fragment used for processing; (b) two-dimensional spatial spectrum of the selected fragment and its enlarged central part (right); (c) installation of a wave buoy; (d) a one-dimensional spatial spectrum obtained from the two-dimensional spectrum of the satellite image; (e) the frequency spectrum obtained by a wave buoy; (f) comparison of frequency spectra obtained by different methods.

the time of shooting (see **Figure 3a**). The data obtained by measurements with a wave buoy (see **Figure 3c**) were selected in such a way that the moment of the survey was as close as possible to the end of the half-hour accumulation of data obtained by the buoy. For the selected image fragments, two-dimensional spatial spectra S (k_x, k_y) were formed, examples of which are shown in **Figure 3b**, and according to measurements by wave buoys, the frequency-angle spectra of the elevations $\Psi\varepsilon$ (ω, θ) are constructed.

Two-dimensional spectra of satellite images S (k_x, k_y) (see **Figure 3b**) also yielded one-dimensional spatial spectra S (**k**) (see **Figure 3d**), and from the frequency-angle spectra of the elevations Ψ (ω, θ) obtained by wave buoys, the frequency spectra of Ψ (ω) (see **Figure 3e**) were constructed in the chosen directions.

From the one-dimensional spatial spectra obtained from two-dimensional spectra of satellite images using the dispersion relation for gravitational waves, the frequency spectra S (ω) were determined from the formula (12).

An important stage in the comparison of wave spectra obtained from space images and data from wave buoys is the detection of additional spectral harmonics due to anthropogenic effects on the surface waves caused by buried wastewater outfalls in the region of the experiments [7–12]. Such spectral harmonics arise under the action of high-frequency internal waves generated by turbulent jets of nonsalty water discharged into the saline marine environment through the diffusers of deep outfalls. Similar effects are caused by various physical mechanisms, analyzed in [14, 15].

The conducted experiments' results and comparison of additional spectral harmonics detected on the base of satellite image spectra and wave buoy data have confirmed the efficiency of remote methods for detection of manifestations of anthropogenic impacts on the water environment taking into account wave spectra changes.

Experimental work of the third type was performed completely on the oceanographic platform in Katsiveli settlement (Crimea).

To verify the adequacy of the methods for retrieving sea wave spectra in the 0.1–1 m shortwave range, the results of complex field experiments of the third type were analyzed. These experiments were carried out at an oceanographic platform, including conventional and stereo survey, as well as contact measurements of wave spectra using a wave recorder array. Stereo surveying of the sea surface was carried out from the working platform, which was located at a height of 16 m above sea level with a 10.2 m basis using stereocameras with a focal length of 99 mm. From the measured elevation field samples, the spectra Ψ_ϕ (k_ϕ) were calculated using the interpolation and discrete Fourier transform procedures. Simultaneously, with the stereoscopic shooting on the platform, contact measurements of the frequency spectra of waves were performed using a wave spectrograph providing registration in the frequency range of 0.1–15 Hz with a tunable filter bandwidth of 0.1 Hz. In the wave spectrograph, a method for sequential analysis of the frequency spectrum was realized by automatically tuning the transmission frequency of a narrowband filter in a given interval [22].

Images of the sea surface obtained during stereo photography were also used to retrieve the wave spectra by a nonlinear multiposition method [22]. At the same time, fragments of two

stereopair images were analyzed on which a surface area processed by a stereo-photogrammetric method is presented. Experimental conditions: the zenith angle of the Sun was 30° (the images were recorded with a cloudless sky), and the wind speed was 5 m/s. During the experiments, the wind blew from the shore, so the acceleration of wind waves did not exceed the distance from the platform to the shore, which was ~600 m.

As the main characteristics for comparing the wave spectra obtained by different methods, the rms elevation σ_ξ and the power exponent p_x in two wavelength intervals Λ were chosen: from 0.1 to 1 m and from 0.04 to 0.4 m. The wave spectra, measured by different methods, were recalculated in spatial spectra of χ (k).

In the presence of solar glitters in the image, which cause a significant nonlinearity of the transfer function, which connects the slopes and the brightness of the elements of the sea surface, systematic errors arise in retrieving the spectra of waves. Such errors were eliminated by means of nonlinear retrieval filters adapted to the wave characteristics using an iterative procedure for retrieving the wave spectra [20, 25].

Quantitative estimates of these errors were given in [17, 21], where it was shown that even with the use of images containing solar patches, two iterations of retrieving obtained from different positions are sufficient to reduce the relative error in measuring the integral spectral energy to ≈3% and the error determines the exponent of the power-law approximation of the wave spectrum to ≈0.03.

To correct the spectra of elevations obtained by the stereo method, the noise of digitization resulting from errors in measuring the elevations of the surface during stereo-photogrammetric image processing was taken into account. It was assumed that the noise is additive, so their spectrum was subtracted from the spectra measured during processing [22].

The form of short-wave spatial spectra of sea surface elevations χ (k), obtained from data of different measurement methods, is shown in **Figure 4**. The spectra are constructed by averaging over six realizations. The analysis of **Figure 4** indicates a good correspondence of the wave spectra obtained by different methods in the short-wave range of wavelengths (Λ = 0.04–1.0 m). The character of the obtained spatial spectra of the elevations testifies to the possibility of their power-law approximation by the Toba formula [23], recalculated taking into account the dispersion relation (12).

To generalize the data obtained, such characteristics of the spectra as the exponents of power approximation and the dispersion of wave energy in different wavelength ranges were analyzed. For the wavelength range Λ = 1.0–5.0 m, wave spectra were used, which were determined from the space image obtained from the GEOEYE satellite by the nonlinear recovery approach. For shortwave waves (Λ = 0.04–1.0 m), experimental data obtained in six experiments of the third type by three methods in two bands were used: Λ = 0.04–0.4 m and Λ = 0.1–1.0 m.

For comparison with known literature data, the parameters of wave spectra were calculated from the well-known approximations: Phillips, Pierson-Moskovitz, Toba, Leikin, and Rosenberg [19]. The values of the variances and exponents of power approximations of the spatial spectra of sea surface elevations, obtained experimentally by various methods, as well as obtained from known approximations, were analyzed in [19].

http://dx.doi.org/10.5772/intechopen.71834

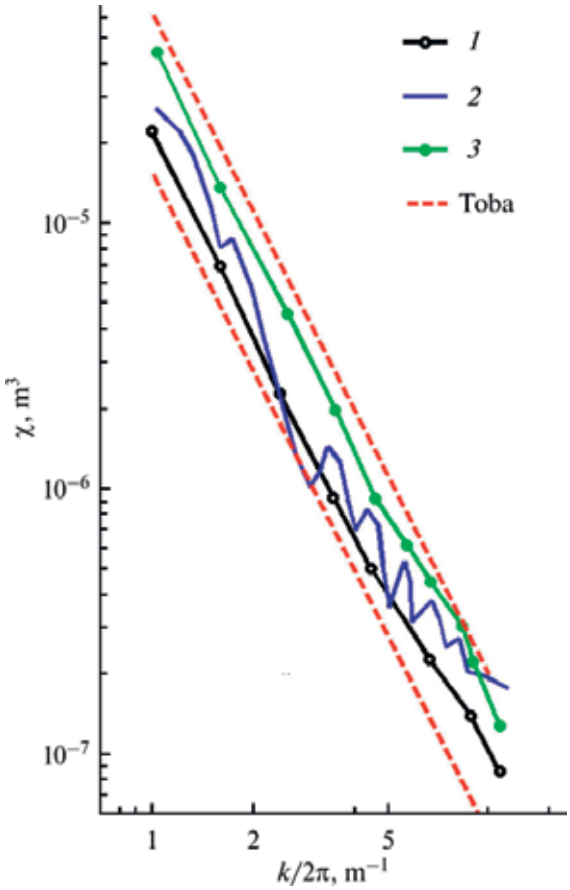

Figure 4. Spatial spectra of sea surface elevations, obtained by different methods: (1) retrieving of images by the nonlinear multiposition method; (2) contact measurements by a string wave; (3) stereo-photogrammetric measurements; red lines denote Toba approximation.

Analysis of the experimental data has shown that there is a coincidence of statistical estimates of the characteristics of sea waves measured by different methods within the mean square scatter of samples of these parameters. This indicates that the developed remote methods sufficiently accurately determine the characteristics of sea waves.

The most important for practice is the determination of the exponent p in power approximation. An analysis of the data obtained in the experiments shows that the parameters of the spectra of waves retrieved from the image spectra correspond best to the Toba approximation [23].

The obtained results of the studies by remote methods made it possible to reveal the following values of the parameters p for the experimental conditions:

p = 2.22 ± 0.08 for the wavelength interval Λ = 1.0–5.0 m; p = 2.23 ± 0.09 for the short-wavelength wavelength interval Λ = 0.1–1.0 m; p = 2.1 ± 0.08 for the short-wavelength wavelength interval Λ = 0.04–0.4 m.

To determine the effect of sea surface disturbances associated with the nonstationary nature of the wave, correlation analysis was used to obtain the estimates. Correlation coefficients between sea surface characteristics in the short-wave range were studied in [19].

The correlation of the estimates carried out by various methods is quite high, and averages were 0.8–0.9. Those cases in which there is a decrease in the correlation coefficient are explained by the peculiarities of the measurement methods. For example, a slight decrease in the correlation coefficient of estimates of the exponent px obtained by the contact method, with estimates obtained from the images, is due to the time diversity of the registration of the spectral density at different frequencies ω. During the tuning of the filter transmission frequency, a change in the spectral density of the wave at different frequencies ω can occur, which leads to a deviation in the estimate of the exponent of the elevation spectrum with respect to estimates obtained for a fixed time in image processing [22].

Good correlation between independently measured wave spectra allows us to conclude that the developed remote measurement methods reliably reflect real processes in the ocean-atmosphere boundary layer.

Retrieving operators constructed by the numerical method and having passed the calibration procedure using contact data were used for experimental studies in various water areas [16, 18–20].

One of the important experiments was to study the development of wind waves at various distances from the shore. An experiment of this type was conducted in the water area of Mamala Bay near the Oahu Island (Hawaii, USA) [19].

Figure 5 shows four fragments of the space image obtained by the QuickBird satellite with 0.65 m spatial resolution, and the spectra of slopes retrieved on their base.

An analysis of the two-dimensional retrieved slope spectra shows that, as the distance from the coast and the wind regime change, characteristic additional wave systems develop. At the same time, the energy of sea waves increases with the distance from the coast and the increase in wind speed.

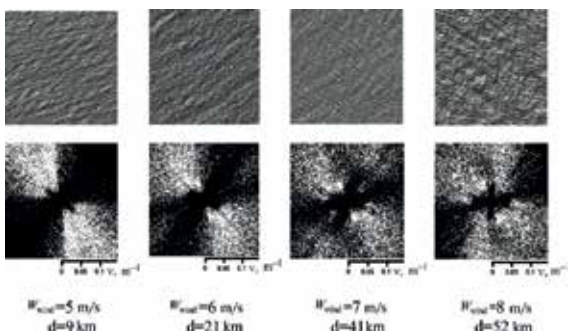

Figure 5. Fragments of the satellite image obtained at various distances from the shore in the water area of Mamala Bay off the Oahu Island and retrieved two-dimensional spatial spectra of sea wave slopes.

http://dx.doi.org/10.5772/intechopen.71834

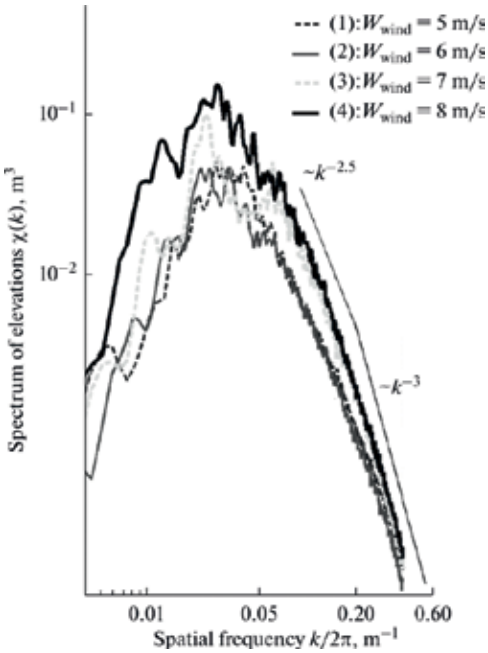

Figure 6. One-dimensional spatial spectra of sea wave elevation, retrieved from fragments of the satellite image, obtained at different distances from the shore at different wind speeds in the water area of Mamala Bay near Oahu (Hawaii, USA).

Figure 6 presents one-dimensional spatial elevation spectra obtained by averaging over the direction of two-dimensional spatial spectra of elevations in the 70° angular sector, recovered using the developed retrieving operator.

The analysis of **Figure 6** shows that the course of one-dimensional spectra retrieved from the two-dimensional spatial spectra of fragments of the satellite image depends on wind speed and the distance of the corresponding sections from the shore. The shape and position of the spectral maxima depends not only on the speed of the near-surface wind but also on the acceleration from the leeward shore, which in this experiment was between 10 and 50 km.

5. Conclusion

A method is developed to retrieve the spectra of gradients and elevations of sea waves from the spectra of aerospace optical images over a wide frequency range, based on the formation of a retrieving operator that takes into account the nonlinear character of the modulation of the brightness field by sea surface slopes.

The conducted studies demonstrated the effectiveness and adequacy of the application of the method of recovering the spectra of gradients and elevations of sea waves from satellite optical images of high spatial resolution.

The optimal parameters of such a retrieving operator are determined by an iterative method when comparing the spectra of aerospace images with spectra with sea wave characteristics measured with high accuracy by string waveforms under controlled conditions.

During the research, the spatial spectral characteristics of sea waves estimated from remote sensing data were compared with the corresponding characteristics measured by contact means under controlled conditions. The satellite data used for the comparison were the arrays of string wave recorders mounted on a stationary oceanographic platform, the data of a stereo survey performed with a high spatial resolution from a low altitude above the sea surface, as well as data of drifting wave buoys. Comparison of the spectra of waves and their statistical characteristics demonstrated the consistency of the results obtained in the processing of satellite images of high spatial resolution and the results of processing data obtained by various sea truth assets.

Experiments carried out in different water areas demonstrated the possibility of using a retrieving operator with optimal values of parameters found under certain conditions for obtaining satellite optical images of the sea surface for a wide range of wave formation conditions.

As a result of the application of numerical optimization procedures, the values of the parameters of nonlinear retrieving filters that are effective in both developed and developing waves, as well as in the presence of swell waves, are chosen. In this case, the measurement of the divergence of the wave spectra obtained from satellite images of high spatial resolution and subsatellite data at optimal values of these parameters is 0.08–0.12. This testifies to the adequacy of the proposed method for recording wave spectra from the spectra of satellite images over a wide frequency range.

Thus, the adequacy of remote measurement of both the time-averaged spectra of the sea surface and the variations of these spectra caused by wave nonstationarity using high spatial resolution images and nonlinear recovering operators has been experimentally confirmed. The conducted researches made it possible to develop methods and technologies for comprehensive ground-space monitoring of marine areas to obtain such important oceanographic characteristics as surface wave spectra.

The developed method can be used to study surface wave conditions, including in the space monitoring of natural and anthropogenic impacts on the marine waters.

Acknowledgements

The work was carried out with the financial support of the state represented by the Ministry of Education and Science of the Russian Federation in the framework of the Federal Program "Research and development in priority areas of development of the scientific and technological complex of Russia for 2014-2020" (unique identifier of the project RFMEFI57716 X0234).

Author details

Valery G. Bondur* and Alexander B. Murynin*

*Address all correspondence to: vgbondur@aerocosmos.info and amurynin@bk.ru

AEROCOSMOS Research Institute for Aerospace Monitoring, Moscow, Russia

References

[1] Monin AS, Krasitsky VP. Ocean Surface Phenomena. Leningrad: Gidrometeoizdat; 1985. 375 p

[2] Phillips OM. Dynamics of the Upper Ocean Layer. Cambridge: Cambridge University Press; 1977. 336 p

[3] Davidan IN, Lopatukhin LI, Rozhkov VA. Wind Waves in the World Ocean. Leningrad: Gidrometeoizdat; 1985. 289 p

[4] Bondur VG. Aerospace methods in modern oceanology. In: New Ideas in Oceanology, Physics, Chemistry, and Biology. Vol. 1. Moscow: Nauka; 2004. pp. 55-117

[5] Bondur VG, Grebenyuk YV. Remote indication of anthropogenic influence on marine environment caused by depth wastewater plume: Modeling, experiments. Issledovaniya Zemli iz Kosmosa. 2001;**6**:46-67

[6] Keeler R, Bondur V, Gibson C. Optical satellite imagery detection of internal wave effects from a submerged turbulent outfall in the stratified ocean. Geophysical Research Letters. 2005;**32**:L12610. DOI: 10.1029/2005GL022390

[7] Bondur VG, Zhurbas VM, Grebenyuk YV. Mathematical modeling of turbulent jets of deepwater sewage discharge into coastal basins. Oceanology. 2006;**46**(6):757-771

[8] Bondur VG, Sabinin KD, Grebenyuk YV. Anomalous variation of the Ocean's Inertial Oscillations at the Hawaii Shelf. Doklady Earth Sciences. 2013;**450**:526-530

[9] Bondur VG, Grebenyuk YV, Sabinin KD. Variability of internal tides in the coastal water area of Oahu Island (Hawaii). Oceanology. 2008;**48**(5):611-621

[10] Bondur VG, Grebenyuk YV, Ezhova EV, Kazakov VI, Sergeev DA, Soustova IA, Troitskaya YI. Surface manifestations of internal waves investigated by a subsurface buoyant jet: 1. The mechanism of internal-wave generation. Izvestiya, Atmospheric and Oceanic Physics. 2009; **45**(6):779-790

[11] Bondur VG, Grebenyuk YV, Ezhova EV, Kazakov VI, Sergeev DA, Soustova IA, Troitskaya YI. Surface manifestations of internal waves investigated by a subsurface buoyant jet: 3. Surface manifestations of internal waves. Izvestiya, Atmospheric and Oceanic Physics. 2010; **46**(4):482-491

[12] Bondur VG, Grebenyuk YV, Sabinin KD. The spectral characteristics and kinematics of shortperiod internal waves on the Hawaiian shelf. Izvestiya, Atmospheric and Oceanic Physics. 2009;**45**(5):598-607

[13] Bondur VG. Modern approaches to processing large hyperspectral and multispectral aerospace data flows. Izvestiya, Atmospheric and Oceanic Physics. 2014;**50**(9):840-852

[14] Bondur VG. Satellite monitoring and mathematical modelling of deep runoff turbulent jets in coastal water areas. In: Waste Water—Evaluation and Management. Croatia: InTech; 2011. pp. 155-180

[15] Bondur VG, Zubkov EV. Showing up the small-scale ocean upper layer optical inhomogeneities by the multispectral space images with the high surface resolution. Part 1. The canals and channels drainage effects at the coastal zone. Issledovaniya Zemli iz Kosmosa. 2005;(4):54-61

[16] Bondur VG, Murynin AB. Reconstruction of the spectra of the surface waves from the spectra of their images with an account of the nonlinear modulation of the brightness field. Optika Atmosfery i Okeana. 1991;**4**(4):387-393

[17] Murynin AB. Restoration of the spatial spectrum of the sea surface from the optical images in a nonlinear model of brightness field. Issledovaniya Zemli iz Kosmosa. 1990;**6**:60-70

[18] Bondur VG, Murynin AB. Methods for retrieval of sea wave spectra from aerospace image spectra. Izvestiya, Atmospheric and Oceanic Physics. 2016;**52**(9):877-887

[19] Bondur VG, Dulov VA, Murynin AB, Yurovsky YY. Studying marine wave spectra in a wide range of wavelengths using satellite and in situ data. Izvestiya, Atmospheric and Oceanic Physics. 2016;**52**(9):888-903

[20] Bondur VG, Dulov VA, Murynin AB, Ignatiev VY. Retrieving sea-wave spectra using satellite-imagery spectra in a wide range of frequencies. Izvestiya, Atmospheric and Oceanic Physics. 2016;**52**(9):637-648

[21] Murynin AB. Parametrization of filters retrieving spatial spectra of sea surface slopes from optical images. Issledovaniya Zemli iz Kosmosa. 1991;**5**:31-38

[22] Baranovskii VD, Bondur VG, Kulakov VV, et al. Calibration of remote measurements of 2-D spatial wave spectra from optical images. Issledovaniya Zemli iz Kosmosa. 1992;**2**:59-67

[23] Toba J. Local balance in the air-sea boundary process. Journal of the Oceanographical Society of Japan. 1973;**29**:209-225

[24] Yurovskaya MV, Dulov VA, Chapron B, Kudryavtsev VN. Directional short wind wave spectra derived from the sea surface photography. Journal of Geophysical Research. 2013;**118**(9):4380-4394. DOI: 10.1002/jgrc.20296

[25] Bondur VG, Murynin AB, Ignatiev VY. Parameters optimization in the problem of sea-wave spectra recovery by airspace images. Journal of Machine Learning and Data Analysis. 2016;**2**(2):218-230. DOI: 10.21469/22233792.2.2.07

Chapter 5

Electromagnetic Polarization: A New Approach on the Linear Component Method

Jobson de Araújo Nascimento,
Regina Maria De Lima Neta,
José Moraes Gurgel Neto, Adi Neves Rocha and
Alexsandro Aleixo Pereira Da Silva

Additional information is available at the end of the chapter

http://dx.doi.org/10.5772/intechopen.71836

Abstract

In this chapter it is elucidated how the analytical solution was obtained to obtain the electromagnetic polarization profile of a completely polarized wave in the region of distant fields. The analytical solution was obtained from the interpretation of the physical phenomenon associated with the method of the linear component, which was adapted for the use of discrete and miniaturized elements, reducing the physical space for the measurement circuit and the expenses associated to the delay circuit. From the analytical solution it is possible to observe that with only one phase measurement in the delay circuit it is possible to obtain the polarization profile of the wave, with the axial ratio and phase, respectively.

Keywords: polarization, phased shifter, microfite, dipole

1. Introduction

Nowadays, in many industries, industries, offices, companies, supermarket chains among others, there is a very large diversity of radio frequency (RF) equipment. In these sectors, several RF equipment can coexist, operating simultaneously in a small space, even having different emission/reception characteristics. Because there are several devices, some of them may have their performances harmed or even compromised due to electromagnetic interference (EM) caused by other equipment that may be emitting an undesirable EM wave to the apparatus that is undergoing the interference process. In addition, it is also observed that, in the technological market of the present day, the size of the antennas existing in these

equipments becomes less and less. The miniaturization of antennas in many cases makes it difficult to locate the emitter system, which is possibly causing EM interference, since the antenna is often built into the equipment. Therefore, knowledge of the direction of propagation of the EM wave emitted by these antennas or EM field emitting elements will facilitate the discovery of the EM interference source (s) and the determination of possible engineering actions that help to attenuate the same. The study of techniques that aim to reduce the damage caused by EM interference between electronic devices has increased in recent years. Through a study of the polarization of electromagnetic waves, one can identify the behavior of the irradiated electric field. The knowledge of the amplitude and phase of the electric field [1] allows to identify the polarization pattern of the wave The information of the phase of the electric field in the region of far fields (FFR) is of great value for the discovery and suggestions of overcoming problems caused By EM interference. An experimental technique was developed to confirm the linear component method, proposed by Kraus [2], for the reconstruction of the electromagnetic polarization in the FFR. The method was adapted using miniaturized discrete elements for the lagging circuit and an experimental and analytical confirmation was obtained in order to obtain the phase of the electric field radiated to electromagnetic waves that are completely polarized in the FFR using discrete components.

2. Methodology

The model for obtaining the polarization profile of an electromagnetic (EM) wave in the RCD was initially proposed by [2]. An adaptation in the phase-shift circuit to obtain the phase of polarization is proposed in an analytical way below.

The mathematical approach to gain access to the polarization phase of the EM wave in the FFR (Far Field Region) is made using the phasor analysis of the signal that is received by each dipole, and the resulting signal at the receiver of **Figure 1(b)**. The discrepancy introduced by the discrete components does not identify the phase of the transmitted signal, and it allows to deduce this phase after a phasor sum of the two components. What would be simpler is the construction of a system to identify the phase of the emitted electric field.

In the delay circuit **Figure 1(b)** it was proposed a modification in the physical structure of the phase shift, replacing the split line with planar transmission lines at the end of the connection with the dipoles. And in a discrete way the delay was supposed from the interpretation of the associated physical phenomenon and the supposed theoretical formulation. The proposed delay circuit can be observed in **Figure (2)**.

The particular cases were tested in order to validate the method. But for the general case, where the polarization phase of the signal emitted by the transmitting antenna is not known, the following reasoning is given. From the consideration that the fields captured by the dipoles are of the form

$$\vec{E_v} = E_v.e^{j0^\circ}\hat{v} \tag{1}$$

$$\vec{E_h} = E_h.e^{j(\psi+\theta)}\hat{h} \tag{2}$$

http://dx.doi.org/10.5772/intechopen.71836

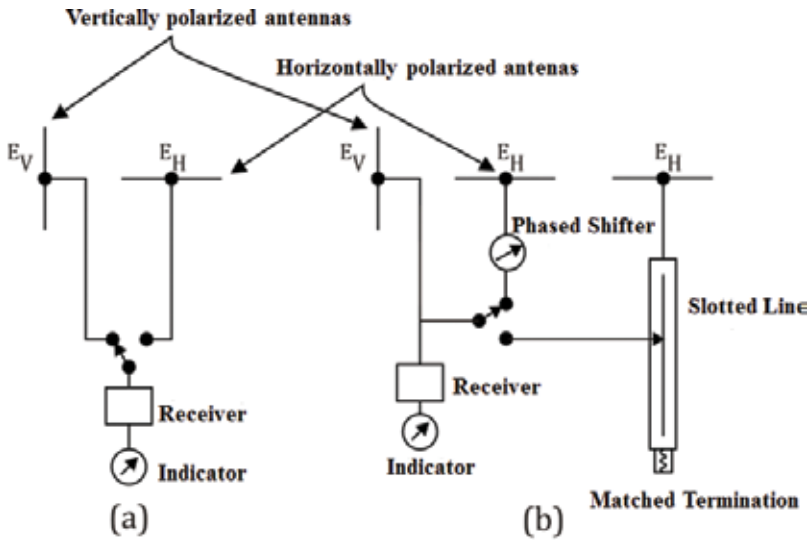

Figure 1. Set up for measuring: (a) the axial ratio; (b) the phase difference ψ, using the method of linear components [1].

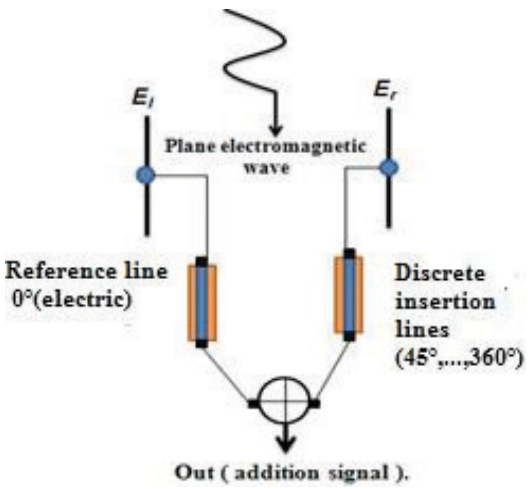

Figure 2. Circuit validation of adjustments made in the method of the linear component.

Where ψ is the phase difference between the two signals picked up by the dipoles, i.e., the phase of the polarization of the transmitted signal, and θ is the delay intentionally inserted in order to find the phase of the emitted signal, and $\hat{v}$ and $\hat{h}$ are the unit vectors in the vertical and horizontal directions, respectively. The receiver is the one who performs a phasor sum of the signals at high frequencies, has its resulting field given by

$$\vec{E_R} = \vec{E_v} + \vec{E_h} \tag{3}$$

In phasor form one has to

$$E_R = E_v e^{j0^\circ} + E_h e^{j(\psi+\theta)} \tag{4}$$

In developing this expression one has to

$$\begin{gathered} E_R = E_v \cos\left(0^\circ\right) + E_h \cos\left(\theta + \psi\right) + jE_h[sen(\theta + \psi)] \\ E_R = E_v + E_h[\cos\left(\theta\right).\cos\left(\psi\right) - sen(\theta).sen(\psi)] + jE_h[sen(\theta).\cos\left(\psi\right) + sen(\psi).\cos\left(\theta\right)] \end{gathered} \tag{5}$$

Once E_R, E_h, E_v e ψ are known it can be adopted that

$$\begin{cases} A = E_h.\cos\left(\theta\right) \\ B = E_h.sen(\theta) \\ C = E_R \end{cases} \tag{6}$$

Is that $z = a + bi$;

$$a = E_v + A.\cos\left(\psi\right) - Bsen(\psi) \tag{7}$$

$$b = Acos(\psi) + Bsen(\psi) \tag{8}$$

$$C = E_v + A.\cos\left(\psi\right) - Bsen(\psi) + j[Asen(\psi) + Bcos(\psi)]. \tag{9}$$

The value of C in this equation is the electric field module E_R and this module is given by

$$|z| = \sqrt{a^2 + b^2} \tag{10}$$

Thus it is to develop the expression (9) in (10) that:

$$\begin{gathered} |C| = \sqrt{[E_v + A.\cos\left(\psi\right) - Bsen(\psi)]^2 + [Asen(\psi) + Bcos(\psi)]^2} \\ C^2 = E_v^2 + A^2 + B^2 + 2.E_v[A.\cos\left(\psi\right) - B.sen(\psi)] \end{gathered} \tag{11}$$

In the case where the angle ψ it is unknown to have:

$$\begin{gathered} C^2 - E_v^2 - A^2 - B^2 = 2.E_v[A.\cos\left(\psi\right) - B.sen(\psi)] \\ \frac{C^2 - E_v^2 - A^2 - B^2}{2.E_v} = A.\cos\left(\psi\right) - B.sen(\psi) \end{gathered} \tag{12}$$

Doing

$$D = \frac{\left(C^2 - E_v^2 - A^2 - B^2\right)}{2E_v} \tag{13}$$

it has been

$$D = A.\cos\left(\psi\right) - B.sen(\psi) \tag{14}$$

Using the expression

$$\cos(\psi) = \pm\sqrt{1 - sen^2(\psi)} \tag{15}$$

In (14) one has to

$$D = A.\sqrt{1 - sen^2(\psi)} - B.sen(\psi). \tag{16}$$

The geometric development of the analytic model is elucidated in the following expressions.

From the geometric analysis to Eq. (16) illustrated in the **Figure 3** is possible to verify that:

$$\alpha = \psi + atan\left(\frac{B}{A}\right) \tag{17}$$

$$\overline{OP}' = \overline{OP}.\cos(\alpha) \tag{18}$$

$$\overline{OP}' = D \tag{19}$$

$$D = \sqrt{A^2 + B^2}\cos\left(\psi + atan\left(\frac{B}{A}\right)\right) \tag{20}$$

$$\frac{D}{\sqrt{A^2 + B^2}} = \cos\left(\psi + atan\left(\frac{B}{A}\right)\right) \tag{21}$$

$$\psi = acos\left(\frac{D}{\sqrt{A^2 + B^2}}\right) - atan\left(\frac{B}{A}\right) \tag{22}$$

Then it found a closed expression to find the value of phase difference ψ. The discovery phase can be analytically or by using the parameters measured experimentally as done at work.

Denoting $x = sen(\psi)$, one can write Eq. (16) as

$$D = A.\sqrt{1 - x^2} - B.x. \tag{23}$$

In developing Eq. (23), one arrives at the expression that relates the unknown angle ψ, with known constants. In solving Eq. (23) have

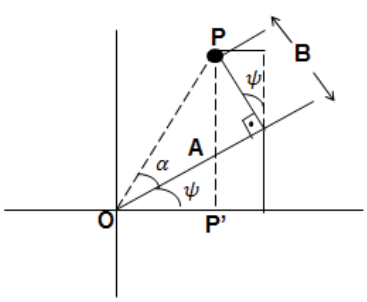

Figure 3. This is achieved as the phase of the polarization.

$$sen(\psi) = \frac{-D \pm \left[(DB)^2 - \left(A^2 + B^2\right).\left(D^2 - A^2\right)\right]^{1/2}}{\left(A^2 + B^2\right)} \tag{24}$$

An analysis was performed to validate Eq. (11) for elementary cases. The results can be seen in **Table 1** and all the mathematical development that follows.

$$\psi = arcsen\left(\frac{-D \pm \left[(DB)^2 - \left(A^2 + B^2\right).\left(D^2 - A^2\right)\right]^{1/2}}{\left(A^2 + B^2\right)}\right) \tag{25}$$

To validate the cases where there is ambiguity in the polarization profile of the EM wave, which are those in which the axial ratio is unitary, Eq. (9) and tested a random phase in the delay circuit, in order to prove that it is enough to only insert a delay line to validate the adapted linear component method [3].

The elementary cases were tested in Eq. (9), the whole mathematical development for these cases is next

- For the Linear case at 45°, it is possible to write:

$$\begin{cases} E_h = 1\text{(horizontal dipole amplitude)} \\ E_v = 1\text{(vertical dipole amplitude)} \\ \psi = 45^{\circ}\text{(phase difference)} \\ \theta = 45^{\circ}\text{ (generic phase of the line)} \end{cases}$$

Substituting this data into Eq. (9) we have that:

$$\begin{gathered} E_R = 1,0 + 1,0.\left[\cos\left(45^{\circ} + 45^{\circ}\right)\right] + j.1,0.\left[sen\left(45^{\circ} + 45^{\circ}\right)\right] \\ E_R = 1 + j \\ |E_R| = \sqrt{2} \end{gathered} \tag{26}$$

- For the linear case at 135°, we have that:

$$\begin{cases} E_h = 1\text{(horizontal dipole amplitude)} \\ E_v = 1\text{(vertical dipole amplitude)} \\ \psi = 135^{\circ}\text{(phase difference)} \\ \theta = 45^{\circ}\text{ (generic phase of the line)} \end{cases}$$

Substituting this data into Eq. (C.4.3) gives:

$$\begin{gathered} E_R = 1,0 + 1,0.\left[\cos\left(135^{\circ} + 45^{\circ}\right)\right] + j.1,0.\left[sen\left(135^{\circ} + 45^{\circ}\right)\right] \\ E_R = 0 \\ |E_R| = 0 \end{gathered} \tag{27}$$

Polarization profile	E_h	E_v	θ	$\lvert E_R \rvert$	ψ
Linear to 45°	100	100	45°	$\sqrt{2}$	45°
Linear to 135°	100	100	45°	0	135°
Left circular	100	100	45°	$\sqrt{2-\sqrt{2}}$	90°
Right circular	100	100	45°	$\sqrt{2+\sqrt{2}}$	270°

Table 1. Polarization patterns tested.

- For the left circular case, we have:

$$\begin{cases} E_h = 1(\text{horizontal dipole amplitude}) \\ E_v = 1(\text{vertical dipole amplitude}) \\ \psi = 90^{\circ}(\text{phase difference}) \\ \theta = 45^{\circ}\ (\text{generic phase of the line}) \end{cases}$$

Substituting this data into Eq. (C.4.3) gives:

$$\begin{gathered} E_R = 1,0 + 1,0.\left[\cos\left(90^{\circ} + 45^{\circ}\right)\right] + j.1,0.\left[sen\left(90^{\circ} + 45^{\circ}\right)\right] \\ E_R = 1 - \frac{\sqrt{2}}{2} + j.\left(\frac{\sqrt{2}}{2}\right) \\ |E_R| = \sqrt{2-\sqrt{2}} \end{gathered} \tag{28}$$

- For the Circular case on the right, we have that:

$$\begin{cases} E_h = 1(\text{horizontal dipole amplitude}) \\ E_v = 1(\text{vertical dipole amplitude}) \\ \psi = 270^{\circ}(\text{phase difference}) \\ \theta = 45^{\circ}\ (\text{generic phase of the line}) \end{cases}$$

Substituting this data into Eq. (C.4.3) gives:

$$\begin{gathered} E_R = 1,0 + 1,0.\left[\cos\left(270^{\circ} + 45^{\circ}\right)\right] + j.1,0.\left[sen\left(270^{\circ} + 45^{\circ}\right)\right] \\ E_R = 1 + \frac{\sqrt{2}}{2} + j.\left(-\frac{\sqrt{2}}{2}\right) \\ |E_R| = \sqrt{2+\sqrt{2}} \end{gathered} \tag{29}$$

Therefore what will be done is a comparison of the values of θ, with the possible results of E_R, and we have:

- Linear at 45°:
- $E_h = 1$;
- $E_v = 1$;
- $\psi = 45^{\circ}$;
- $|E_R| = \sqrt{2}$;
- ψ =?

When applying in (9) we have:

$$\sqrt{2}^2 = 1 + \left(\frac{\sqrt{2}}{2}\right)^2 + \left(\frac{\sqrt{2}}{2}\right)^2 + \cos(2\psi)\left[\left(\frac{\sqrt{2}}{2}\right)^2 - \left(\frac{\sqrt{2}}{2}\right)^2\right] + 2.1.\left[\frac{\sqrt{2}}{2}.\cos(\psi) - \frac{\sqrt{2}}{2}sen(\psi)\right]$$

$$2 = 2 + 2.\frac{\sqrt{2}}{2}[\cos(\psi) - sen(\psi)]$$

$$sen\left(\frac{\pi}{2} - \psi\right) = sen(\psi),$$

$$\frac{\pi}{2} - \psi = \psi + 2.k.\pi$$

$$\psi = \frac{\pi}{4} + 2.k.\pi. \tag{30}$$

Which certifies the phase difference of 45°.

- Linear at 135°:
- $E_h = 1$;
- $E_v = 1$;
- $\psi = 45^{\circ}$;
- $|E_R| = 0$;
- ψ=?

When replacing in (9) we have:

$$0 = 1 + \left(\frac{\sqrt{2}}{2}\right)^2 + \left(\frac{\sqrt{2}}{2}\right)^2 + \cos(2\psi)\left[\left(\frac{\sqrt{2}}{2}\right)^2 - \left(\frac{\sqrt{2}}{2}\right)^2\right] + 2.1.\left[\frac{\sqrt{2}}{2}.\cos(\psi) - \frac{\sqrt{2}}{2}sen(\psi)\right],$$

$$-2 = 2.\frac{\sqrt{2}}{2}[\cos(\psi) - sen(\psi)],$$

$$sen\left(\psi - \frac{\pi}{4}\right) = sen\left(\frac{\pi}{2}\right) + 2.k.\pi,$$

$$\psi = \frac{3.\pi}{4} + 2.k.\pi. \tag{31}$$

- Which validates the phase difference of 135°.
- Circular left
- $E_h = 1$;
- $E_v = 1$;
- $\psi = 45^{\circ}$;
- $|E_R| = \sqrt{2 - \sqrt{2}}$;
- ψ =?

When applying in (9), we have that:

$$\left(\sqrt{2-\sqrt{2}}\right)^2 = 1 + \left(\frac{\sqrt{2}}{2}\right)^2 + \left(\frac{\sqrt{2}}{2}\right)^2 + \cos(2\psi)\left[\left(\frac{\sqrt{2}}{2}\right)^2 - \left(\frac{\sqrt{2}}{2}\right)^2\right] + 2.1.\left[\frac{\sqrt{2}}{2}.\cos(\psi) - \frac{\sqrt{2}}{2}sen(\psi)\right]$$

$$2 - \sqrt{2} = 2 + \ 2.\frac{\sqrt{2}}{2}[\cos(\psi) - sen(\psi)],$$

$$sen\left(\psi - \frac{\pi}{4}\right) = sen\left(\frac{\pi}{4}\right) + 2.k.\pi,$$

$$\psi = \frac{\pi}{2} + 2.k.\pi. \tag{32}$$

Which gives the phase difference of 90°.

- Circular right:
- $E_h = 1$;
- $E_v = 1$;
- $\psi = 45^{\circ}$;
- $|E_R| = \sqrt{2 + \sqrt{2}}$;
- ψ =?

When replacing in (9), we have that:

$$\left(\sqrt{2+\sqrt{2}}\right)^2 = 1 + \left(\frac{\sqrt{2}}{2}\right)^2 + \left(\frac{\sqrt{2}}{2}\right)^2 + \cos(2\psi)\left[\left(\frac{\sqrt{2}}{2}\right)^2 - \left(\frac{\sqrt{2}}{2}\right)^2\right] + 2.1.\left[\frac{\sqrt{2}}{2}.\cos(\psi) - \frac{\sqrt{2}}{2}sen(\psi)\right]$$

$$2 + \sqrt{2} = 2 + \ 2.\frac{\sqrt{2}}{2}[\cos(\psi) - sen(\psi)],$$

$$sen\left(\psi - \frac{\pi}{4}\right) = sen\left(\frac{5.\pi}{4}\right) + 2.k.\pi,$$

$$\psi = \frac{3.\pi}{2} + 2.k.\pi. \tag{33}$$

Which certifies the phase difference of 270°.

Author details

Jobson de Araújo Nascimento[1]*, Regina Maria De Lima Neta[2], José Moraes Gurgel Neto[3], Adi Neves Rocha[3] and Alexsandro Aleixo Pereira Da Silva[4]

*Address all correspondence to: job.nascimento@gmail.com

1 Universidade Estadual de Ciências da Saúde de Alagoas (UNCISAL), Trapiche da Barra, Maceió-Alagoas, Brazil

2 IFPE-Rua Edson Barbosa de Araújo, Afogados da Ingazeira, PE, Brazil

3 Centro de Estudos Superiores de Maceió Cesmac, Maceió-Alagoas, Brazil

4 Universidade Federal de Pernambuco (UFPE), Recife, PE, Brazil

References

[1] Peter K, Yuri M. Measurement of Polarization and Applications. LFNM 2002, 3–5 June, 2002, Kharkiv, Ukraine. pp. 188-196

[2] Kraus JD. Antennas, 1 ed. McGraw–Hill book Company; 1950

[3] Nascimento JA, Assis FM, Serres A. Determination of the electromagnetic wave polarization from unknown sources by the method of linear component modified. In: Internacional Microwave and Optoelectronics Conference, 2013, Rio de Janeiro. Determination of the electromagnetic wave polarization from unknown sources by the method of linear component modified; 2013. pp. 1-6

Chapter 6

Modal Phenomena of Surface and Bulk Polaritons in Magnetic-Semiconductor Superlattices

Vladimir R. Tuz, Illia V. Fedorin and
Volodymyr I. Fesenko

Additional information is available at the end of the chapter

http://dx.doi.org/10.5772/intechopen.71837

Abstract

We discuss peculiarities of bulk and surface polaritons propagating in a composite magnetic-semiconductor superlattice influenced by an external static magnetic field. Three particular configurations of magnetization, namely, the Voigt, polar, and Faraday geometries, are considered. In the long-wavelength limit, involving the effective medium theory, the proposed superlattice is described as an anisotropic uniform medium defined by the tensors of effective permittivity and effective permeability. The study is carried out in the frequency band where the characteristic resonant frequencies of underlying constitutive magnetic and semiconductor materials of the superlattice are different but closely spaced. The effects of mode crossing and anti-crossing in dispersion characteristics of both bulk and surface polaritons are revealed and explained with an assistance of the concept of Morse critical points from the catastrophe theory.

Keywords: electromagnetic theory, polaritons, magneto-optical materials, superlattices, metamaterials

1. Introduction

Surface polaritons are a special type of electromagnetic waves propagating along the interface of two partnering materials whose material functions (e.g., permittivities) have opposite signs that are typical for a metal-dielectric boundary [1]. These waves are strongly localized at the interface and penetrate into the surrounding space over a distance of wavelength order in a medium, and their amplitudes fall exponentially away from the surface. Observed strong confinement of electromagnetic field in small volumes beyond the diffraction limit leads to enormous increasing matter-field interaction, and it makes attractive using surface waves in the wide fields from the microwave and photonic devices to solar cells [2, 3]. Furthermore, surface electromagnetic waves are highly promising from physical point of view because from

the character of their propagation, one can derive information about both interface quality and electromagnetic properties of partnering materials (such as permittivity and permeability). High sensitivity to the electromagnetic properties of media enables utilization of surface waves in the sensing applications, particularly in both chemical and biological systems [4]. Thus, studying characteristics of surface waves is essential in the physics of surfaces and optics; in the latter case, the research has led to the emergence of a new science—plasmonics.

Today plasmonics is a rapidly developing field characterized by enormous variety of possible practical applications. In many of them, an ability to control and guide surface waves is a crucial characteristic. Thereby in last decades, many efforts have been made to realize active tunable components for plasmonic integrated circuits such as switchers, active couplers, modulators, etc. In this regard, searching effective ways to control characteristics of plasmon-polariton propagation by utilizing external driving agents is a very important task. In particular, the nonlinear, thermo-optical, and electro-optical effects are proposed to be used in the tunable plasmonic devices for the control of plasmon-polariton propagation [5–8]. In such devices, the tuning mechanism is conditioned by changing the permittivity of the dielectric medium due to applying external electric field or temperature control. At the same time, utilization of an external magnetic field as a driving agent to gain a control over polariton dispersion features is very promising, since it allows changing both permeability of magnetic materials (e.g., ferrites) and permittivity of conducting materials (e.g., metals or semiconductors). It is worth mentioning that the uniqueness of this controlling mechanism lies in the fact that the polariton properties depend not only on the magnitude of the magnetic field but also on its direction. An applied magnetic field also produces additional branches in spectra of magnetic plasmon-polariton resulting in the multiband propagation accompanied by nonreciprocal effects [9–16]. Thus, a combination of plasmonic and magnetic functionalities opens a prospect toward active devices with an additional degrees of freedom in the control of plasmon-polariton properties, and such systems have already found a number of practical applications in integrated photonic devices for telecommunications (see, for instance [3, 8] and references therein).

In this framework, using superlattices (which typically consist of alternating layers of two partnering materials) that are capable to provide a combined plasmon and magnetic functionality instead of traditional plasmonic systems (in which the presence of a metal-dielectric interface is implied) has great prospects. Particularly, it conditioned by the fact that the superlattices demonstrate many exotic electronic and optical properties uncommon to the homogeneous (bulk) samples due to the presence of additional periodic potential, which period is greater than the original lattice constant [14]. The application of magnetic field to a superlattice leads to the so-called magneto-plasmon-polariton excitations. Properties of the magnetic polaritons in the superlattices of different kinds being under the action of an external static magnetic field have been studied by many authors during several last decades [10–16]. The problem is usually solved within two distinct considerations of gyroelectric media (e.g., semiconductors) with magneto-plasmons [10, 14] and gyromagnetic media (e.g., ferrites) with magnons [11–13, 16], which involve the medium characterization with either permittivity or permeability tensor having asymmetric off-diagonal parts. This distinction is governed by the fact that the resonant frequencies of permeability of magnetic materials usually lie in the

http://dx.doi.org/10.5772/intechopen.71837

microwave range, whereas characteristic frequencies of permittivity of semiconductors commonly are in the infrared range.

At the same time, it is evident that combining together magnetic and semiconductor materials into a single gyroelectromagnetic superlattice in which both permeability and permittivity simultaneously are tensor quantities allows additional possibilities in the control of polaritons using the magnetic field that are unattainable in convenient either gyromagnetic or gyroelectric media. Fortunately, it is possible to design heterostructures in which both characteristic resonant frequencies of semiconductor and magnetic materials are different but, nevertheless, closely spaced in the same frequency band. As a relevant example, the magnetic-semiconductor heterostructures proposed in [17–20] can be mentioned that are able to exhibit a gyroelectromagnetic effect from gigahertz up to tens of terahertz [21]. Thus investigation of electromagnetic properties of such structures in view of their promising application as a part of plasmonic devices is a significant task.

This chapter is devoted to the discussion of dispersion peculiarities of both bulk and surface polaritons propagating in a finely-stratified magnetic-semiconductor superlattice influenced by an external static magnetic field. It is organized as follows. In Section 2, we formulate the problem to be solved and derive effective medium expressions suitable for calculation of the properties of modes under the long-wavelength approximation. Section 3 describes the problem solution in a general case assuming an arbitrary orientation of the external magnetic field with respect to the direction of wave propagation and interface of the structure. The discussion about manifestation of mode crossing and anti-crossing effects is presented in Section 4 involving a concept of the Morse critical points from the catastrophe theory. In Section 5, we reveal dispersion peculiarities of bulk and surface polaritons in the given superlattice for three particular cases of the vector orientation of the external magnetic field with respect to the superlattice's interface and wave vector, namely we study the configurations where the external magnetic field is influenced in the Voigt, polar, and Faraday geometries. Finally, Section 6 summarizes the chapter.

2. Outline of problem

Thereby, in this chapter, we study dispersion features of surface and bulk polaritons propagating in a *semi-infinite* stack of identical composite double-layered slabs arranged along the y-axis that forms a *superlattice* (**Figure 1**). Each composite slab within the superlattice includes magnetic (with constitutive parameters ε_m, $\widehat{\mu}_m$) and semiconductor (with constitutive parameters $\widehat{\varepsilon}_s$, μ_s) layers with thicknesses d_m and d_s, respectively. The stack possesses a periodic structure (with period $L = d_m + d_s$) that fills half-space $y < 0$ and adjoins a vacuum $(\varepsilon_0 = \mu_0 = 1)$ occupying half-space $y > 0$. Therefore, the superlattice's interface lies in the $x - z$ plane, and along this plane, the system is considered to be infinite. The structure under investigation is influenced by an external static magnetic field $\vec{M}$ that lies in the $y - z$ plane and makes an angle θ with the y-axis. It is supposed that the strength of this field is high enough to form a homogeneous saturated state of magnetic as well as semiconductor subsystems. Finally, the

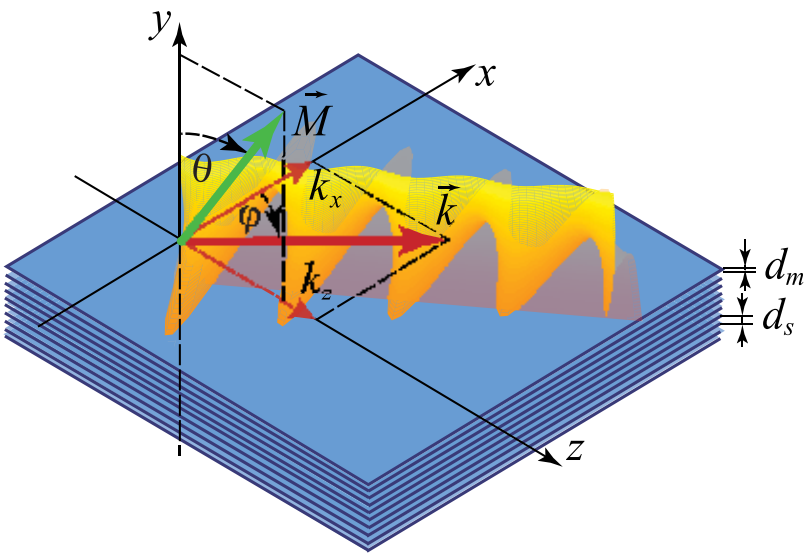

Figure 1. Schematic representation of a magnetic-semiconductor superlattice influenced by an external static magnetic field $\vec{M}$ and a visual representation of the tangential electric field distribution of the surface polariton propagating over the interface between the given structure and free space.

wave vector $\vec{k}$ of the macroscopic electric field lies in the $x-z$ plane and makes an angle φ with the x-axis.

In the general case, when no restrictions are imposed on characteristic dimensions (d_m, d_s, and L) of the superlattice compared to the wavelength of propagating modes, the transfer matrix formalism [22] is usually involved in order to reveal the dispersion features of polaritons. It implies a *numerical* solution of a canonical boundary value problem formulated for each layer within the period of superlattice and then performing a subsequent multiplication of the obtained transfer matrices to form a semi-infinite extent. On the other hand, when all characteristic dimensions of the superlattice satisfy the long-wavelength limit, i.e., they are all much smaller than the wavelength in the corresponding layer and period of structure ($d_m \ll \lambda$, $d_s \ll \lambda$, $L \ll \lambda$), homogenization procedures from the effective medium theory can be involved in order to derive dispersion characteristics in an *explicit* form [24–28] that is suitable for identifying the main features of interest. Therefore, further only the modes under the long-wavelength approximation are studied in this chapter, i.e., the structure is considered to be a *finely-stratified* one.

In order to obtain expressions for the tensors of effective permeability and permittivity of the superlattice in a general form, constitutive equations, $\vec{B}=\mu\vec{H}$ and $\vec{D}=\varepsilon\vec{E}$, for magnetic ($0<z<d_m$) and semiconductor ($d_m<z<L$) layers are represented as follow [26]:

$$Q_\nu^{(j)} = \sum_{\nu'} g_{\nu\nu'}^{(j)} P_{\nu'}^{(j)}, \tag{1}$$

where $\vec{Q}$ takes values of the magnetic and electric flux densities $\vec{B}$ and $\vec{D}$, respectively; $\vec{P}$ is varied between the magnetic and electric field strengths $\vec{H}$ and $\vec{E}$; g is substituted for

permeability and permittivity μ and ε; the superscript j is introduced to distinguish between magnetic ($m \to j$) and semiconductor ($s \to j$) layers; and $\nu\nu'$ iterates over x, y, and z.

In the given structure geometry, the interfaces between adjacent layers within the superlattice lie in the $x - z$ plane, and they are normal to the y-axis; thus, the field components $P_x^{(j)}$, $P_z^{(j)}$, and $Q_y^{(j)}$ are continuous at the interfaces. Therefore, the normal component $P_y^{(j)}$ can be expressed from (1) in terms of the continuous components of the field as follow:

$$P_y^{(j)} = -\frac{g_{yx}^{(j)}}{g_{yy}^{(j)}} P_x^{(j)} + \frac{1}{g_{yy}^{(j)}} Q_y^{(j)} - \frac{g_{yz}^{(j)}}{g_{yy}^{(j)}} P_z^{(j)}, \tag{2}$$

and substituted into equations for components $Q_x^{(j)}$ and $Q_z^{(j)}$:

$$\begin{aligned} Q_x^{(j)} &= \left(g_{xx}^{(j)} - \frac{g_{xy}^{(j)} g_{yx}^{(j)}}{g_{yy}^{(j)}} \right) P_x^{(j)} + \frac{g_{xy}^{(j)}}{g_{yy}^{(j)}} Q_y^{(j)} + \left(g_{xz}^{(j)} - \frac{g_{xy}^{(j)} g_{yz}^{(j)}}{g_{yy}^{(j)}} \right) P_z^{(j)} \\ Q_z^{(j)} &= \left(g_{zx}^{(j)} - \frac{g_{zy}^{(j)} g_{yx}^{(j)}}{g_{yy}^{(j)}} \right) P_x^{(j)} + \frac{g_{zy}^{(j)}}{g_{yy}^{(j)}} Q_y^{(j)} + \left(g_{zz}^{(j)} - \frac{g_{zy}^{(j)} g_{yz}^{(j)}}{g_{yy}^{(j)}} \right) P_z^{(j)}. \end{aligned}, \tag{3}$$

Relations (2) and (3) are then used for the field averaging [24].

With taking into account the long-wavelength limit, the fields $\vec{P}(j)$ and $\vec{Q}(j)$ inside the layers are considered to be constant, and the *averaged* (Maxwell) fields $\left\langle \vec{Q} \right\rangle$ and $\left\langle \vec{P} \right\rangle$ can be determined by the equalities:

$$\left\langle \vec{P} \right\rangle = \frac{1}{L} \sum_j \vec{P}\,(j) d_j, \quad \left\langle \vec{Q} \right\rangle = \frac{1}{L} \sum_j \vec{Q}\,(j) d_j. \tag{4}$$

In view of the continuity of components $P_x^{(j)}$, $P_z^{(j)}$, and $Q_y^{(j)}$, it follows that

$$\langle P_x \rangle = P_x^{(j)}, \quad \langle P_z \rangle = P_z^{(j)}, \quad \left\langle Q_y \right\rangle = Q_y^{(j)}, \tag{5}$$

and with using Eqs. (2) and (3), we can obtain the relations between the averaged field components in the next form:

$$\begin{aligned} \langle Q_x \rangle &= \alpha_{xx} \langle P_x \rangle + \gamma_{xy} \left\langle Q_y \right\rangle + \alpha_{xz} \langle P_z \rangle, \\ \left\langle P_y \right\rangle &= \beta_{yx} \langle P_x \rangle + \beta_{yy} \left\langle Q_y \right\rangle + \beta_{yz} \langle P_z \rangle, \\ \langle Q_z \rangle &= \alpha_{zz} \langle P_x \rangle + \gamma_{zy} \left\langle Q_y \right\rangle + \alpha_{zz} \langle P_z \rangle. \end{aligned} \tag{6}$$

Here, we used the following designations $\alpha_{\nu\nu'} = \sum_j \left(g_{\nu\nu'}^{(j)} - g_{\nu y}^{(j)} g_{y\nu'}^{(j)} / g_{yy}^{(j)} \right) \delta_j$, $\beta_{yy} = \sum_j \left(1 / g_{yy}^{(j)} \right) \delta_j$, $\beta_{yy} = \sum_j \left(g_{y\nu'}^{(j)} / g_{yy}^{(j)} \right) \delta_j$, $\gamma_{\nu y} = \sum_j \left(g_{\nu y}^{(j)} / g_{yy}^{(j)} \right) \delta_j$, $\delta_j = d_j / L$ is filling factor, and $\nu\nu'$ iterates over x and z.

Expressing $\left\langle Q_y \right\rangle$ from the second equation in system (6) and substituting it into the rest two equations, the constitutive equations for the flux densities of the effective medium $\left\langle \vec{Q} \right\rangle = \hat{g}_{eff} \left\langle \vec{P} \right\rangle$ can be derived, where $\hat{g}_{eff}$ is a tensor quantity:

$$\hat{g}_{eff} = \begin{pmatrix} \tilde{\alpha}_{xx} & \tilde{\gamma}_{xy} & \tilde{\alpha}_{xz} \\ \tilde{\beta}_{yx} & \tilde{\beta}_{yy} & \tilde{\beta}_{yz} \\ \tilde{\alpha}_{zx} & \tilde{\gamma}_{zy} & \tilde{\alpha}_{zz} \end{pmatrix} = \begin{pmatrix} \tilde{g}_{xx} & \tilde{g}_{xy} & \tilde{g}_{xz} \\ \tilde{g}_{yx} & \tilde{g}_{yy} & \tilde{g}_{yz} \\ \tilde{g}_{zx} & \tilde{g}_{zy} & \tilde{g}_{zz} \end{pmatrix}, \tag{7}$$

with components $\tilde{\alpha}_{\nu\nu'} = \alpha_{\nu\nu'} - \beta_{y\nu'}\gamma_{\nu y}/\beta_{yy}$, $\tilde{\beta}_{yy} = 1/\tilde{\beta}_{yy}$, $\tilde{\beta}_{y\nu'} = -\beta_{y\nu'}/\beta_{yy}$, and $\tilde{\gamma}_{\nu y} = -\gamma_{\nu y}/\beta_{yy}$.

The expressions for tensor components of the underlying constitutive parameters of magnetic ($\hat{\mu}_m \to \hat{g}^{(m)}$) and semiconductor ($\hat{\varepsilon}_s \to \hat{g}^{(s)}$) layers depend on the orientation of the external magnetic field $\vec{M}$ in the $y-z$ plane which is defined by the angle θ in the form:

$$\hat{g}^{(j)} = \begin{pmatrix} g_1 & i\zeta g_2 & i\xi g_2 \\ -i\zeta g_2 & \zeta^2 g_1 + \xi^2 g_3 & \zeta\xi(g_1 - g_3) \\ -i\xi g_2 & \zeta\xi(g_1 - g_3) & \xi^2 g_1 + \zeta^2 g_3 \end{pmatrix}, \tag{8}$$

where $\zeta = \sin\theta$ and $\xi = \cos\theta$.

For magnetic layers [29], the components of tensor $\hat{g}^{(m)}$ are $g_1 = 1 + \chi' + i\chi''$, $g_2 = \Omega' + i\Omega''$, $g_3 = 1$ and $\chi' = \omega_0\omega_m\left[\omega_0^2 - \omega^2\left(1-b^2\right)\right]D^{-1}$, $\chi'' = \omega\omega_m b\left[\omega_0^2 + \omega^2\left(1+b^2\right)\right]D^{-1}$, $\Omega' = \omega\omega_m\left[\omega_0^2 - \omega^2\left(1+b^2\right)\right]D^{-1}$, $\Omega'' = 2\omega^2\omega_0\omega_m bD^{-1}$, and $D = \left[\omega_0^2 - \omega^2\left(1+b^2\right)\right]^2 + 4\omega_0^2\omega b^2$, where ω_0 is the Larmor frequency and b is a dimensionless damping constant.

For semiconductor layers [23], the components of tensor $\hat{g}^{(s)}$are $g_1 = \varepsilon_l\left[1 - \omega_p^2(\omega + i\nu)[\omega((\omega + i\nu)^2 - \omega_c^2)]^{-1}\right]$, $g_2 = \varepsilon_l\omega_p^2\omega_c\left[\omega\left((\omega + i\nu)^2 - \omega_c^2\right)\right]^{-1}$, and $g_3 = \varepsilon_l\left[1 - \left[\omega_p^2(\omega + i\nu)\right]^{-1}\right]$, where ε_l is the part of permittivity attributed to the lattice, ω_p is the plasma frequency, ω_c is the cyclotron frequency, and ν is the electron collision frequency in plasma.

Permittivity ε_m of the magnetic layers as well as permeability μ_s of the semiconductor layers are scalar quantities.

Hereinafter, we consider two specific orientations of the external magnetic field vector $\vec{M}$ with respect to the superlattice's interface (see **Figure 1**), namely (i) the polar configuration in which $\theta = 0$ and the vector $\vec{M}$ is parallel to the surface normal ($\vec{M} \| y$) and (ii) $\theta = \pi/2$ and the vector $\vec{M}$ is parallel to the surface plane ($\vec{M} \| z$), which is inherent in both the Voigt and Faraday configurations.

When $\vec{M} \| y$, then $\zeta = 0$, $\xi = 1$, and tensor (8) is reduced to the form

$$\hat{g}^{(j)} = \begin{pmatrix} g_1 & 0 & ig_2 \\ 0 & g_3 & 0 \\ -ig_2 & 0 & g_1 \end{pmatrix}, \tag{9}$$

and for the components of tensor (7), we have following expressions: $\tilde{\gamma}_{xy} = \tilde{\gamma}_{zy} = \tilde{\beta}_{yx} = \tilde{\beta}_{yz} = 0$, $\tilde{\alpha}_{xx} = g_{xx}^{(m)}\delta_m + g_{xx}^{(s)}\delta_s$, $\tilde{\alpha}_{zz} = g_{zz}^{(m)}\delta_m + g_{zz}^{(s)}\delta_s$, $\tilde{\alpha}_{xz} = -\tilde{\alpha}_{zx} = g_{zx}^{(m)}\delta_m + g_{zx}^{(s)}\delta_s$, and $\tilde{\beta}_{yy} = g_{yy}^{(m)} g_{yy}^{(s)} \tau$, where $\tau = \left(g_{yy}^{(m)}\delta_s + g_{yy}^{(s)}\delta_m\right)^{-1}$.

In the second case, when $\vec{M} \| z$, then $\zeta = 1$, $\xi = 0$, and tensor (8) has the form

$$\hat{g}^{(j)} = \begin{pmatrix} g_1 & ig_2 & 0 \\ -ig_2 & g_1 & 0 \\ 0 & 0 & g_3 \end{pmatrix}. \tag{10}$$

In this configuration, the components of tensor (7) can be written as follows: $\tilde{\alpha}_{xz} = \tilde{\alpha}_{zx} = \tilde{\gamma}_{zy} = \tilde{\beta}_{yz} = 0$, $\tilde{\alpha}_{xx} = g_{xx}^{(m)}\delta_m + g_{xx}^{(s)}\delta_s + \left(g_{xy}^{(m)} - g_{xy}^{(s)}\right)^2 \delta_m\delta_s\tau$, $\tilde{\alpha}_{zz} = g_{zz}^{(m)}\delta_m + g_{zz}^{(s)}\delta_s$, $\tilde{\gamma}_{xy} = -\tilde{\beta}_{yx} = \left(g_{xy}^{(m)} g_{yy}^{(s)}\delta_m + g_{xy}^{(s)} g_{yy}^{(m)}\delta_s\right)\tau$, and $\tilde{\beta}_{yy} = g_{yy}^{(m)} g_{yy}^{(s)}\tau$.

For further reference, the dispersion curves of the tensor components of relative effective permeability $\hat{\mu}_{eff}$ and relative effective permittivity $\hat{\varepsilon}_{eff}$ of the homogenized medium (with filling factors $\delta_m = \delta_s = 0.5$) are presented in **Figure 2**. **Figure 2(a)** and **(b)** represents constitutive parameters for the polar configuration, whereas **Figure 2(c)** and **(d)** represents those for the Voigt and Faraday configurations of magnetization. For these calculations, we used typical constitutive parameters for magnetic and semiconductor materials. In particular, here we follow the results of paper [30], where a magnetic-semiconductor composite is made in the form of a barium-cobalt/doped-silicon superlattice for operating in the microwave part of spectrum. A distinct peculiarity of such a superlattice is that the characteristic resonant frequencies of the underlying constitutive magnetic and semiconductor materials are closely spaced within the same frequency band.

From **Figure 2**, one can conclude that in both the Voigt and Faraday geometries, the next relations between the components of effective tensor (7) hold $\tilde{g}_{xx} \neq \tilde{g}_{yy} \neq \tilde{g}_{zz}$ and $\tilde{g}_{xy} = -\tilde{g}_{yx} \neq 0$, so it means that the obtained homogenized medium is a *biaxial* bigyrotropic crystal [1]. In the polar geometry, it is a *uniaxial* bigyrotropic crystal, and the following relations between tensor components are met: $\tilde{g}_{xx} = \tilde{g}_{zz} \neq \tilde{g}_{yy}$ and $\tilde{g}_{xz} = -\tilde{g}_{zx} \neq 0$.

To sum up, with an assistance of the homogenization procedures from the effective medium theory, the superlattice under study is approximately represented as a uniaxial or biaxial anisotropic uniform medium when an external static magnetic field $\vec{M}$ is directed along or

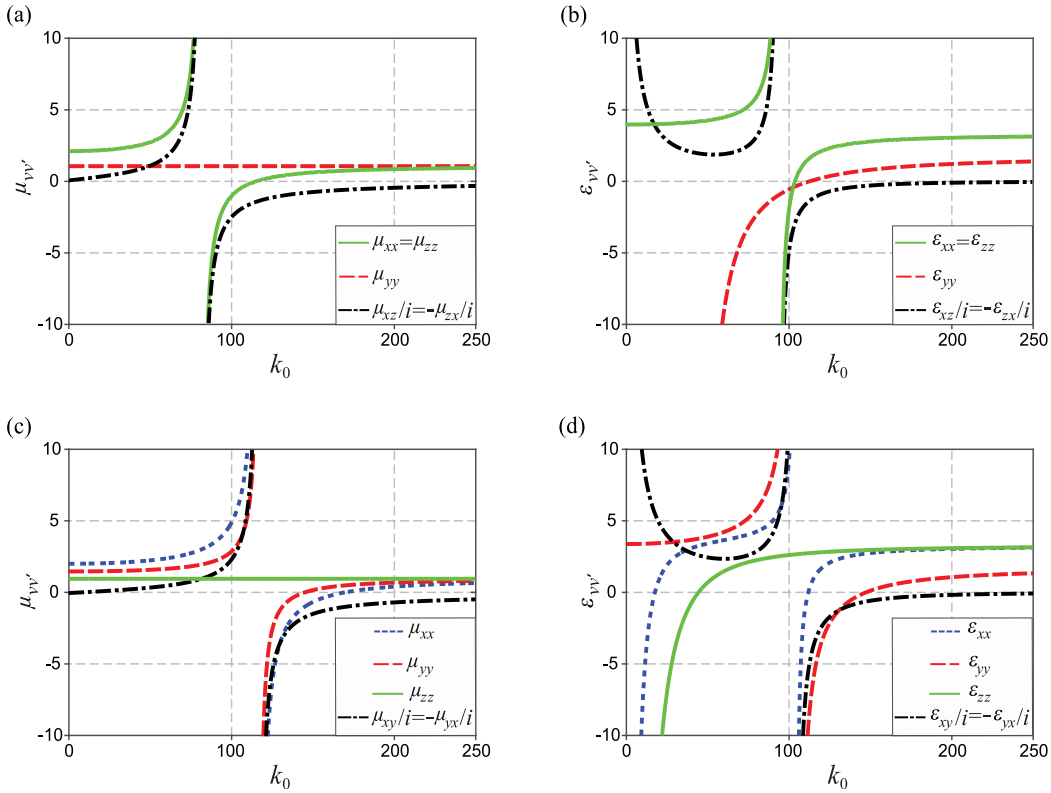

Figure 2. Dispersion curves of the tensor components of (a, c) relative effective permeability $\hat{\mu}_{eff}$ and (b, d) relative effective permittivity $\hat{\varepsilon}_{eff}$ of the homogenized medium. Panels (a) and (b) correspond to the polar geometry and panels (c) and (d) correspond to the Voigt and Faraday geometries. For the magnetic constitutive layers, under saturation magnetization of 2930 G, parameters are $f_0 = \omega_0/2\pi = 3.9$ GHz, $f_m = \omega_m/2\pi = 8.2$ GHz, $b = 0$, and $\varepsilon_m = 5.5$; for the semiconductor constitutive layers, parameters are $f_p = \omega_p/2\pi = 5.5$ GHz, $f_c = \omega_c/2\pi = 4.5$ GHz, $\nu = 0$, $\varepsilon_l = 1.0$, and $\mu_s = 1.0$. Filling factors are $\delta_m = \delta_s = 0.5$.

orthogonal to the structure periodicity, respectively. In the latter case, the first optical axis of the biaxial medium is directed along the structure periodicity, whereas the second one coincides with the direction of the external static magnetic field $\vec{M}$.

3. General solution for bulk and surface polaritons

In order to obtain a *general* solution for both bulk and surface polaritons, we follow the approach developed in Ref. [10] where dispersion characteristics of polaritons in a uniaxial anisotropic dielectric medium have been studied. Here, we extend this approach to the case of a gyroelectromagnetic medium whose permittivity and permeability simultaneously are tensor quantities.

In a general form [26], the electric and magnetic field vectors $\vec{E}$ and $\vec{H}$ used here are represented as

$$\vec{P}^{(j)} = \vec{p}^{(j)} \exp\left[i(k_x x + k_z z)\right] \exp\left(\mp \kappa y\right), \tag{11}$$

where a time factor $\exp(-i\omega t)$ is also supposed and omitted, and sign $"-"$ is related to the fields in the upper medium ($y > 0,\ j = 0$), while sign $"+"$ is related to the fields in the composite medium ($y < 0,\ j = 1$), respectively, which provide required wave attenuation along the y-axis.

From a pair of the curl Maxwell's equations $\nabla\times \vec{E} = ik_0 \vec{B}$ and $\nabla\times \vec{H} = -ik_0 \vec{D}$, in a standard way, we arrive at the following equation for the macroscopic field:

$$\nabla \times \nabla \times \vec{P}^{(j)} - k_0^2 \widehat{\varsigma}^{(j)} \vec{P}^{(j)} = 0, \tag{12}$$

where $k_0 = \omega/c$ is the free-space wavenumber and $\widehat{\varsigma}^{(j)}$ is introduced as the product of $\widehat{\mu}^{(j)}$ and $\widehat{\varepsilon}^{(j)}$ made in the appropriate order.

For the upper medium ($j = 0$), direct substitution of expression (11) with $\vec{P}^{(0)}$ and corresponding constitutive parameters ($\widehat{\varsigma}^{(0)}_{\nu\nu'} = 1$ for $\nu = \nu'$ and $\widehat{\varsigma}^{(0)}_{\nu\nu'} = 0$ for $\nu \neq \nu'$; here and further subscripts ν and ν' are substituted to iterate over indexes of the tensor components x, y, and z in Cartesian coordinates) into Eq. (12) gives us the relation with respect to κ_0:

$$\kappa_0^2 = k^2 - k_0^2, \tag{13}$$

where $k^2 = k_x^2 + k_z^2$.

For the composite medium ($j = 1$), substitution of (11) with $\vec{P}^{(1)}$ and $\widehat{\varsigma}^{(1)}$ into (12) and subsequent elimination of $P_y^{(1)}$ yield us the following system of two homogeneous algebraic equations for the rest two components of $\vec{P}^{(1)}$:

$$\begin{aligned} A_{xz} P_x^{(1)} + B_{xz} P_z^{(1)} &= 0, \\ B_{zx} P_x^{(1)} + A_{zx} P_z^{(1)} &= 0, \end{aligned} \tag{14}$$

where A_{nm} and B_{nm} are functions of κ derived in the form [10]:

$$\begin{aligned} A_{nm}(\kappa) &= \left(k_m^2 - k_0^2 \varsigma_{nm}^{(1)} - \kappa^2\right) \varkappa_y^2 + k_n^2 \kappa^2 + i k_n \kappa \left(\varsigma_{ny}^{(1)} + \varsigma_{yn}^{(1)}\right) k_0^2 - k_0^4 \varsigma_{ny}^{(1)} \varsigma_{yn}^{(1)}, \\ B_{nm}(\kappa) &= -\left(k_n k_m + \varsigma_{nm}^{(1)}\right) \varkappa_y^2 + k_n k_m \kappa^2 + i\kappa \left(k_n \varsigma_{ym}^{(1)} + k_m \varsigma_{ny}^{(1)}\right) k_0^2 - k_0^4 \varsigma_{ny}^{(1)} \varsigma_{ym}^{(1)}, \end{aligned} \tag{15}$$

with $\varkappa_y^2 = k^2 - k_0^2 \varsigma_{yy}^{(1)}$, and subscripts m and n iterate over indexes x and z.

In order to find a nontrivial solution of system (15), we set its determinant of coefficients to zero. After disclosure of the determinant, we obtain an equation of the fourth degree with respect to κ:

$$\varsigma_{yy}^{(1)}\kappa^4 + a\kappa^3 + b\kappa^2 + c\kappa + d = 0, \tag{16}$$

whose coefficients a, b, c, and d are

$$\begin{aligned}
a &= ik_x\left(\varsigma_{yz}^{(1)} + \varsigma_{zy}^{(1)}\right) + ik_z\left(\varsigma_{yx}^{(1)} + \varsigma_{xy}^{(1)}\right),\\
b &= k_0^2\left[\varsigma_{yy}^{(1)}\left(\varsigma_{zz}^{(1)} + \varsigma_{xx}^{(1)}\right) - \varsigma_{zy}^{(1)}\varsigma_{yz}^{(1)} - \varsigma_{xy}^{(1)}\varsigma_{yx}^{(1)}\right]\\
&\quad -\left[k^2\varsigma_{yy}^{(1)} + k_z^2\varsigma_{zz}^{(1)} + k_x^2\varsigma_{xx}^{(1)} + k_xk_z\left(\varsigma_{zx}^{(1)} + \varsigma_{xz}^{(1)}\right)\right],\\
c &= -ik_0^2\left\{k_z\left[\varsigma_{xy}^{(1)}\varsigma_{zx}^{(1)} + \varsigma_{yx}^{(1)}\varsigma_{xz}^{(1)} - \varsigma_{xx}^{(1)}\left(\varsigma_{yz}^{(1)} + \varsigma_{zy}^{(1)}\right)\right]\right.\\
&\quad \left.+k_x\left[\varsigma_{yz}^{(1)}\varsigma_{zx}^{(1)} + \varsigma_{zy}^{(1)}\varsigma_{xz}^{(1)} - \varsigma_{zz}^{(1)}\left(\varsigma_{yx}^{(1)} + \varsigma_{xy}^{(1)}\right)\right]\right\}\\
&\quad -ik^2\left[k_z\left(\varsigma_{yz}^{(1)} + \varsigma_{zy}^{(1)}\right) + k_x\left(\varsigma_{yx}^{(1)} + \varsigma_{xy}^{(1)}\right)\right],\\
d &= k^2\left[k_z^2\varsigma_{zz}^{(1)} + k_x^2\varsigma_{xx}^{(1)} + k_xk_z\left(\varsigma_{zx}^{(1)} + \varsigma_{xz}^{(1)}\right)\right] + k_0^2k^2\left[\varsigma_{zx}^{(1)}\varsigma_{xz}^{(1)} - \varsigma_{zz}^{(1)}\varsigma_{xx}^{(1)}\right]\\
&\quad +k_0^2\left\{k_x^2\left(\varsigma_{xy}^{(1)}\varsigma_{yx}^{(1)} - \varsigma_{yy}^{(1)}\varsigma_{xx}^{(1)}\right) + k_z^2\left(\varsigma_{zy}^{(1)}\varsigma_{yz}^{(1)} - \varsigma_{yy}^{(1)}\varsigma_{zz}^{(1)}\right)\right.\\
&\quad \left.+k_xk_z\left[\varsigma_{xy}^{(1)}\varsigma_{yz}^{(1)} + \varsigma_{zy}^{(1)}\varsigma_{yx}^{(1)} - \varsigma_{yy}^{(1)}\left(\varsigma_{zx}^{(1)} + \varsigma_{xz}^{(1)}\right)\right]\right\}\\
&\quad +k_0^4\left[\varsigma_{xx}^{(1)}\varsigma_{yy}^{(1)}\varsigma_{zz}^{(1)} - \varsigma_{yy}^{(1)}\varsigma_{zx}^{(1)}\varsigma_{xz}^{(1)} + \varsigma_{xy}^{(1)}\left(\varsigma_{yz}^{(1)}\varsigma_{zx}^{(1)} - \varsigma_{zz}^{(1)}\varsigma_{yx}^{(1)}\right)\right.\\
&\quad \left.+\varsigma_{zy}^{(1)}\left(\varsigma_{xz}^{(1)}\varsigma_{yx}^{(1)} - \varsigma_{yz}^{(1)}\varsigma_{xx}^{(1)}\right)\right].
\end{aligned} \tag{17}$$

The dispersion relation for *bulk* polaritons is then obtained straightforwardly from (16) by putting $\kappa = 0$ inside it.

In order to find the dispersion law of surface polaritons from four roots of (16), two physically correct ones must be selected. In general, two such roots are required to satisfy the electromagnetic boundary conditions at the surface of the composite medium. We define these roots as κ_1 and κ_2 and then following [10] introduce the quantities K_w ($w = 1, 2$) in the form:

$$\begin{aligned}
P_x^{(1)}(\kappa_w) &= K_w A_{zx}(\kappa_w),\\
P_y^{(1)}(\kappa_w) &= K_w C(\kappa_w),\\
P_z^{(1)}(\kappa_w) &= -K_w B_{zx}(\kappa_w),
\end{aligned} \tag{18}$$

where $C(\kappa_w) = -\left(1/\varkappa_y^2\right)\left[\left(ik_x\kappa_w - k_0^2\varsigma_{yx}^{(1)}\right)A_{zx}(\kappa_w) + \left(ik_z\kappa_w - k_0^2\varsigma_{yz}^{(1)}\right)B_{zx}(\kappa_w)\right]$.

In (18), unknown quantities K_w need to be determined from the boundary conditions.

http://dx.doi.org/10.5772/intechopen.71837

Taking into consideration that two appropriate roots κ_1 and κ_2 of (16) are selected, the components of the field $\vec{P}^{(1)}$ can be rewritten as the linear superposition of two terms:

$$\begin{aligned} P_x^{(1)} &= \sum_{w=1,2} K_w A_{zx}(\kappa_w) \exp(\kappa_w y), \\ P_y^{(1)} &= \sum_{w=1,2} K_w C(\kappa_w) \exp(\kappa_w y), \\ P_z^{(1)} &= \sum_{w=1,2} K_w B_{zx}(\kappa_w) \exp(\kappa_w y), \end{aligned} \tag{19}$$

where $y < 0$ and the factor $\exp[i(k_x x + k_z z - \omega t)]$ is omitted.

Involving a pair of the divergent Maxwell's equations $\nabla \cdot \vec{B} = 0$ and $\nabla \cdot \vec{D} = 0$ in the form

$$\nabla \cdot \vec{Q}^{(j)} = \nabla \cdot \left(\hat{g}^{(j)} P^{(j)}\right) = 0, \tag{20}$$

where g is substituted for permeability μ and permittivity ε and $\vec{Q}$ is substituted for the magnetic $\vec{B}$ and electric $\vec{D}$ flux densities; one can immediately obtain the relations between the field components in the upper ($y > 0$) medium as follows:

$$Q_y^{(0)} = \left(ig_0/\kappa_0\right)\left(k_x P_x^{(0)} + k_z P_z^{(0)}\right). \tag{21}$$

The boundary conditions at the interface require the continuity of the tangential components of $\vec{E}$ and $\vec{H}$ as well as the normal components of $\vec{D}$ and $\vec{B}$, i.e., in our notations these components are P_x, P_z, and Q_y, respectively. Thus, application of the boundary conditions together with (21) gives us the next set of equations:

$$\begin{aligned} \left(ig_0/\kappa_0\right)\left(k_x P_x^{(0)} + k_z P_z^{(0)}\right) &= \tilde{g}_{yx} \sum_{w=1,2} K_w A_{zx}(\kappa_w) \\ &+ \tilde{g}_{yx} \sum_{w=1,2} K_w C(\kappa_w) - \tilde{g}_{yz} \sum_{w=1,2} K_w B_{zx}(\kappa_w), \\ P_x^{(0)} &= \sum_{w=1,2} K_w A_{zx}(\kappa_w), \\ P_z^{(0)} &= -\sum_{w=1,2} K_w B_{zx}(\kappa_w), \\ k_z P_x^{(0)} - k_x P_z^{(0)} &= k_z \sum_{w=1,2} K_w A_{zx}(\kappa_w) + k_x \sum_{w=1,2} K_w B_{zx}(\kappa_w). \end{aligned} \tag{22}$$

The system of Eq. (22) has a nontrivial solution only if its determinant vanishes. Applying this condition gives us the required dispersion equation for *surface* polaritons.

Finally, the amplitudes K_1 and K_2 can be found by solving set of linear homogeneous Eq. (22). They are

$$\begin{aligned} K_1 &= [k_x A_{zx}(\kappa_2) + k_z B_{zx}(\kappa_2)](\kappa_0 + \kappa_2), \\ K_2 &= -[k_x B_{zx}(\kappa_1) + k_z A_{zx}(\kappa_1)](\kappa_0 + \kappa_1). \end{aligned} \tag{23}$$

Here, the problem is considered to be formally solved, and the dispersion relations are derived in a general form for both bulk and surface polaritons.

4. Theory of Morse critical points: mode coupling phenomena

Further, for brevity, obtained dispersion equations for the bulk and surface polaritons are denoted in the form:

$$\mathfrak{D}(k, k_0) = 0. \tag{24}$$

Numerical solution of Eq. (24) gives a set of dispersion curves $k_0(k)$ of polaritons, which can contain both regular and singular (critical) points. The regular points draw dispersion curves of a classical form possessing either normal or anomalous dispersion line, at which a small variation in k_0 results in a smooth changing in the form of the curves. Besides, some situations are possible when a slight variation in k_0 leads to a very sharp (catastrophic) changing in the form of dispersion curves. Such singularities (extreme states) can be accompanied by mutual coupling phenomena of modes, which are further of our interest.

From the mathematical point of view the found extreme states in dispersion curves exist in the region where the differential $\mathfrak{D}'(k, k_0)$ of dispersion Eq. (24) vanishes (see, e.g., **Figure 3**). These extreme states can be carefully identified and studied involving the approach based on the theory of the Morse critical points from the catastrophe theory [31–36]. This treatment has been originally applied to study open waveguides and resonators [31, 32], and later it has been extended to more complex waveguide structures [33–35]. From viewpoint of this theory, the presence of the Morse critical points is generally defined by a set of nonlinear differential equations written in the form [33]:

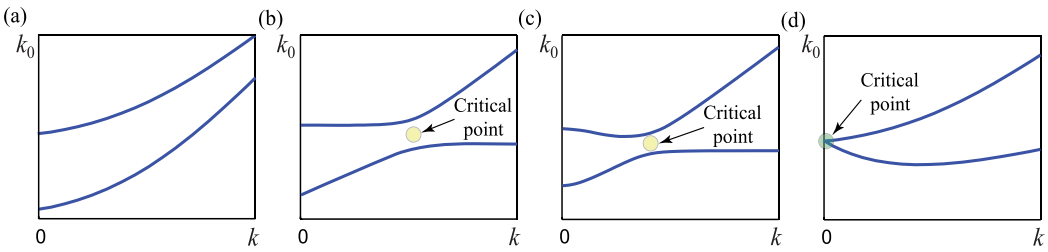

Figure 3. Sketch of the band diagrams presenting different kinds of interaction between two neighboring modes: (a) weak interaction, (b) intermediate interaction, (c) strong interaction, and (d) accidental degeneracy. Areas where the critical points exist are pointed by circles.

http://dx.doi.org/10.5772/intechopen.71837

$$\begin{aligned} \mathfrak{D}'_k(k,k_0)\big|_{\left(k^m,k_0^m\right)} &= \mathfrak{D}'_{k_0}(k,k_0)\big|_{\left(k^m,k_0^m\right)} = 0, \\ \mathbb{H} &= [h_{11}h_{22} - h_{12}h_{21}]\big|_{\left(k^m,k_0^m\right)} \neq 0, \end{aligned} \tag{25}$$

where $\left(k^m, k_0^m\right)$ are coordinates in the $k - k_0$ plane of a particular m-th Morse critical point, the subscripts k and k_0 near the letter $\mathfrak{D}$ define corresponding partial derivatives $\partial/\partial k$ and $\partial/\partial k_0$, and $\mathbb{H}$ is the Hessian determinant with elements:

$$\begin{aligned} h_{11} &= \mathfrak{D}''_{kk}(k,k_0), \quad h_{12} = \mathfrak{D}''_{kk_0}(k,k_0), \\ h_{21} &= \mathfrak{D}''_{k_0k}(k,k_0), \quad h_{22} = \mathfrak{D}''_{k_0k_0}(k,k_0). \end{aligned} \tag{26}$$

The type of each extreme state defined by set of Eq. (25) can be uniquely identified from the sign of the Hessian determinant [35]. For instance, when $\mathbb{H} < 0$, the corresponding Morse critical point represents a saddle point, which occurs in the region of a modal coupling (the *anti-crossing* effect), whereas in the case of degeneracy, when $\mathbb{H} = 0$, it is a non-isolated critical point (the *crossing* effect). In the case when $\mathbb{H} > 0$, the Morse critical point defines either a local minimum or maximum (this case is not considered here). In what follows we distinguish found critical points by circles for both crossing and anti-crossing effects, as shown in **Figure 3**.

In general, when conditions (25) are met, the type of interacting modes in the vicinity of the corresponding Morse critical point can be defined as follows [33]:

$$\textit{Codirectional forward}: \quad h_{12}/h_{11} < 0, \quad h_{22}/h_{11} > 0; \tag{27}$$

$$\textit{Codirectional backward}: \quad h_{12}/h_{11} > 0, \quad h_{22}/h_{11} > 0; \tag{28}$$

$$\textit{Contradirectional}: \quad h_{12}/h_{11} > 0, \quad h_{22}/h_{11} < 0. \tag{29}$$

The strength of modes interaction within the found extreme states in the region of their coupling can be identified considering the classification introduced in paper [37], which concerns on the mode behaviors appearing in axial waveguides. In particular, (i) a weak interaction takes place when frequency band gap between dispersion curves of interacting modes is high enough (**Figure 3a**), (ii) an intermediate interaction of modes leads to formation of very flattened parts in the dispersion curves (**Figure 3b**), (iii) a strong interaction appears when the repulsion between modes is strong enough resulting in formation of dispersion curve having anomalous dispersion line (**Figure 3c**), and (iv) an accidental degeneracy arises when two dispersion branches are merged within the critical point which leads to nonzero group velocities at $k = 0$ (**Figure 3d**).

The strong interaction with forming negative-slope region in dispersion curve of one of interacting modes (as it is depicted in **Figure 3c** and **d**) leads to some unusual effects [37]. First, zero group velocity ($v_g = \partial k_0/\partial k$) can appear at a nonzero value of k. The flattened region of the dispersion curve around that extreme point (**Figure 3c**) is very useful for applications in nonlinear optics, where a small group velocity is suitable for enhancing nonlinear effects, while the phase-matching criterion can still be satisfied because the wave vector is nonzero. Second,

when interacting modes are exactly degenerated, then their group velocities appear to be nonzero and roughly constant values as $k \to 0$ (**Figure 3d**). From viewpoint of practical applications, this situation is useful, because regular modes in the vicinity of $k = 0$ have extremely small value of their group velocity and thus become unusable. Since both dispersion and losses are inversely proportional to $v_{g,}$ they diverge when $k \to 0$.

At the same time, the intermediate interaction with forming extremely flattened part in the mode dispersion curve (see **Figure 3b**) leads to strong divergence in density of states, and it can be utilized in designs of low-threshold lasers [37].

5. Dispersion features of bulk and surface polaritons for three particular orientations of magnetization

Since further our goal is to elucidate the dispersion laws of the bulk and surface polaritons (which are in fact *eigenwaves*), we are interested in real solutions of Eq. (24). In order to find the real solutions, the absence of losses in constitutive parameters of the underlying layers is supposed.

We consider three particular orientations of the external magnetic field $\vec{M}$ with respect to the superlattice's interface (the $x - z$ plane) and to the wave vector $\vec{k}$, namely, (i) the *polar geometry* in which the external magnetic field is applied perpendicular to both the direction of wave propagation ($\vec{M} \perp \vec{k}$) and structure's interface ($\vec{M} \| y$) as shown in **Figure 4a**; (ii) the *Voigt geometry* in which the external magnetic field is applied parallel to the structure's interface, and it is perpendicular to the direction of the wave propagation, so $\vec{M} \| z$ and $\vec{M} \perp \vec{k}$ as presented in **Figure 4b**; (iii) the *Faraday geometry* in which the external magnetic field is applied parallel to both the direction of wave propagation and structure's interface, i.e., $\vec{M} \| z$ and $\vec{M} \| \vec{k}$ as presented in **Figure 4c**.

With respect to the problem of polaritons, in any kind of an unbounded gyrotropic medium, there are two distinct eigenwaves (the bulk waves), whereas the surface waves split apart only

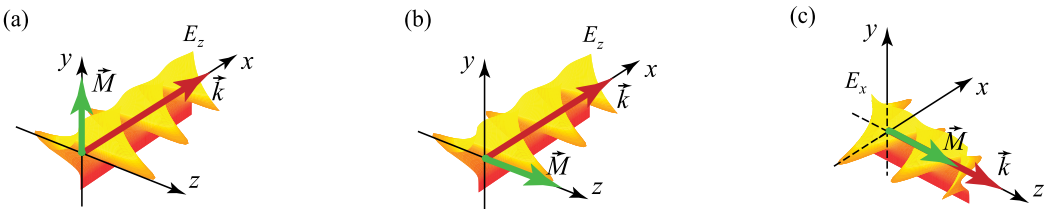

Figure 4. Three particular orientations of the external magnetic field vector $\vec{M}$ with respect to the superlattice's interface and wave vector; (a) polar geometry, $\vec{M} \| y$, $\vec{M} \perp \vec{k}$; (b) Voigt geometry, $\vec{M} \| z$, $\vec{M} \perp \vec{k}$; and (c) Faraday geometry $\vec{M} \| z$, $\vec{M} \| \vec{k}$.

http://dx.doi.org/10.5772/intechopen.71837

for some particular configurations (e.g., for the Voigt geometry), and generally, the field has all six components. Such surface waves are classified as hybrid EH modes and HE modes, and these modes appear as some superposition of longitudinal and transverse waves. By analogy with [38], we classify hybrid modes depending on the magnitude ratio between the longitudinal electric and magnetic field components (P_x and P_z components for the polar and Faraday geometries, respectively). For instance, for the polar configuration, it is supposed that the wave has the EH type if $E_x > H_x$ and the HE type if $H_x > E_x$. Contrariwise, in the Faraday geometry, we stipulate that the wave has the EH type if $E_z > H_z$ and the HE type if $H_z > E_z$. In the Voigt geometry, the waves appear as transverse electric (TE) and transverse magnetic (TM) modes, where each of them has three field components.

The polariton dispersion relations for these specific cases of magnetization can be obtained using general results derived in Section 3 with application of appropriate boundary and initial conditions.

When an external static magnetic field is influenced in the Voigt geometry ($\vec{M} \| z, \quad \vec{M} \perp \vec{k}$), solution of Eq. (16) for both bulk and surface waves splits apart into two independent equations for distinct polarizations [10], namely, TE modes with field components $\{H_x, H_y, E_z\}$ and TM modes with field components $\{E_x, E_y, H_z\}$. Therefore, regions of existence of bulk polaritons are uniquely determined by solutions of two separated equations related to the TE and the TM modes as follows [26, 38]:

$$k_x^2 - k_0^2 \varepsilon_{zz} \mu_v \mu_{yy} \mu_{xx}^{-1} = 0, \tag{30}$$

$$k_x^2 - k_0^2 \mu_{zz} \varepsilon_v \varepsilon_{yy} \varepsilon_{xx}^{-1} = 0, \tag{31}$$

where $\varepsilon_v = \varepsilon_{xx} + \varepsilon_{xy}^2/\varepsilon_{yy}$ and $\mu_v = \mu_{xx} + \mu_{xy}^2/\mu_{yy}$ are the Voigt relative permittivity and permeability, respectively.

Under such magnetization, the dispersion equation for the surface polaritons at the interface between vacuum and the given structure has the form [26]:

$$\kappa_1 g_v + \kappa_2 g_0 + i k_x g_0 \tilde{g}_{xy} \tilde{g}_{yy}^{-1} = 0, \tag{32}$$

where substitutions $\mu \to g$ and $\varepsilon \to g$ are related to the TE and TM modes, respectively.

We should note that in two particular cases of the gyroelectric and gyromagnetic superlattices, dispersion relation (32) coincides with Eq. (33) of Ref. [10] and Eq. (21) of Ref. [15], respectively, which verifies the obtained solution.

It follows from **Figure 4b** that in the Voigt geometry, the magnetic field vector in the TM mode has components $\{0, 0, H_z\}$, and it is parallel to the external magnetic field $\vec{M}$, which results in the absence of its interaction with the magnetic subsystem [39–41]. Thus, hereinafter dispersion features only of the TE mode are of interest for which the dispersion equation for surface polaritons (32) can be rewritten as

$$\kappa_1 \mu_v + \kappa_2 \mu_0 + i k_x \mu_0 \mu_{xy} \mu_{yy}^{-1} = 0. \tag{33}$$

Importantly, since the dispersion equation consists of a term which is linearly depended on k_x (the last term in (33)), the spectral characteristics of the surface polaritons in the structure under study possess the nonreciprocal nature, i.e., $k_0(k_x) \neq k_0(-k_x)$.

A complete set of dispersion curves obtained from solution of Eq. (30) that outlines the passbands of the TE bulk polaritons as a function of the filling factor δ_m is presented in **Figure 5a**. One can see that behaviors of the TE bulk polaritons are quite trivial in the overwhelming majority of structure's configurations, namely, there are two isolated passbands separated by a forbidden band. The upper passband is bounded laterally by the light line, and its lower limit is restricted by the line at which $\mu_v = 0$. The bottom passband starts on the line where $\varepsilon_{zz} = 0$ and then approaches the asymptotic frequency ($k_x \to \infty$) at which $\mu_{xx} = 0$ (see Eq. (25)).

In this study, we are mainly interested in those curves of the set which have greatly sloping branches and exhibit the closest approaching each other (i.e., they manifest the anti-crossing effect) or have a crossing point, since such dispersion behaviors correspond to the existence of the Morse critical points. Hereinafter, the areas of interest in which these extreme states exist are denoted in figures by orange circles.

It follows from **Figure 5a** that in the Voigt geometry, both the anti-crossing ($\mathbb{H} < 0$) and crossing ($\mathbb{H} = 0$) effects with forming the bottom branch characterized by the anomalous dispersion (i.e., the strong mode interaction occurs) can be achieved in the composite structure with a predominant impact of the semiconductor subsystem (further we stipulate that the composite system has a predominant impact of either magnetic subsystem or semiconductor subsystem if $\delta_m \gg \delta_s$ or $\delta_s \gg \delta_m$, respectively). Moreover, since condition (29) is met near the critical point, the bulk waves appear to be contradirectional.

The crossing effect is found to be at $k_x \to 0$ (accidentally degenerate modes) for the particular configuration of the structure, when $\delta_m = 0.132$ (**Figure 5b**). Remarkably, such an extreme state corresponds to a particular frequency where ε_{zz} and μ_v simultaneously acquire zero [26].

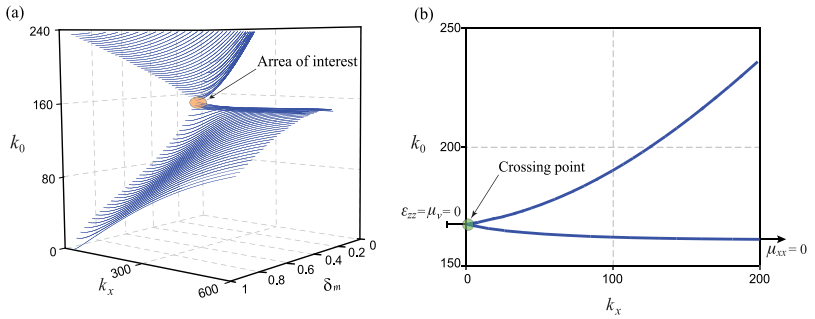

Figure 5. (a) A set of dispersion curves of the TE bulk polaritons for different filling factors δ_m for the structure being in the Voigt geometry and (b) manifestation of crossing effect in dispersion curves of the TE bulk polaritons at the particular value of filling factor $\delta_m = 0.132$. Parameters of magnetic constitutive layers are shown in **Figure 2**. For the semiconductor constitutive layers, parameters are $f_p = \omega_p/2\pi = 10.5$ GHz, $f_c = \omega_c/2\pi = 9.5$ GHz, $\nu = 0$, $\varepsilon_l = 1.0$, and $\mu_s = 1.0$.

http://dx.doi.org/10.5772/intechopen.71837

In the polar geometry ($\vec{M} \| y, \quad \vec{M} \perp \vec{k}$), composite medium under study is a uniaxial crystal whose optical axis is directed along the y-axis. In this case, bulk polaritons split onto two waves with field components $\{E_x, H_y, E_z\}$ and $\{H_x, E_y, H_z\}$, respectively [40], and their continua is outlined by two dispersion relations:

$$k_x^2 - k_0^2 \mu_{yy} \varepsilon_{yy} = 0, \tag{34}$$

$$k_x^2 - k_0^2 \mu_v \varepsilon_v \left[1 - \mu_{xz}\varepsilon_{xz}/\left(\mu_{xx}\varepsilon_{xx}\right)\right]^{-1} = 0, \tag{35}$$

where $\varepsilon_v = \varepsilon_{xx} + \varepsilon_{xz}^2/\varepsilon_{xx}$ and $\mu_v = \mu_{xx} + \mu_{xz}^2/\mu_{xx}$ are introduced as the effective bulk permeability and permittivity, respectively.

Hereinafter, we distinguish these two kinds of waves as ordinary and extraordinary bulk polaritons, respectively (note: such a definition is common in the plasma physics [43]).

In order to elucidate the dispersion features of hybrid surface polaritons, the initial problem is decomposed into two particular solutions with respect to the vector $\vec{H}$ (EH modes) and vector $\vec{E}$ (HE modes) [10, 42]. In this way, the dispersion equation for surface polaritons is derived in the form:

$$\begin{aligned}
&\kappa_0^2 \tilde{g}_{xx} g_0^{-1} \left[\left(\kappa_1^2 + \kappa_1\kappa_2 + \kappa_2^2 - \varkappa_z^2\right) + \varkappa_y^2 \varsigma_{xz} \tilde{g}_{xz} \left(\varsigma_{yy} \tilde{g}_{xx}\right)^{-1}\right] \\
&\quad + \kappa_0(\kappa_1 + \kappa_2)\left[\kappa_1\kappa_2 + \varkappa_y^2 \tilde{g}_{xx} g_v \left(g_0 \varsigma_{yy}\right)^{-1}\right] \\
&\quad + \tilde{g}_{xz} \varsigma_{xz}^{-1} \left[\left(\varkappa_z^4 - \varkappa_z^2(\kappa_1 + \kappa_2) + \kappa_1^2\kappa_2^2\right) + \varkappa_y^2\left(\varkappa_z^2 + \kappa_1\kappa_2\right)\varsigma_{xz} \tilde{g}_{zz} \left(\varsigma_{yy} \tilde{g}_{xz}\right)^{-1}\right] = 0,
\end{aligned} \tag{36}$$

where $\varkappa_\nu^2 = k_x^2 - k_0^2 \varsigma_{\nu\nu}$ and two distinct substitutions $\varepsilon_{\nu\nu'} \to \tilde{g}_{\nu\nu'}$, $\varepsilon_0 \to g_0$, $\varepsilon_v \to g_v$ and $\varepsilon_{\nu\nu'} \to \tilde{g}_{\nu\nu'}$, $\mu_0 \to g_0$, $\mu_v \to g_v$ correspond to the problem resolving with respect to the vector $\vec{E}$ and vector $\vec{H}$, respectively; ε_v and μ_v are the same shown in Eqs. (34) and (35).

For two particular cases of the gyroelectric and gyromagnetic superlattices, dispersion relation (36) coincides with Eq. (23) of Ref. [10] and Eq. (21) of Ref. [13], respectively, which verifies the obtained solution.

Complete sets of dispersion curves calculated from the solution of Eqs. (34) and (35) that outline the passbands of both ordinary (blue curves) and extraordinary (red curves) bulk polaritons as functions of the filling factor δ_m are presented in **Figure 6a** and **b**. Moreover, in order to discuss the observed crossing and anti-crossing effects more clearly, dispersion curves of both ordinary and extraordinary bulk polaritons are plotted in the $k_0 - k_x$ plane at the particular values of filling factor δ_m as shown in **Figure 6c–f**.

From **Figure 6a** one can conclude that there are two isolated areas of existence of the ordinary bulk polaritons. The upper passband starts at the frequency where $\varepsilon_{yy} = 0$, while the bottom passband is bounded above by the asymptotic line where $\varepsilon_{yy} \to \infty$. Remarkably, the anti-

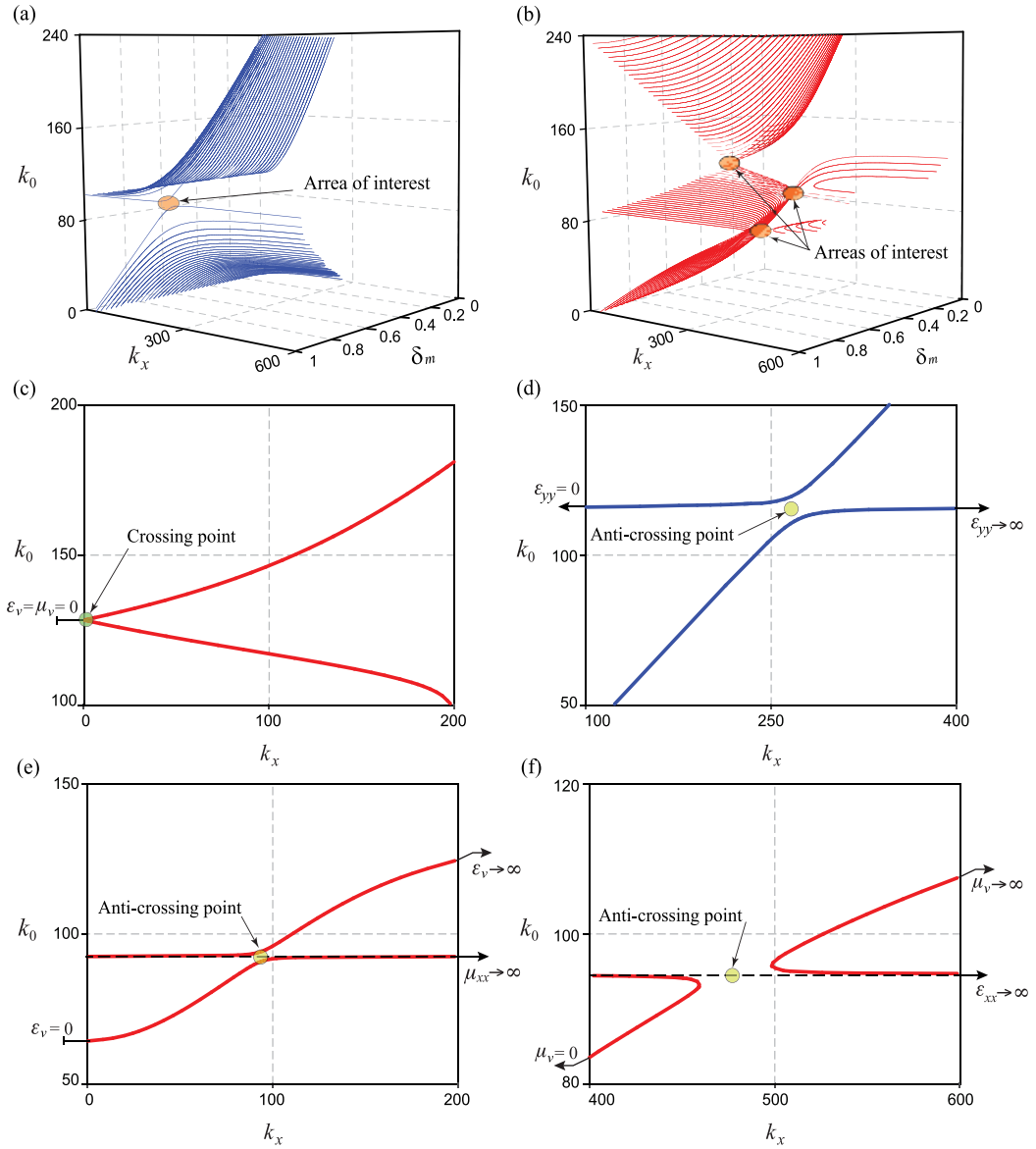

Figure 6. Complete sets of dispersion curves of (a) ordinary (blue curves) and (b) extraordinary (red curves) bulk polaritons for different filling factor δ_m for the structure being in the polar geometry. Manifestation of (c) crossing and (d–f) anti-crossing effects in dispersion curves of bulk polaritons at the particular value of filling factor δ_m, (c) $\delta_m = 0.267$, (d) $\delta_m = 0.99$, (e) $\delta_m = 0.05$, and (f) $\delta_m = 0.99$. All structure constitutive parameters are shown in **Figure 2**.

crossing effect ($\mathbb{H} < 0$) between dispersion curves which restrict upper and bottom passbands of ordinary bulk polaritons can be observed in the composite structure with a predominant impact of the magnetic subsystem (i.e., $\delta_m \gg \delta_s$) as presented in **Figure 6a** and **d**. Coupled modes exhibit an intermediate interaction for which an appearance of the flattened branches in

http://dx.doi.org/10.5772/intechopen.71837

dispersion curves is peculiar (see, for instance, **Figure 3b**). Besides, condition (27) is met, so these waves are codirectional forward in the area nearly the critical point.

As shown in **Figure 6b**, there are two separated areas of existence of extraordinary bulk polaritons for each particular filling factor δ_m. Moreover, there are two possible combinations of conditions for their passbands, which depend strictly on the value of filling factor δ_m [42]. Therefore, the particular critical filling factor is denoted here as δ_c at which $\varepsilon_v = \mu_v = 0$ at $k_x = 0$, and it is considered as a separation point between these two combinations. Thus, the overall range of values δ_m can be separated onto two subranges $0 \le \delta_m < \delta_c$ and $\delta_c < \delta_m \le 1$, respectively.

The value of the critical filling factor δ_c depends on the constitutive parameters of magnetic and semiconductor layers, and for the structure under study, it is $\delta_c = 0.267$. Such critical state in the effective parameters of the superlattice leads to the absence of the forbidden band between the upper and bottom passbands as shown in **Figure 6c**. Remarkably, these dispersion branches appear to be coupled exactly at the frequency where $\varepsilon_v = \mu_v = 0$, i.e., the crossing effect ($\mathbb{H} = 0$) is found to be at $k_x \to 0$. Besides, such coupled waves are contradirectional, and they are described by condition (29).

At the same time, for all present values of filling factor δ_m from the first subrange $0 \le \delta_m < \delta_c$, the lower limits of both the upper and bottom passbands are restricted by the lines at which $\varepsilon_v = 0$, as well as the bottom passband is bounded above by the asymptotic line where $\varepsilon_v \to \infty$. The upper passband is outlined by the set of following conditions [40]: $\varepsilon_v > 0$, $\mu_v > 0$, $\varepsilon_{xz}\mu_{xz}/\varepsilon_{xx}\mu_{xx} < 1$. The bottom passband exists when the set of following conditions holds [42]: $\varepsilon_v > 0$, $\mu_v < 0$ and $\varepsilon_{xz}\mu_{xz}/\varepsilon_{xx}\mu_{xx} > 1$ or $\varepsilon_v > 0$, $\mu_v > 0$ and $\varepsilon_{xz}\mu_{xz}/\varepsilon_{xx}\mu_{xx} < 1$.

For all other values of filling factor δ_m (i.e., $\delta_c < \delta_m \le 1$), the conditions for the upper passband are the same (i.e., $\varepsilon_v > 0$, $\mu_v > 0$, $\varepsilon_{xz}\mu_{xz}/\varepsilon_{xx}\mu_{xx} < 1$), whereas its lower limit is at the line where $\mu_v = 0$. The bottom passband exists when either the set of conditions $\varepsilon_v < 0$, $\mu_v > 0$ and $\varepsilon_{xz}\mu_{xz}/\varepsilon_{xx}\mu_{xx} > 1$ or $\varepsilon_v > 0$, $\mu_v > 0$ and $\varepsilon_{xz}\mu_{xz}/\varepsilon_{xx}\mu_{xx} < 1$ is satisfied. For this band, the lower and upper limits are restricted by the lines at which $\mu_v = 0$ and $\mu_v \to \infty$, respectively.

From **Figure 6a** and **b**, one can conclude that the upper passband possesses typical behaviors in the $k_0 - k_x$ plane, whereas the width and position of the bottom passbands are defined by the corresponding resonant frequencies of effective bulk permeability μ_v and effective bulk permittivity ε_v. In fact, these constitutive parameters are multipliers of the numerator of Eq. (35), whereas the denominator of this equation originates a singularity at the asymptotic line where $1 - \varepsilon_{xz}\mu_{xz}/\varepsilon_{xx}\mu_{xx} \to \infty$. This asymptotic line splits the bottom passbands onto two separated sub-passbands which corresponds to the structures with a predominant impact of semiconductor and magnetic subsystems, respectively (**Figure 6e** and **f**). Note, the intermediate interaction with forming flattened region in dispersion curves between bulk modes from these two sub-bands is observed nearly the Morse critical points ($\mathbb{H} < 0$). Such coupled waves are contradirectional since condition (29) is met.

In the Faraday geometry ($\vec{M} \| z$, $\vec{M} \| \vec{k}$), the superlattice is characterized by the biaxial anisotropy, for which, as already mentioned, the first anisotropy axis is associated with the structure

periodicity (so it is directed along the y-axis), while the second anisotropy axis is a result of the external static magnetic field influence (so it is directed along the z-axis). For this geometry, the bulk polaritons in the structure under study appear as right-handed and left-handed elliptically polarized waves [10, 12, 44], and their passbands are outlined by curves governed by the following dispersion law [44]:

$$\varkappa_x^2\varkappa_y^2 - k_0^4\varsigma_{xy}\varsigma_{yx} = 0, \tag{37}$$

where $\varkappa_\nu^2 = k_z^2 - k_0^2\varsigma_{\nu\nu}$.

The surface polaritons are hybrid EH and HE waves, and their dispersion relation can be written in the form [44]:

$$\begin{gathered}\left(\kappa_2 + \kappa_0\tilde{g}_{zz}\right)\left(\kappa_2^2\varsigma_{yy} - \varkappa_y^2\varsigma_{zz}\right)\left\{\kappa_1\psi\left(\kappa_0^2 - k_z^2\right) + \kappa_0\left[\kappa_1^2\tilde{g}_{xy}\varsigma_{yy} - \varsigma_{zz}\left(k_0^2\rho + k_z^2\tilde{g}_{xy}\right)\right]\right\} \\ -\left(\kappa_1 + \kappa_0\tilde{g}_{zz}\right)\left(\kappa_1^2\varsigma_{yy} - \varkappa_y^2\varsigma_{zz}\right)\left\{\kappa_2\psi\left(\kappa_0^2 - k_z^2\right) + \kappa_0\left[\kappa_2^2\tilde{g}_{xy}\varsigma_{yy} - \varsigma_{zz}\left(k_0^2\rho + k_z^2\tilde{g}_{xy}\right)\right]\right\} = 0.\end{gathered} \tag{38}$$

In Eq. (38), two distinct substitutions $\varepsilon_{vv'} \to \tilde{g}_{vv'}$, $\varepsilon_v \to g_v$ and $\mu_{vv'} \to \tilde{g}_{vv'}$, $\mu_v \to g_v$ correspond to the problem resolving with respect to the vector $\vec{E}$ and vector $\vec{H}$, respectively; $\varepsilon_v = \varepsilon_{xx} + \varepsilon_{xy}^2/\varepsilon_{yy}$, $\mu_v = \mu_{xx} + \mu_{xy}^2/\mu_{yy}$, $\psi = g_v\tilde{g}_{yy}\varsigma_{yx}$; $\rho = \tilde{g}_{yy}\varsigma_{yx} - \tilde{g}_{xy}\varsigma_{yy}$; and the constant $g_0 = 1$ is omitted.

For the semiconductor superlattice, the dispersion Eq. (38) agrees with Eq. (38) of Ref. [10], while in the case of magnetic superlattice, it coincides with Eq. (13) of Ref. [12], which verifies the obtained solution.

Complete sets of dispersion curves that outline the bands of existence of the bulk polaritons (see Eq. (37)) as functions of filling factor δ_m are presented in **Figure 7a** and **b** for right-handed (blue curves) and left-handed (red curves) elliptical polarizations. From these figures, one can conclude that there is a pair of corresponding sets of dispersion curves separated by a forbidden band for the bulk polaritons of each polarization. The dispersion curves of the right-handed elliptically polarized bulk waves demonstrate quite trivial behaviors, and they completely inherit characteristics of the right-handed circularly polarized waves of the corresponding reference semiconductor or magnetic medium (see, for instance [44]). Contrariwise, the dispersion features of the left-handed elliptically polarized waves are much more complicated being strongly dependent on filling factor δ_m and resonant frequencies of constitutive parameters of both semiconductor and magnetic underlying materials. Therefore, in what follows we are interested only in the consideration of dispersion features of the bulk polaritons having the left-handed polarization.

One can conclude that the dispersion characteristics of the left-handed elliptically polarized bulk waves of the given gyroelectromagnetic structure are different from those ones of both convenient gyroelectric and gyromagnetic media. Indeed, in contrast to the characteristics of the left-handed circularly polarized waves of the corresponding reference medium whose passband has no discontinuity, the passband of the left-handed elliptically polarized bulk

http://dx.doi.org/10.5772/intechopen.71837

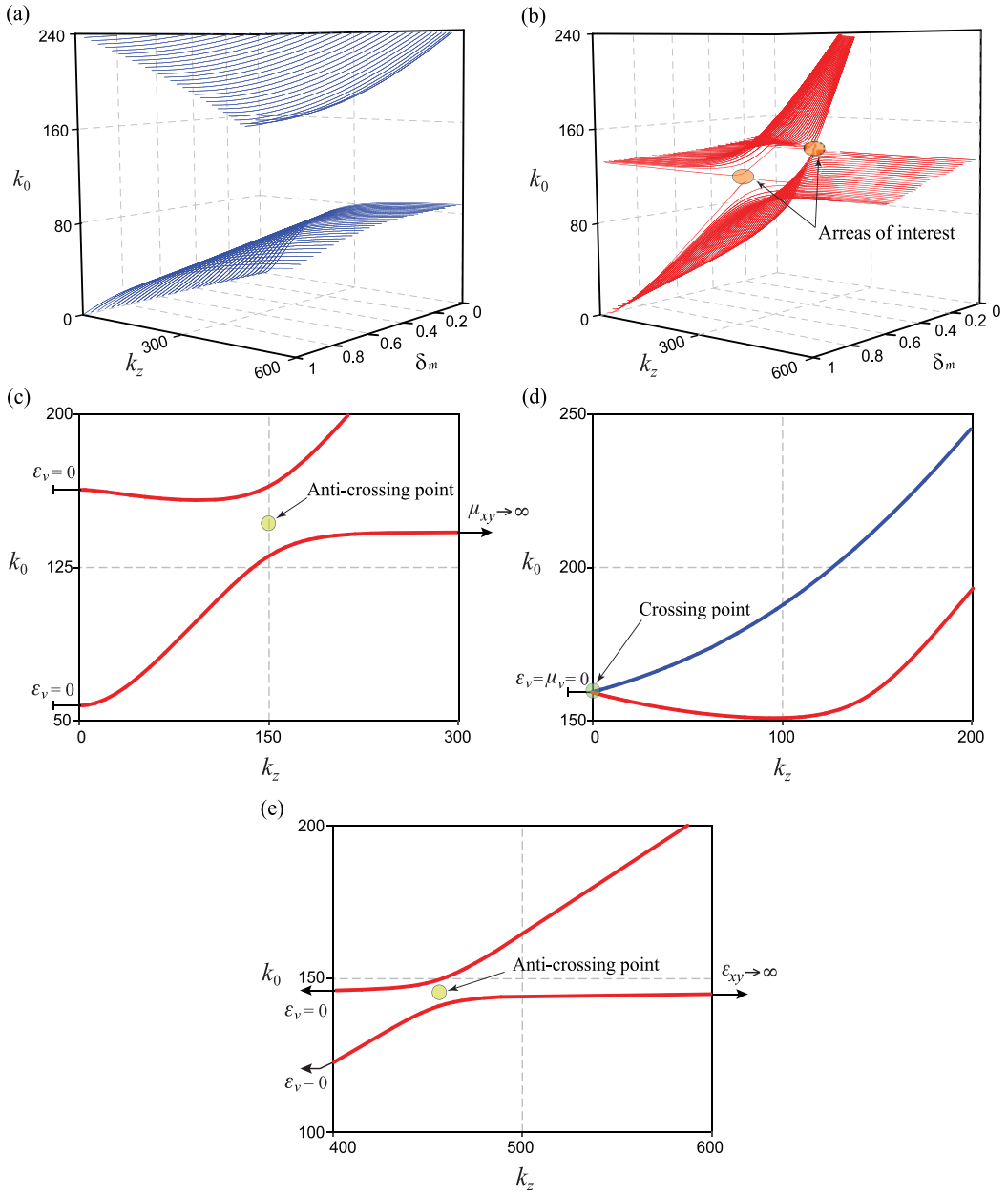

Figure 7. (a, b) Complete sets of dispersion curves of both right-handed (blue curves) and left-handed (red curves) elliptically polarized bulk polaritons for different filling factor δ_m for the structure being in the Faraday geometry. Manifestation of (c, e) anti-crossing and (d) crossing effects in dispersion curves of bulk polaritons at the particular value of filling factor δ_m; (c) $\delta_m = 0.15$; (d) $\delta_m = 0.1$; and (e) $\delta_m = 0.95$. All structure constitutive parameters are shown in **Figure 2**.

polaritons of the superlattice is separated into two distinct areas. This separation appears nearly the frequency at which the resonances of the functions ε_{xy} and μ_{xy} occur for the composite structures with predominant impact of the magnetic and semiconductor subsystems,

respectively. Also, we should note that the exchange by the critical conditions for the asymptotic lines (at which $k_z \to \infty$) between the bottom passbands of left-handed and right-handed elliptically polarized bulk polaritons appears at the particular frequency where ε_{xy} and μ_{xy} simultaneously tend to infinity.

The dispersion curves of bulk waves, which have left-handed polarization, demonstrate significant variation of their slope having subsequent branches with normal and anomalous dispersion that possess approaching at some points (extreme states) as depicted in **Figure 7c** and **e**. The features of these dispersion curves in the vicinity of the critical points are different for the composite structure which has predominant impact either semiconductor (i.e., $\delta_s \gg \delta_m$) or magnetic (i.e., $\delta_m \gg \delta_s$) subsystem. The corresponding modes are contradirectional (i.e., condition (29) is met), and they demonstrate strong interaction nearly the Morse critical point (the anti-crossing effect with $\mathbb{H} < 0$) in the case when $\delta_s \gg \delta_m$. The modes acquire an intermediate interaction in the superlattice with predominant impact of the magnetic subsystem as depicted in **Figure 7e**.

Moreover, a particular extreme state in dispersion curves is found out where the upper branches of the left-handed and right-handed elliptically polarized bulk polaritons merge with each other (see **Figure 6d**) and crossing point ($\mathbb{H} = 0$) occurs at $k_z \to 0$. Likewise to the polar geometry, such extreme state corresponds to the particular superlattice configuration where $\varepsilon_v = \mu_v = 0$ at $k_z = 0$. So, the interacting waves are degenerated at this point and possess the contradirectional propagation.

We should note that in [37] some unusual and counterintuitive consequences of such behaviors of the dispersion curves (e.g., backward wave propagation, reversed Doppler shift, reversed Cherenkov radiation, atypical singularities in the density of states, etc.) for the TE and TM modes of an axially uniform waveguide are discussed, and it is emphasized that these effects are of considerable significance for practical applications.

Finally, in order to obtain the dispersion curves $k_0(k)$ of surface polaritons in both the polar and Faraday configurations, characteristic Eqs. (36) and (38) are solved numerically [42, 44]. Here, as previously, the problem is decomposed into two particular solutions with respect to the vector $\vec{H}$ (EH waves) and vector $\vec{E}$ (HE waves) [10, 12]. Note, as evident from Eqs. (36) and (38), k_x and k_z appear only in even powers, so the dispersion curves of the surface waves appear to be reciprocal.

For both initial problem considerations, dispersion Eqs. (36) and (38) have four roots from which two physically correct ones (denoted here as κ_1 and κ_2) are selected [10] ensuring they correspond to the attenuating waves. In papers [10] and [12], it was noted that depending upon the position in the $k_0 - k_w$ plane, in the non-dissipative system, the following combinations between two roots κ_1 and κ_2 may arise: (i) both roots are real and positive (bona fide surface modes); (ii) one root is real and the other is pure imaginary or vice versa (pseudosurface modes); (iii) both roots are complex in which case they are conjugate (generalized surface modes); and (iv) both roots are pure imaginary (the propagation is forbidden). In our study we consider only bona fide surface mode. Nevertheless, we should note that in both

http://dx.doi.org/10.5772/intechopen.71837

the polar and Faraday geometries, pseudosurface waves (which attenuate only on one side of the surface) can also be supported [10, 45].

Among all possible appearance of dispersion curves of the surface polaritons, we are only interested in those ones which manifest the crossing or anti-crossing effect. The search of their existence implies solving an optimization problem, where for the crossing effect the degeneracy point should be found. For the anti-crossing effect, the critical points are defined from calculation of the first $\mathfrak{D}'(k, k_0)$ and second $\mathfrak{D}''(k, k_0)$ partial derivatives of Eq. (36) or (38) with respect to k and k_0 for both EH and HE modes. During the solution of this problem, the period and constitutive parameters of the underlying materials of the superlattice are fixed, and the search for the effect manifestation is realized by altering the filling factors δ_m and δ_s within the period. The found crossing points are depicted in **Figure 8a** and **b** by green circles. We should note that in both configurations, the degeneracy points for EH (red line) and HE (blue line) surface polaritons can be obtained only for the case of composite structure with a predominant impact of the semiconductor subsystem. In particular, this state is found out to be at the values of filling factor $\delta_m = 0.27$ and $\delta_m = 0.15$ for the polar and Faraday configurations, respectively. Remarkable, in the Faraday geometry, both dispersion curves possess an anomalous dispersion line, namely, they start on the light line and fall just to the right of the light line, and then they flatten out and approach an asymptotic limit for large values of k. Contrariwise to the Faraday geometry, in the polar geometry, both dispersion curves demonstrate normal dispersion.

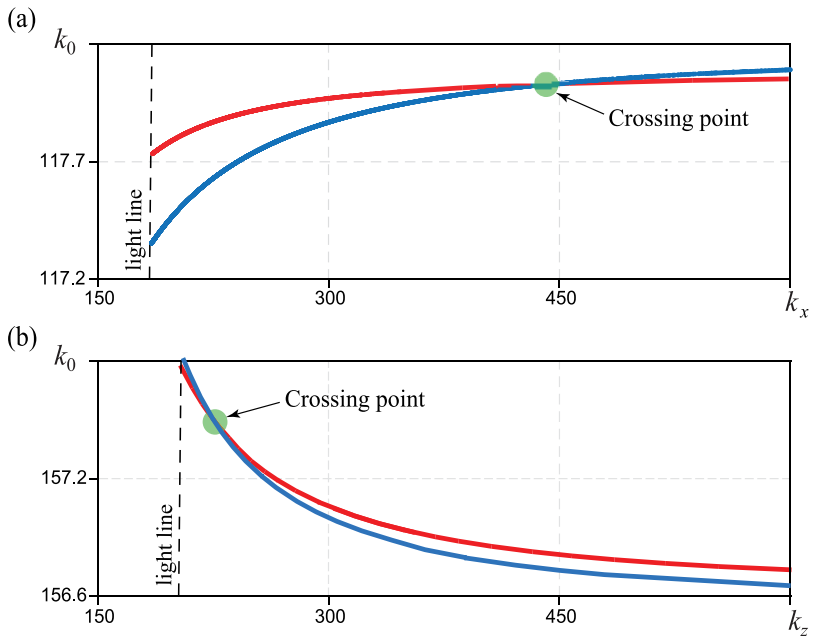

Figure 8. Manifestation of the crossing effect in dispersion curves of hybrid EH (red line) and HE (blue line) surface polaritons; (a) polar configuration ($\delta_m = 0.27$) and (b) Faraday configuration ($\delta_m = 0.15$). All structure constitutive parameters are shown in **Figure 2**.

6. Conclusions

To conclude, in this chapter, we have studied dispersion features of both bulk and surface polaritons in a magnetic-semiconductor superlattice influenced by an external static magnetic field. The investigation was carried out under an assumption that all characteristic dimensions of the given superlattice satisfy the long-wavelength limit; thus, the homogenization procedures from the effective medium theory was involved, and the superlattice was represented as a gyroelectromagnetic uniform medium characterized by the tensors of effective permeability and effective permittivity.

The general theory of polaritons in the gyroelectromagnetic medium whose permittivity and permeability simultaneously are tensor quantities was developed. Three particular configurations of the magnetization, namely, the Voigt, polar, and Faraday geometries, were discussed in detail.

The crossing and anti-crossing effects in the dispersion curves of both surface and bulk polaritons have been identified and investigated with an assistance of the analytical theory about the Morse critical points.

We argue that the discussed dispersion features of polaritons identified in the magnetic-semiconductor superlattice under study have a fundamental nature and are common to different types of waves and waveguide systems.

Author details

Vladimir R. Tuz[1,2], Illia V. Fedorin[3] and Volodymyr I. Fesenko[1,2]*

*Address all correspondence to: volodymyr.i.fesenko@gmail.com

1 International Center of Future Science, State Key Laboratory on Integrated Optoelectronics, College of Electronic Science and Engineering, Jilin University, China

2 Institute of Radio Astronomy of National Academy of Sciences of Ukraine, Ukraine

3 National Technical University 'Kharkiv Polytechnical Institute', Ukraine

References

[1] Agranovich VM, Ginzburg V. Crystal optics with spatial dispersion, and excitons. Berlin: Springer. 1984;**XI**:447. DOI: 10.1007/978-3-662-02406-5

[2] Ozbay E. Plasmonics: Merging photonics and electronics at nanoscale dimensions. Science. 2006;**311**(5758):189-193. DOI: 10.1126/science.1114849

[3] Armelles G, Cebollada A, Garcia-Martin A, Ujue Gonzalez M. Magnetoplasmonics: Combining magnetic and plasmonic functionalities. Advanced Optical Materials. 2013;**1**(1): 10-35. DOI: 10.1002/adom.201200011

[4] Anker JN, Hall WP, Lyandres O, Shah NC, Zhao J, Van Duyne RP. Biosensing with plasmonic nanosensors. Nature Materials. 2008;**7**:442-453. DOI: 10.1038/nmat2162

[5] Jun YC. Electrically-driven active plasmonic devices. In: Ki YK, editor. Plasmonics - Principles and Applications. InTech: Rijeka; 2012. pp. 383-400. DOI: 10.5772/50756

[6] Dicken MJ, Sweatlock LA, Pacific D, Lezec HJ, Bhattacharya K, Atwater HA. Electrooptic modulation in thin film barium titanate plasmonic interferometers. Nano Letters. 2008; **8**(11):4048-4052. DOI: 10.1021/nl802981q

[7] Min C, Wang P, Jiao X, Deng Y, Ming H. Beam manipulating by metallic nano-optic lens containing nonlinear media. Optics Express. 2007;**15**(15):9541-9546. DOI: 10.1364/OE.15.009541

[8] Hu B, Zhang Y, Wang QJ. Surface magneto plasmons and their applications in the infrared frequencies. Nanophotonics. 2015;**4**(1):383-396. DOI: 10.1515/nanoph-2014-002

[9] Kaganov MI, Pustyl'nik NB, Shalaeva TI. Magnons, magnetic polaritons, magnetostatic waves. Physics-Uspekhi. 1997;**40**(2):181-224. DOI: 10.1070/PU1997v040n02ABEH000194

[10] Wallis RF, Brion JJ, Burstein E, Hartstein A. Theory of surface polaritons in anisotropic dielectric media with application to surface magnetoplasmons in semiconductors. Physical Review B. 1974;**9**(8):3424-3343. DOI: 10.1103/PhysRevB.9.3424

[11] Camley RE, Mills DL. Surface polaritons on uniaxial antiferromagnets. Physical Review B. 1982;**26**(3):1280-1287. DOI: 10.1103/PhysRevB.26.1280

[12] Abraha K, Smith SRP, Tilley DR. Surface polaritons and attenuated total reflection spectra of layered antiferromagnets in the Faraday configuration. Journal of Physics: Condensed Matter. 1995;**7**(32):6423-6436. DOI: 10.1088/0953-8984/7/32/008

[13] Elmzughi FG, Constantinou NC, Tilley DR. Theory of electromagnetic modes of a magnetic superlattice in a transverse magnetic field: An effective-medium approach. Physical Review B. 1995;**51**(17):11515-11520. DOI: 10.1103/PhysRevB.51.11515

[14] Kushwaha MS. Plasmons and magnetoplasmons in semiconductor heterostructures. Surface Science Reports. 2001;**41**(1):1-416. DOI: 10.1016/S0167-5729(00)00007-8

[15] Abraha K, Tilley DR. The theory of far-infrared optics of layered antiferromagnets. Journal of Physics: Condensed Matter. 1995;**7**(14):2717

[16] Askerbeyli RT (Tagiyeva). The influence of external magnetic field on the spectra of magnetic polaritons and magnetostatic waves. Journal of Superconductivity and Novel Magnetism. 2016;**30**(4):1115-1122. DOI: 10.1007/s10948-016-3869-4

[17] Datta S, Furdyna JK, Gunshor RL. Diluted magnetic semiconductor superlattices and heterostructures. Superlattices and Microstructures. 1985;**1**(4):327-334. DOI: 10.1016/0749-6036(85)90094-1

[18] Munekata H, Zaslavsky A, Fumagalli P, Gambino RJ. Preparation of (In,Mn)As/(Ga,Al)Sb magnetic semiconductor heterostructures and their ferromagnetic characteristics. Applied Physics Letters. 1993;**63**(21):2929-2931. DOI: 10.1063/1.110276

[19] Koshihara S, Oiwa A, Hirasawa M, Katsumoto S, Iye Y, Urano C, et al. Ferromagnetic order induced by photogenerated carriers in magnetic III-V semiconductor heterostructures of (In, Mn)As/GaSb. Physical Review Letters. 1997;**78**(24):4617-4620. DOI: 10.1103/PhysRevLett.78.4617

[20] Ta JX, Song YL, Wang XZ. Magneto-phonon polaritons in two-dimension antiferromagnetic/ion-crystalic photonic crystals. Photonics and Nanostructures: Fundamentals and Applications. 2012;**10**(1):1-8. DOI: 10.1016/j.photonics.2011.05.007

[21] Jungwirth T, Sinova J, Masek J, Kucera J, MacDonald AH. Theory of ferromagnetic (III, Mn)V semiconductors. Reviews of Modern Physics. 2006;**78**(3):809-864. DOI: 10.1103/RevModPhys.78.809

[22] Polo JA, Mackay TG, Lakhtakia A. Electromagnetic surface waves. A modern perspective. London: Elsevier; 2013. 293 p

[23] Bass FG, Bulgakov AA. Kinetic and electrodynamic phenomena in classical and quantum semiconductor superlattices. New York: Nova Science. 1997

[24] Agranovich VM. Dielectric permeability and influence of external fields on optical properties of superlattices. Solid State Communications. 1991;**78**(8):747-750. DOI: 10.1016/0038-1098(91)90856-Q

[25] Eliseeva SV, Sementsov DI, Stepanov MM. Dispersion of bulk and surface electromagnetic waves in bigyrotropic finely stratified ferrite-semiconductor medium. Technical Physics. 2008;**53**(10):1319-1326. DOI: 10.1134/S1063784208100101

[26] Tuz VR. Polaritons dispersion in a composite ferrite-semiconductor structure near gyrotropic-nihility state. Journal of Magnetism and Magnetic Materials. 2016;**419**: 559-565. DOI: 10.1016/j.jmmm.2016.06.070

[27] Tuz VR. Gyrotropic-nihility state in a composite ferrite-semiconductor structure. Journal of Optic. 2015;**17**(3). DOI: 035611, 10.1088/2040-8978/17/3/035611

[28] Tuz VR, Fesenko VI. Gaussian beam tunneling through a gyrotropic-nihility finely-stratified structure. In: Shulika OV, Sukhoivanov IA, editors. Contemporary Optoelectronics. Netherlands: Springer; 2016. pp. 99-113. DOI: 10.1007/978-94-017-7315-7

[29] Collin RE. Foundation for Microwave Engineering. New Jersey: Wiley-Interscience; 1992

[30] Rui-Xin Wu, Tianen Zhao, John Q Xiao. Periodic ferrite-semiconductor layered composite with negative index of refraction. Journal of Physics: Condensed Matter. 2007;**19**(2): 026211. DOI: 10.1088/0953-8984/19/2/026211

[31] Shestopalov VP. Morse critical points of dispersion equations. Soviet Physics Doklady. 1990;**35**:905

[32] Shestopalov VP. Morse critical points of dispersion equations of open resonators. Electromagnetics. 1993;**13**:239-253. DOI: 10.1080/02726349308908348

[33] Yakovlev AB, Hanson GW. Analysis of mode coupling on guided-wave structures using Morse critical points. IEEE Transactions on Microwave Theory and Techniques. 1998;**46**(7): 966-974. DOI: 10.1109/22.701450,

[34] Yakovlev AB, Hanson GW. Mode-transformation and mode-continuation regimes on waveguiding structures. IEEE Transactions on Microwave Theory and Techniques. 2000;**48**(1):67-75. DOI: 10.1109/22.817473

[35] Yakovlev AB, Hanson GW. Fundamental wave phenomena on biased-ferrite planar slab waveguides in connection with singularity theory. IEEE Transactions on Microwave Theory and Techniques. 2003;**51**(2):583-587. DOI: 10.1109/TMTT.2002.807809

[36] Gilmore R. Catastrophe Theory for Scientists and Engineers. New York: Wiley; 1981

[37] Ibanescu M, Johnson SG, Roundy D, Luo C, Fink Y, Joannopoulos JD. Anomalous dispersion relations by symmetry breaking in axially uniform waveguides. Physical Review Letters. 2004;**92**(6):063903. DOI: 10.1103/PhysRevLett.92.063903

[38] Ivanov ST. Waves in bounded magnetized plasmas. In: Schluter H, Shivarova A, editors. Advanced Technologies Based on Wave and Beam Generated Plasmas. Netherlands: Springer; 1999. pp. 367-390

[39] Fesenko VI, Fedorin IV, Tuz VR. Dispersion regions overlapping for bulk and surface polaritons in a magnetic-semiconductor superlattice. Optics Letters. 2016;**41**(9):2093-2096. DOI: 10.1364/OL.41.002093

[40] Tarkhanyan RH, Niarchos DG. Effective negative refractive index in ferromagnet-semiconductor superlattices. Optics Express. 2006;**14**(12):5433-5444. DOI: 10.1364/OE.14.005433

[41] Tarkhanyan RH, Niarchos DG. Influence of external magnetic field on magnon-plasmon polaritons in negative-index antiferromagnet-semiconductor superlattices. Journal of Magnetism and Magnetic Materials. 2010;**322**(6):603-608. DOI: 10.1016/j.jmmm.2009.10.023

[42] Tuz VR, Fesenko VI, Fedorin IV, Sun H-B, Han W. Coexistence of bulk and surface polaritons in a magnetic-semiconductor superlattice influenced by a transverse magnetic field. Journal of Applied Physics. 2017;**121**(10):103102. DOI: 10.1063/1.4977956

[43] Ginzburg VL. The Propagation of Electromagnetic Waves in Plasma. London: Gordon and Breach; 1962

[44] Tuz VR, Fesenko VI, Fedorin IV, Sun H-B, Shulga VM. Crossing and anti-crossing effects of polaritons in a magnetic-semiconductor superlattice influenced by an external magnetic field. Superlattices and Microstructures. 2017;**103**:285-294. DOI: 10.1016/j.spmi.2017.01.040

[45] Brion JJ, Wallis RF. Theory of pseudosurface polaritons in semiconductors in magnetic fields. Physical Review B. 1974;**10**(8):3140-3143. DOI: 10.1103/PhysRevB.10.3140

Chapter 7

Video Measurements and Analysis of Surface Gravity Waves in Shallow Water

Charles R. Bostater Jr, Bingyu Yang and
Tyler Rotkiske

Additional information is available at the end of the chapter

http://dx.doi.org/10.5772/intechopen.73042

Abstract

This paper discusses a shallow-water wave height measurement method that uses high definition video cameras to image a water surface wave patch. Wave height time series are extracted from water surface video sequences. Wave features such as the wavelength distribution and energy contained in a wave patch (W/m^2) were obtained by analyzing the extracted wave height time series and expressing the wind-driven wave energy as a wave energy spectrum. A Weibull probability distribution was used as the mathematical form of the energy spectrum. Wave spectra are used as input to a wave patch simulation model that generates simulated wind-driven wave images. The measurement protocol is inexpensive, easy to implement, and useful to calibrate and validate wind-driven wave models. The protocol is used to understand resuspension of bottom muds due to wind waves in shallow waters. Scaled staff gauges made of polyvinyl chloride (PVC) materials are placed in shallow water and imaged at 30 Hz followed by frame based image analysis to extract wave height time series. Wave spectra calculated using the fast Fourier transform (FFT) results in a Weibull probability distribution function (WPDF) energy spectrum. The estimated wave spectrum is used to estimate wave energy in W/m^2 followed by generation of wave patch simulations of the water surface. Simulated wave patches are compared with the sensor-based wave patch video measurements. Sensitivity analysis of coefficients α and β in the model are used to adjust the synthetic wave images to measured wave patch images. The approach allows one to obtain an estimate of the energy (W/m^2) transferred from the local wind field to a water surface gravity wave patch.

Keywords: water surface waves, gravity waves, wind driven waves, wave patches, wave patch energy, remote sensing, staff gauges, video imaging, video analysis, energy spectra, Weibull distributions, synthetic imaging, wind energy

1. Introduction

Differential heating of the earth causes large-scale atmospheric pressure gradients. These gradients and the acceleration due to rotation of the earth result in the major wind fields around the globe. The winds cause friction on the water surface and result in the generation of wind-driven water surface gravity waves. These wind-driven gravity waves are a major source of transfer of energy from the sun and atmosphere to the earth's water system on a global scale as well as in small water regions. Measurements of these wind-driven shallow-water surface gravity wave characteristics such as wave height, period, and direction of propagation are key to understanding the magnitude of energy in a small gravity wave field or "wave patch." These surface wind-driven waves cause orbital motion of water parcels [1]. In water the wind stress or friction causes the downward movement or transport of momentum from the water surface to the water column. The downward transport of momentum causes internal friction in the water in the form of turbulent friction or viscosity, and the associated circular eddy-type motions influence the bottom lutocline within the bottom boundary layer [2, 3]. The resulting shearing forces at the bottom in shallow water cause resuspension of and fluidization of bottom sediments and associated nutrients and/or trace metals. The fluidization can result in fluidized mud, muck, high-bottom water turbidity, and nephelometric wave motions (internal wavelike motions that are observed in acoustic imaging of the bottom water column). Thus, water quality variables are influenced by the surface water wave field driven by surface winds. Bottom orbital or elliptical velocities due to these wind-driven gravity waves in shallow water can be calculated using surface wind-driven gravity wave information, such as significant wave height and wave spectra [3, 4].

Wind-driven gravity waves in water can be measured using numerous techniques and descriptions, including satellite altimeters, video cameras, wave buoys, and many types of wave gauges [5]. Altimeters flown on satellites such as Seasat in 1978, Geosat from 1985 to 1988, ERS-1 and ERS-2 from 1991, TOPEX/Poseidon from 1992, Jason from 2001, and Envisat can provide data for monthly mean maps of wave heights and the variability of wave energy density in time and space [5]. Wave height estimations based on binocular or trinocular imaging also allow acquisition of both spatial and temporal wave information for surface wave patches [6, 7, 14]. Many types of wave gauges including resistance-type, capacitance-type, and wave pressure gauges can also provide data for quantifiable wind-driven gravity wave height estimations [8]. However, there is a need to develop measurement system methods [17, 18] for shallow-water areas since most systems developed to date can only be used in deep waters (>3–5 m).

In this research, a technique or protocol that combines gravity wave staff gauges, HD video cameras [14], and image analyses is used to measure wind-driven gravity waves in shallow-water environments that receive energy from the atmosphere. Wave height time series are extracted from video sequence taken using high-definition (HD) video cameras at a 30 Hz frame rate. Significant wave height, wave spectrum, and wave energy (W m^2) are estimated from the video-based wave height time series.

In this chapter, techniques to describe the protocol are demonstrated for shallow water near the Atlantic Ocean and Space Coast Region of the Banana River estuary and watershed, near Melbourne, Florida. Simulated wave patch synthetic images are then generated using estimated wave spectrum derived from video imagery and compared to the video images.

2. Techniques and methods

2.1. Video imaging and staff gauge system

Staff gauges and HD video cameras (JVC Everio HD cameras) are used to measure the surface wave heights in shallow water (1–2 m) as shown in **Figure 1(a)**. Four staff gauges are mounted in the water by inserting them into the bottom sediment. Staff gauges are constructed from white PVC pipes. Waterproof paper with 0.5 spaced horizontal lines is taped to each gauge pipe.

Images recorded at 1920 × 1080 pixels (30 per second of recording time) obtained from the video sequence yield spatial resolution (using lens zooming) is 0.04 cm/pixel. Each line is either 1 mm (≈2 pixels) or 0.5 mm (≈1 pixel) as shown in **Figure 1(b)**. The HD cameras are mounted on a tripod on the shore or from a fixed platform or mount in the water. The video staff gauges allow one to define a wave patch of ~4.5 × 4.5 m ($W_x = W_y = 4.5$ m).

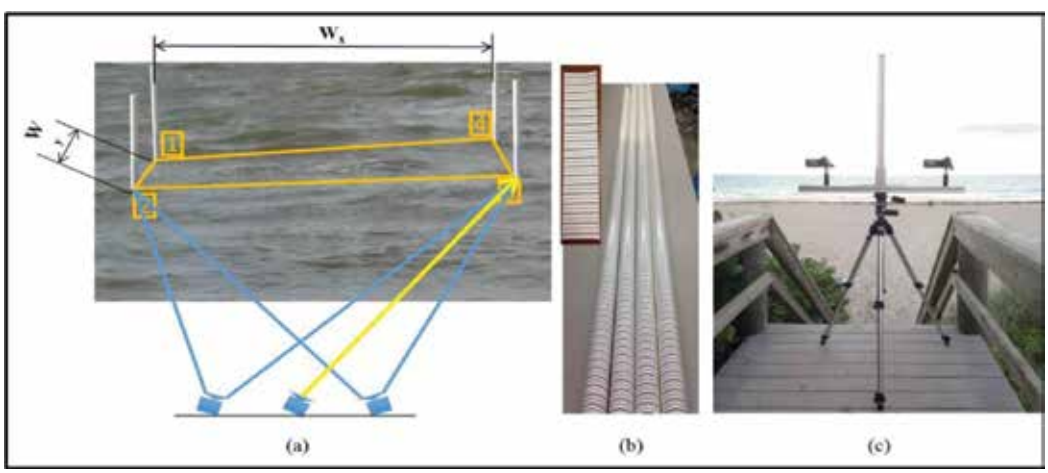

Figure 1. Imaging system deployment and video image of the wave patch (a), staff gauges (b), and example camera deployment platform (c). Target wave patch defined by four staff gauges is 4.5 × 4.5 m (20.25 m^2). Staff gauges were constructed using PVC pipes and striped paper with 0.5 cm line (alternating two colors and thickness) separation. Two video cameras can be used for binocular stereo imaging, and the third camera can be mounted on the vertical bar in the middle or either side in order to conduct a stereo or trinocular imaging of a water patch or zoomed to image staff gauges.

An inverted T-shaped (**Figure 1(c)**) aluminum and steel camera optical mount is used to mount one, two, or three HD cameras. Cameras can be time synchronized, using a known or fixed "digital zoom" mode. During measurement experiments, one camera is focused upon and zoomed (18×) on a staff gauge, and the other two cameras image the entire wave patch and record at 30 Hz or frames per second (fps) (**Figure 2**).

2.2. Image processing

In order to determine the water surface level based on video sequences, three steps are needed as summarized below:

Step 1: Determine the region of interest (ROI)

The water surface level at the staff gauges was clearly observed from the 18× zoomed video frame images. A representative image is shown in **Figure 3(a)**. A ROI was selected to be the area between the top horizontal scale line on the gauge and the bottom margin of the image and was slightly less in width than the actual gauge as defined by the rectangular area in **Figure 3(b)**. A thinner ROI than the actual gauge prevents pixels outside of the staff gauge influencing the results.

Step 2: Average the digital counts within the ROI

Within the ROI, the mean pixel value across each horizontal line is calculated to compress the ROI into a "representative line" shown in **Figure 3(b)**. The average of the three color bands (R, G, B) is calculated in this step as well. The oscillating line in **Figure 3(c)** is the average pixel value of the example frame, and the air-water interface is obvious.

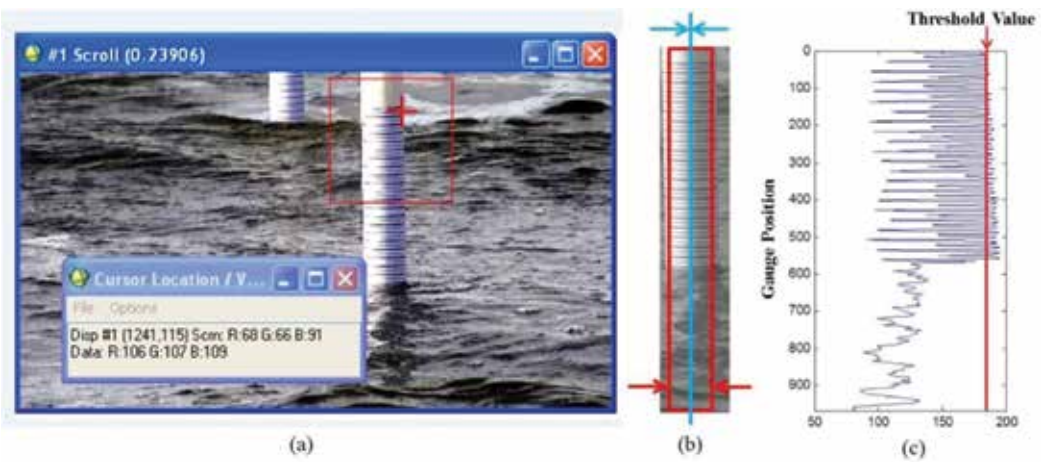

Figure 2. Three steps are used to determine the water surface level from the video. (a) Example of a video frame from the zoomed video (18×). (b) Then, a region of interest (ROI) is defined by a rectangular area, and then a representative line at the center is calculated by averaging the pixel value on each horizontal level. (c) Pixel values along the averaged representative line are shown, and a selected threshold value is selected to locate the interface of water and gauge shown by the solid line.

http://dx.doi.org/10.5772/intechopen.73042

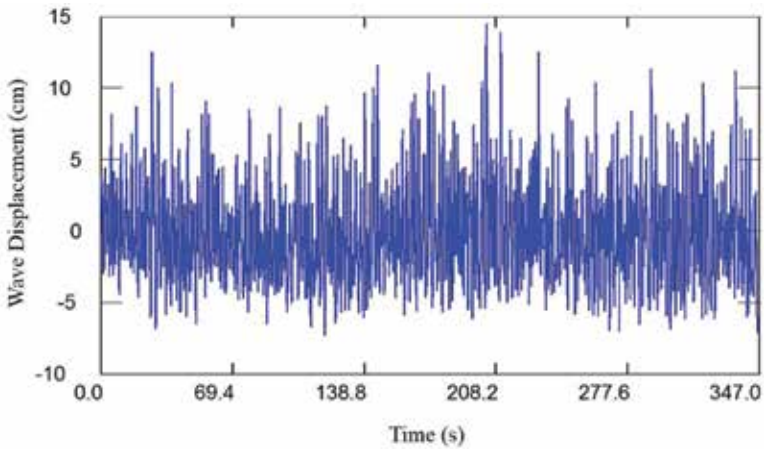

Figure 3. Measured shallow-water surface oscillation series from the video expressed in "wave coordinate." The sequence shown is 347 s with 30 Hz frame rate (10,388 observations). The average water depth during the experiment was 35 cm. The average water surface level during the experiment ranged from 30 cm at the wave troughs and 40 cm at wave crests.

Step 3: Locate the air-water level on the gauge

The shape of the pixel value curve changes dramatically at the interface of water and gauge as shown in **Figure 3(c)**, which is the water surface level. A threshold value is selected in order to automatically locate the interface within each video frame.

The threshold value was determined based on the average of part of the "representative line" (first 500 pixels from the top in the example shown in **Figure 3 (b)**) and it slightly varies from frame to frame. The key is to semiautomatically select a threshold value and apply this value to each frame. The location of the start of values lower than the threshold value is considered as

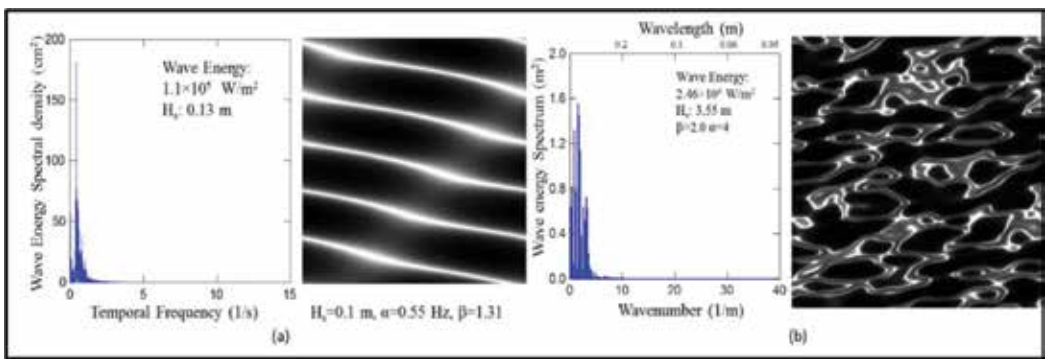

Figure 4. Estimated wave energy spectrum with simulated wave patch (a) and wave energy spectrum with simulated wave patch image using adjusted model coefficients α and β. The peak frequency of the spectrum is 0.39 Hz, and the wave energy in the patch in W/m^2 is 1.1×10^5. The simulated wave patch synthetic images are generated using the estimated wave spectrum from field measurements. The simulated image size is 1024×1024 pixels and represents the 4.5×4.5 m^2 wave patch defined by the staff gauges shown in **Figure 1**. Simulated mean wave height is 7.6 cm, and significant wave height is 0.1 m.

the water surface. **Figure 4** shows the result of 30 Hz time series of the water wave surface oscillations calculated from the example video sequence.

3. Wave spectrum development

A wave energy density spectrum of a wind-driven surface gravity wave patch E can be expressed in units of W/m^2 and is related to the wave height or the variance of the wave displacement, given as $E = \frac{1}{8}\rho g H^2 = \frac{1}{2}\rho g a^2$, where a is the wave displacement and the wave height (H) is twice the wave displacement or $H = 2a$ [1]. Given a measured wave time series, the wave spectrum can be calculated using the fast Fourier transform (FFT) [5]:

$$S(f) = Z_n Z_n^*, \tag{1}$$

where $S(f)$ is the wave spectrum density in the unit of cm^2/Hz, f is temporal frequency in the unit of Hz (1/s), $Z_n = \frac{1}{T}\int_{-T/2}^{T/2} \zeta(t)\exp(i2\pi nft)$ is the Fourier transform of the original signal $\zeta(t)$ (dimensionless), $Z_n^* = \frac{1}{T}\int_{-T/2}^{T/2} \zeta(t)\exp(-i2\pi nft)$ is the conjugate of Z_n (dimensionless), n is the

	β=1.0	β=1.5	β=2.0	β=2.5	β=3.0	β=4.0
α=0.5	0.277862	0.015193	2.68E-05	1.02E-11	2.52E-26	2.52E-26
α=1.0	1.164226	0.416754	0.158876	0.034591	0.002794	5.04E-08
α=2.0	4.244364	1.722385	1.478643	1.175117	1.188344	0.935551
α=4.0	11.88485	4.710576	3.527726	3.322177	2.987826	2.751408
α=8.0	34.78781	12.28227	7.551147	6.673736	5.745111	4.713235
α=10.0	47.07448	17.87447	10.19432	8.754212	7.929079	7.181631

Figure 5. Significant wave height H_s (m) of simulated waves using the wave model (see Eqs. (2) and (3)) parameters α (scale parameter) and β (nondimensional shape parameter) and selected example simulated wave patch synthetic images.

number of the data point in the measured sequence (dimensionless), t is the instant time corresponding to the data point in the unit of second (s), and T is the length of measurement time in the unit of second (s). A two-parameter Weibull distribution function was used as a test model for mathematical expression of the spectrum [2]. The Weibull probability density function (PDF) and cumulative density function (CDF) are given by [9]:

$$\text{PDF} - \text{probability} : (Y) = \left(\frac{\beta}{\alpha^{\beta}}\right) Y^{\beta-1} \exp\left(-\left(\frac{Y}{\alpha}\right)^{\beta}\right) \quad Y > 0, \tag{2}$$

$$\text{CDF} - \text{cumulative} : (Y) = 1 - \exp\left(-\left(\frac{Y}{\alpha}\right)^{\beta}\right) \quad Y > 0, \tag{3}$$

where Y is a variable that follows the Weibull distribution. In this research Y has the unit of 1/s (temporal frequency) or 1/m (wavenumber (spatial frequency); see **Figure 5(a)**), and **Table 1** on x-axis, α = scale parameter has the units of the variable Y, which is 1/s or 1/m, β = non-dimensional shape parameter.

4. Experimental results

4.1. Image-based wave height time series and statistical characteristics

By using the three steps described in Section 2.2, the water surface-level change throughout the video sequence was obtained as shown in **Table 1** and **Figure 4**. Mean wave height of the measured series was 7.9 cm, and significant wave height H_s was 13 cm. The significant wave height H_s is defined as average of the highest one-third of the wave heights [10]. The speed of this wave series extracting process is about two frames per second.

4.2. Wave spectrum, wave energy, and simulation for the Banana River site

The wave spectrum coefficients estimated using the video-based wave series were $\alpha = 0.55$ and $\beta = 1.31$. The calculated wave energy spectrum of the measured wave height time series on temporal frequency domain (Hz) is calculated from Eq. (4):

$$S(\omega) = \left(\frac{\beta}{\alpha^{\beta}}\right) \omega^{\beta-1} \exp\left(-\left(\frac{\omega}{\alpha}\right)^{\beta}\right), \tag{4}$$

where $S(\omega)$ is the wave energy spectral density (m^2/Hz), ω is the temporal frequency (Hz), α = 0.55 is the Weibull scale parameter (Hz), and β = 1.31 is the Weibull shape parameter (dimensionless). The estimated wave spectrum can then be used in the spectral wave patch model [11, 12]. Since the wave simulation program by Bostater et al. [11, 12] was designed to generate a shallow-water gravity wave patch that was independent of time, a dispersion relation was applied to transfer the energy spectrum from temporal frequency domain (Hz) to spatial frequency domain (1/m):

$$\omega(k) = \sqrt{gk\ tanh(kd)}, \tag{5}$$

where $\omega(k)$ is the temporal frequency (Hz), k is the spatial frequency wavenumber (1/m), g is the gravity acceleration (m/s^2), and d is the water depth (m).

The wave energy in the units of W/m^2 can now be calculated using the estimated wave spectrum, based on the area under the spectrum curve [13]:

$$E = \rho g \int S(\omega) d\omega, \tag{6}$$

where E is the wave energy in units of W/m^2 (Joules/s m^2), $S(\omega)$ is the wave energy spectrum in units of m^2, ω is the temporal frequency in units of Hz, $\rho = 1000$ kg/m^3 is the density of the water used in this research, and $g = 9.8$ m/s^2 is the acceleration due to gravity. The discrete approximation of wave energy in this research is calculated by summing the area under the spectral curve:

$$E = \rho g \sum_{0}^{N} S(\omega_n) \Delta\omega_n, \tag{7}$$

where N is the total number of discrete frequencies integral, $S(\omega_n)$ is the magnitude of the energy spectrum at each frequency ωn in units of m^2, and $\Delta\omega_n$ is the discrete frequency interval in units of Hz. A representative shallow-water wind-driven gravity wave can be simulated using the

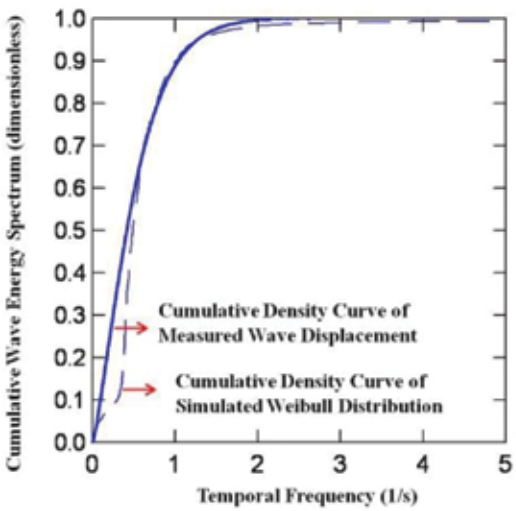

Simulated area in x-y	W_x, W_y	4.5 m² wave patch
Simulated image size	M, N	1024 × 1024 pixels Spatial resolution is 0.004 m/pixel
Gravity acceleration	g	9.8 m/s²
Average water depth	d	0.35 m
Temporal frequency	$\omega(k)$	$\omega(k) = \sqrt{gk\ tanh(kd)}$
Weibull parameters	α, β	$\alpha = 0.55, \beta = 1.31$
Wave energy spectrum	$S(\omega(k))$	$\left(\frac{\beta}{\alpha^\beta}\right)\omega(k)^{\beta-1}\ exp\left(-\left(\frac{\omega(k)}{\alpha}\right)^\beta\right)$

Table 1. (right) Input equations and parameters for running the wave simulation program (Bostater et al. [11, 12]) for simulating the wave patch shown in **Figure 4** and the measured and simulation distributions (left image). Comparison of the calculated Weibull cumulative curve (solid line) and the cumulative curve of the wave energy spectrum extracted from the measured wave displacements with estimated Weibull parameters of $\alpha = 0.55$ (Hz) and $\beta = 1.31$ (dimensionless) as shown in the table.

http://dx.doi.org/10.5772/intechopen.73042

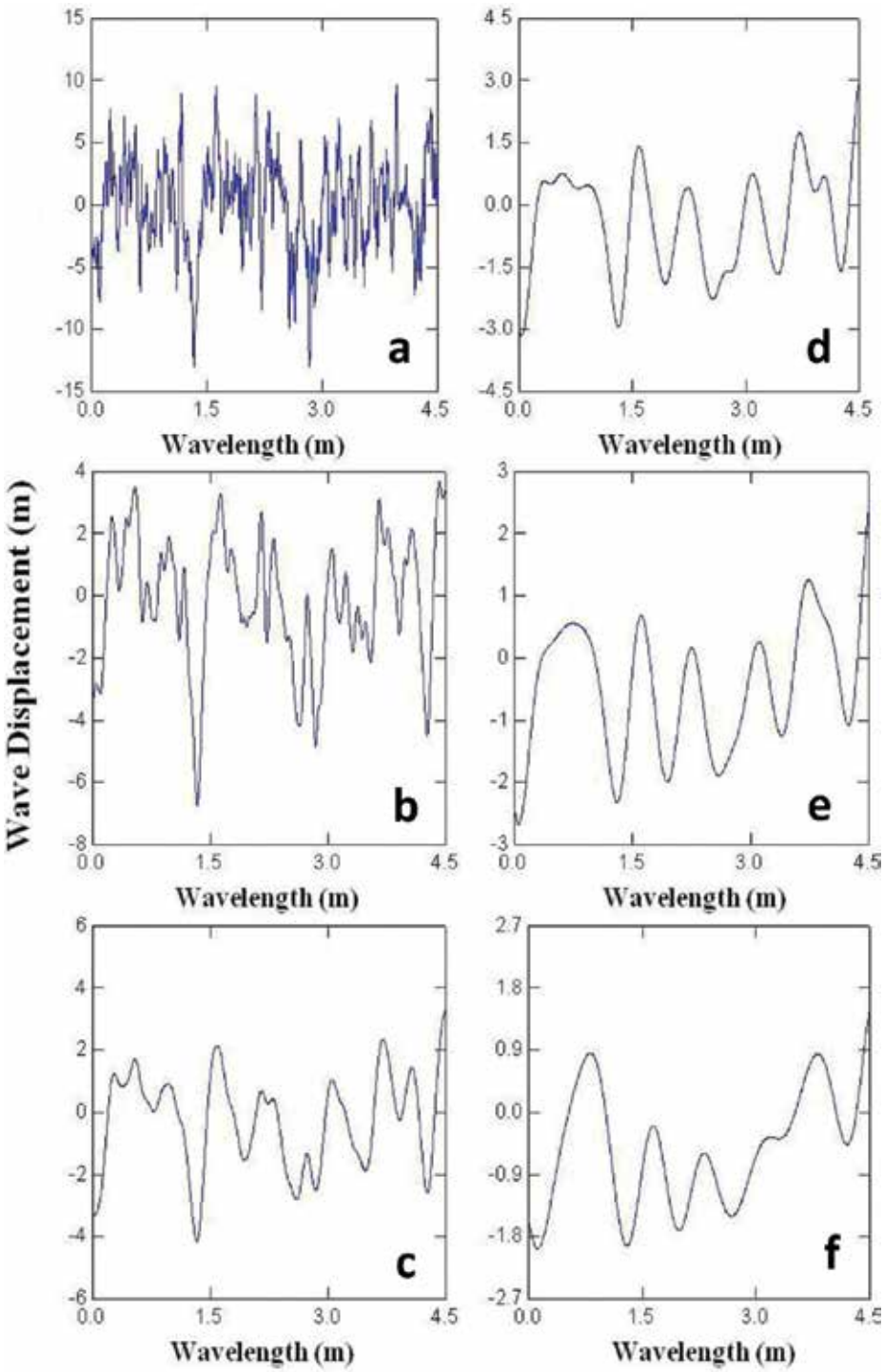

Figure 6. Example shallow-water wave displacement (m) and wavelength (m) sequences (a–f) extracted from synthetic imagery (see **Figure 5**) used to demonstrate the sensitivity of the energy in a simulated wave patch as shown in **Figure 7**. The simulated image results are shown in **Figure 5**.

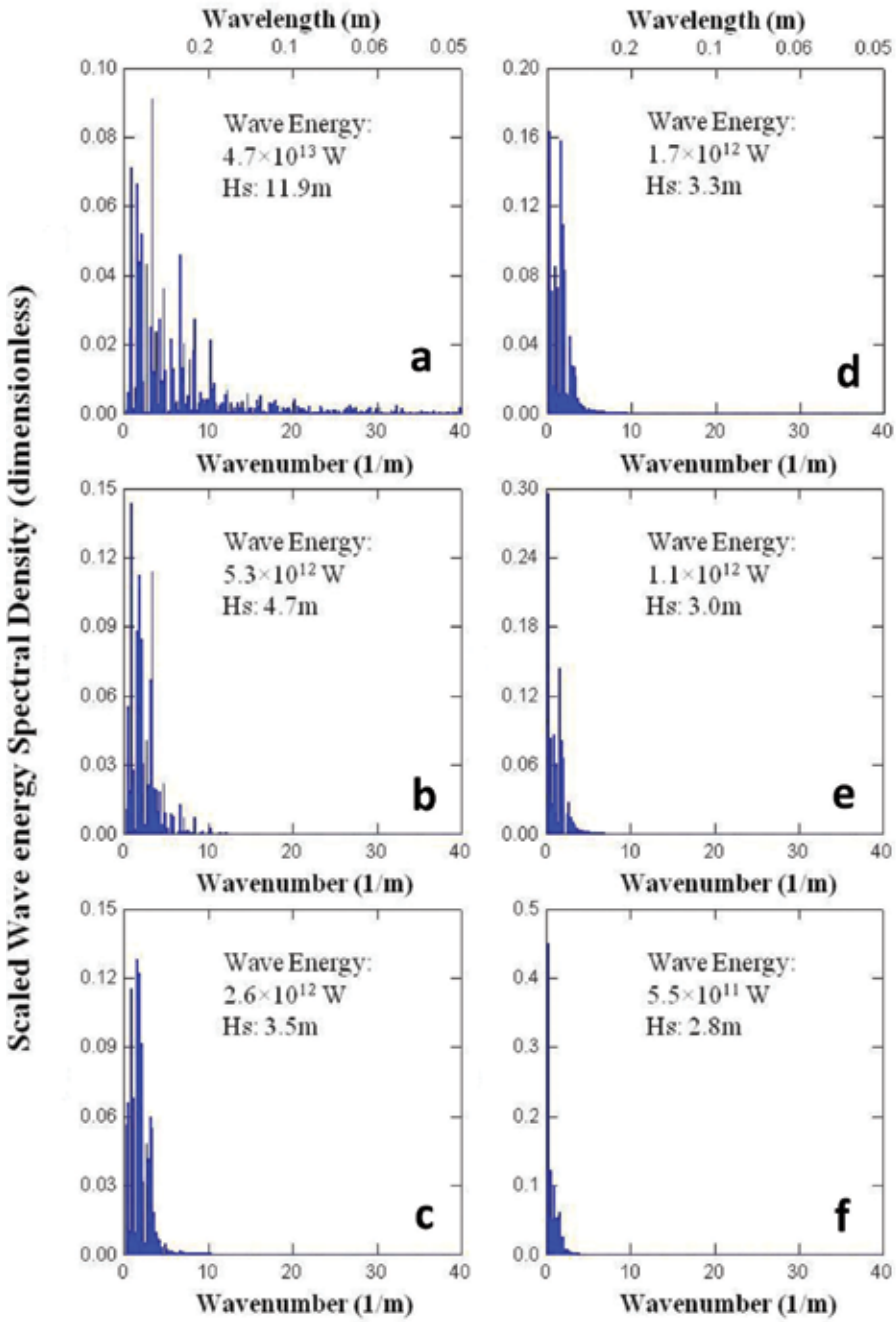

Figure 7. Calculated wave energy in a simulated wave patch for different significant wave heights, wave displacement and wavenumber (spatial frequency) time series (a–f), and synthetic wave patch images shown in **Figure 6**. The representative synthetic mages are shown in **Figure 5**.

estimated wave spectrum from measurements as shown in **Figure 4(a)**. A wave patch simulation model specific for shallow water such as Banana River and Indian River Lagoon was used [8]. The simulated mean wave height is 7.6 cm, and significant wave height is 0.1 m, which is consistent with the video-based measurements. Sensitivity analysis of the simulation model can also be conducted in order to determine the effects of the model coefficients α and β on the simulated wave patches. The results suggest that the model coefficients α and β can affect wave height scale and wave pattern of the simulated wave patches. Therefore, it is reasonable to assume that α and β are related to physical or environmental variables that affect the wave conditions, such as wind speed, wind duration, wind direction, fetch, water depth, bottom slope, etc. When the wave patch model coefficients are adjusted, realistic random water waves are produced as shown in **Figure 4(b)**. The wave energy spectrum (Eq. (4)) can also be introduced or multiplied by a nondimensional scaling coefficient $A = 15$ in this example for sensitivity analysis related to wave patch simulations shown **Figures 4** and **5** (**Table 1**).

A sensitivity analysis of the wave model parameter α (scale parameter) and the β (non-dimensional shape parameter) allows one to clearly see how the water surface wave field would look for different parameter values. The sensitivity simulation results are shown in **Figure 5** with selected wave patch synthetic images for selected model parameters. **Figure 6** shows example wave height displacements, wavenumbers, and significant wave height, and the resulting wave patch energy is simulated wave patches. **Figure 7** shows the associated (a–f) wave energy and significant wave heights obtained from synthetic image model runs. The results demonstrate the utility of making observations, followed by sensitivity analysis and resulting wave patch energy, and associated significant wave heights derived from the synthetic images which are representative measured wind-driven surface gravity wave field patches.

5. Summary

This research developed an imaging methodology to measure wind-driven gravity waves in shallow water using high-definition (HD) video cameras and specially constructed staff gauges. Wave spectrum, wave energy, and significant wave height are estimated from video-based wave height measurement, which can be used to estimate bottom velocity and sediment resuspension. Simulated wave field images are generated using estimated wave spectrum; wave characteristics (significant wave heights) based on the simulation images agree with the in situ video-based measurement protocol and methods described in Section 3 above.

Coefficients α and β in the spectral wave simulation model can affect the wave height and pattern of the simulated wave patches, and they are very likely to be related with some physical and environmental variables. Ongoing research is investigating these variables for these small amplitude water surface waves. The approach developed and described above utilizes the conceptualization shown in **Figure 8**. The energy stored in a surface water gravity wave field drives the sediment resuspension process in the bottom boundary layer and lutocline consisting

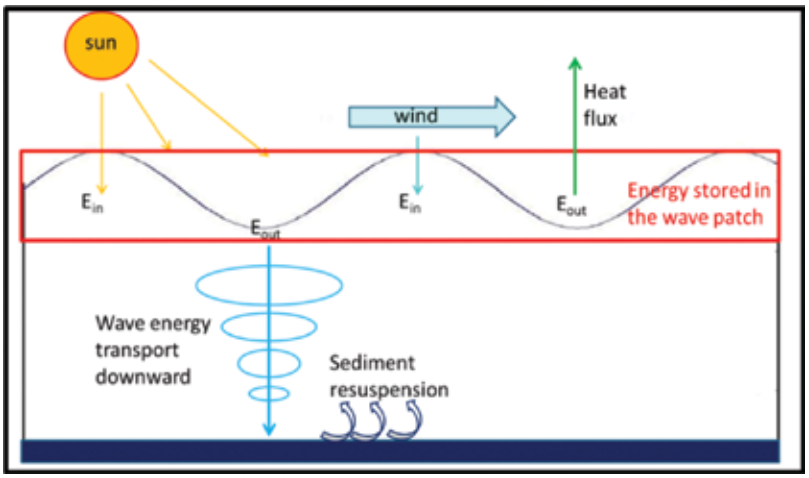

Figure 8. Conceptual model of energy stored in a measured or simulated wave patch and the downward transport of momentum to the bottom boundary layer that can cause resuspension and liquefaction of bottom mud and muck within the lutocline.

of fluid mud and muck. The flowchart shown in **Figure 9** summarizes the protocol and methods described above.

Each time series of water surface displacements is linearly detrended before spectral analysis and calculation of the wind wave energy in the wave field. The mono imaging used in the protocol is the simplest method because water surface elevations can be easily obtained using in situ staff gauges. Algorithms can then be used to calculate wave displacement and wave heights using image processing techniques that analyze each video frame as an instantaneous realization of the water surface elevation or displacement at 0.033 s time intervals. The key for successful mono imaging is the bottom mounted staff gauge used for automatic water surface elevation detection. The staff gauge used in this research was scaled to the appropriate measured wave height field and the gauge and inserted into the bottom sediments.

Simulation of wind-driven water wave patch results shown in **Figure 5** indicates that as α increases, the wave displacement increases and smaller wavelength waves appear on top of the larger waves. The effect of β is just the opposite of α. Increasing β causes decrease in wave displacements with coincident disappearance of smaller waves on top of the larger waves.

The wave energy spectrum graphs (obtained from the synthetic images) shown in **Figures 6** and **7** also provide a visual demonstration of the effect of α and β on wind-driven waves using the Weibull model. Increasing α causes the energy distribution to spread into larger wavenumber in the spatial frequency domain (1/m). This reveals that a simulated wave patch with larger α is consistent with waves with a greater variety of wavelengths. However, increasing β causes the narrowing of the energy distribution to smaller wavenumber (1/m) and suppresses the frequency of larger wavelength waves in a simulated wave patch.

From an energy point of view, wave energy in units of W/m^2 increases with increasing α and decreasing β. The wave energy can be calculated within the simulated wave patch area

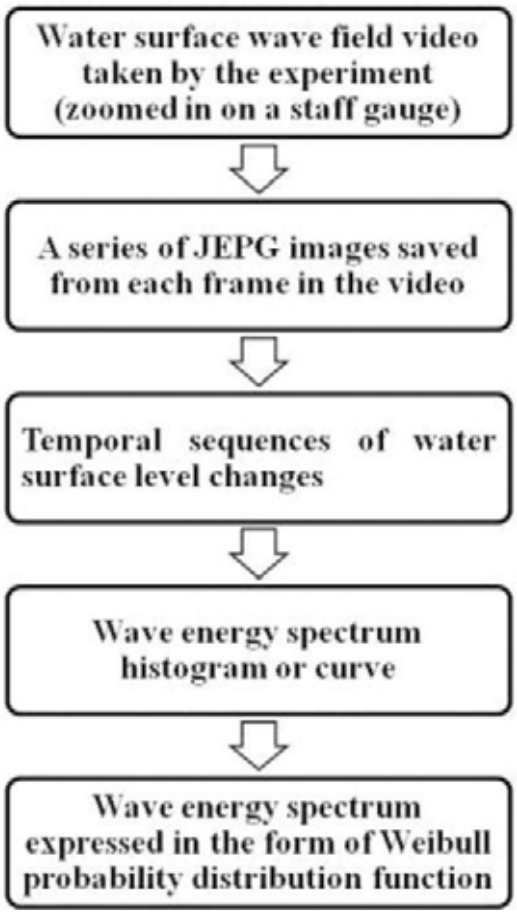

Figure 9. Summary of the general procedures used to extract wind-driven gravity wave energy in a wave patch and resulting wave energy spectrum from measured wind wave videos.

(4.5 × 4.5 m) using the energy distribution from the sum of the variance in the temporal frequency domain [13]. The difference of energy stored in the simulated surface wave patches results in differences in the surface wave heights. In this research, significant wave height was used to represent the simulated surface state.

The significant wave height is defined as the average of the highest one-third of the wave heights [10]. It can be used as a representation of wave height of an observed or simulated wave patch. The tendency of simulated significant wave heights changes with α and β as shown in **Figures 5–7** and suggests that simulated water surfaces are smooth with a small α and large β using the Weibull wave spectrum. A larger α and smaller β tend to produce a rougher surface with more energy. However, considering the shallow-water circumstances of this research, α and β should be limited to a range appropriate to the experimental conditions from field measurements. The authors believe that the techniques, method, and the resulting protocol for the measurement of wind-driven surface water gravity waves described and

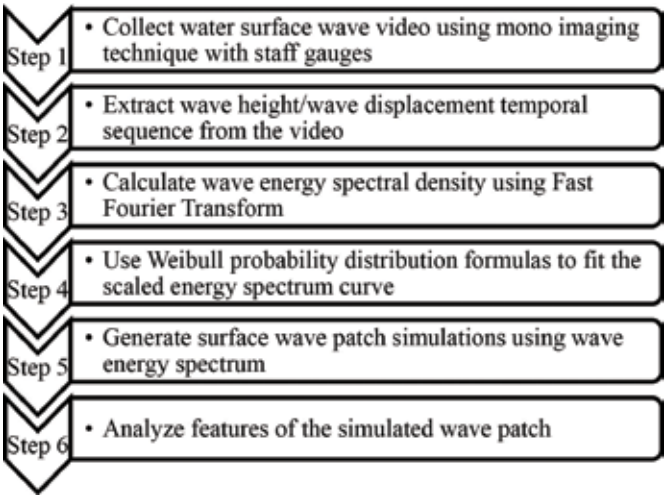

Figure 10. Steps performed to extract wind-driven gravity wave energy and spectra using the protocol methodology described above.

summarized in **Figures 9** and **10** will allow other scientists, engineers, and meteorologists access to an inexpensive and rapidly deployable instrumental approach for shallow waters.

Practical use and applications of water surface video imaging include studying of coastal nearshore processes [14]. The use of fixed sensor video platforms such as bridges, piers, and building which view the littoral zone for water quality constituent determinations has also been demonstrated [15] including the mathematical methods to correct video hyperspectral push broom imagery taken at high oblique angles. Video imaging of bottom features such as seagrasses and sand bottom features has also been demonstrated using practical imaging techniques [16]. The imaging technique described above is being used to assist in assessing moving fluid mud and muck in Indian River Lagoon and Banana River estuarine areas and tributaries [2]. In many shallow-water estuarine regions, wind-driven gravity waves are responsible for resuspension and transport of muds and decaying organic matter within the lutocline [17, 18]. **Figure 11** shows the results of the vertical profile of horizontal mass transport (fluxes) using the water wave video imaging technique in conjunction with simultaneous deployment of a vertical array of six passive Sondes [20] during October 2017. Wind speed during the video wave gauge measurements were 16-17 knots.

Sonde array [20] deployment was 16–17 knots, with east winds in a shallow ≈0.7 m water column and 20–30 cm amplitude wind-driven gravity waves at the location in Banana River near Pineda Causeway [2, 16] near the Atlantic Ocean in Florida (28°12′33.02″N, 80°38′14.72″W). The use of the staff gauge video imaging and Sondes shown in **Figure 11** showed that the shallow-water gravity waves increase the bottom water fine particulate transport or flux of 15,071 g m^{-2} day^{-1} dry weight—nearly 450 times greater than the surface values of 13.1 g m^{-2} day^{-1}. The vertical profile of sediment and particulate mass flux or movement under the waves follows the same profile found in previous studies in tributaries during high flow conditions [19]. The above recent result describes the application of the novel approach to water wave imaging in shallow littoral

http://dx.doi.org/10.5772/intechopen.73042

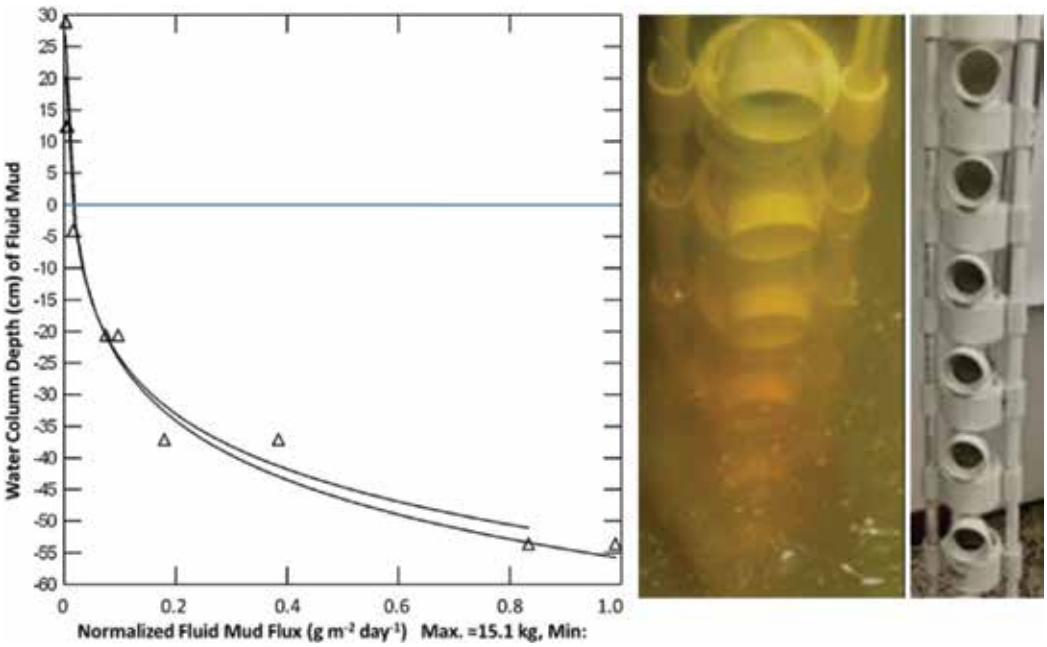

Figure 11. Result (left) from deployment of a vertical array of fluid mud Sondes [20] (right images) in conjunction with video imaging of wind-driven water surface gravity waves (October 2017 (28°12′33.02″N, 80°38′14.72″W)) in a shallow-water littoral zone [2]. The figure demonstrates that water surface gravity waves in shallow coastal areas are responsible for suspending and transporting fluid mud and muck under steady winds of ≈16–17 knots with dry weight mass fluxes (g m^{-2} day^{-1}) at the bottom greater than 450 times the surface transport within surface wave field.

zones. In essence, the novel approach [1] requires no expensive equipment [2], can be easily constructed, and [3] is self-calibrated to video imagery. The method can be used in conjunction with sophisticated wave patch imaging models and when used as a system can be used to improve scientific and engineering understanding of sediment transport due to wind-driven waves. The imaging techniques are currently being used in the field of transportation construction engineering concerned with pile driving rebound imaging and related soil engineering problems.

Acknowledgements

The work presented in this paper has been supported in part by the Northrop Grumman Corporation, the NASA, the Kennedy Space Center, the KB Science, the National Science Foundation, the US-Canadian Fulbright Program, and the US Department of Education, the *FIPSE* and European Union's grant *Atlantis STARS* (Sensing Technology and Robotic Systems) to Florida Institute of Technology, the Budapest University of Technology and Economics (BME), and the Belgium Royal Military Academy, Brussels, in order to support the involvement of students in obtaining international dual US-EU undergraduate engineering degrees.

Author details

Charles R. Bostater Jr*, Bingyu Yang and Tyler Rotkiske

*Address all correspondence to: bostater@fit.edu

Marine Environmental Optics Laboratory and Remote Sensing Center, Ocean Engineering and Sciences, College of Engineering, Florida Institute of Technology, Melbourne, Florida, USA

References

[1] Knauss JA. Introduction to Physical Oceanography. Long Grove, IL: Waveland; 1997

[2] Bostater CR, Yang B. Shallow water surface gravity wave imaging, spectra and their use in shallow water dredging operations. SPIE. 2014;**9240**:92400K-9-92400K-1

[3] Wiberg PL, Sherwood CR. Calculating wave-generated bottom orbital velocities from surface wave parameters. Computers & Geosciences. 2008;**34**:1243-1262

[4] Soulsby RL. Calculating bottom orbital velocity beneath waves. Coastal Engineering. 1987; **11**:371-380

[5] Stewart RH. Introduction to Physical Oceanography. College Station, TX: Texas A&M University; 2004

[6] Benetazzo F, Gallego G, Shih PC, Yezzi A. Offshore stereo measurements of gravity waves. Coastal Engineering. 2012;**64**:127-138

[7] Wanek JM, Wu CH. Automated trinocular stereo imaging system for three-dimensional surface wave measurements. Ocean Engineering. 2006;**33**(5):723-747

[8] Kraus NC. History and Heritage of Coastal Engineering. New York, NY: American Society of Civil Engineers; 1996

[9] Nelson WB. Applied Life Data Analysis. New York, NY: Wiley; 1982

[10] The IAHR Working Group on Wave Generation and Analysis. List of sea-state parameters. Journal of Waterway, Port, Coastal and Ocean Engineering. 1989;**115**(6):793-808

[11] Bostater CR, Chiang G-T, Huddleston L, Gimond M. Synthetic image generation of shallow waters using a parallelized hyperspectral Monte Carlo & analytical radiative transfer model. SPIE. 2003;**5569**:194-208

[12] Bostater CR, Bassetti L. Influence of water waves on hyperspectral remote sensing of subsurface water features. SPIE. 2004;**5569**:194-208

[13] Fréchot J. Realistic simulation of ocean surface using wave spectra. In: Proceedings of the First International Conference on Computer Graphics Theory and Applications (GRAPP), Portugal. 2006. pp. 76-83

[14] Holland KT, Holman RA, Lippmann TC, Stanley J, Plant N. Practical use of video imagery in nearshore oceanographic field studies. IEEE Journal of Oceanic Engineering. 1997; **22**(1):81-92

[15] Bostater CR, Oney TS. Collection and corrections of oblique multiangle hyperspectral bidirectional reflectance imagery of the water surface. SPIE. 2017;**10422**:1042209-1-1042209-22

[16] Bostater CR, Oney TS, Rotkiske T, Aziz S, Morrisette C, Callahan K, Mcallister D. Hyperspectral signatures and WorldView-3 imagery of Indian River Lagoon and Banana River Estuarine Water and bottom types. SPIE. 2017;**10422**:104220E-5-104220E-13

[17] Mehta A, Lee A, Li Y. Fluid Mud and Water Waves: A Brief Review of Processes and Simple Modeling Approaches. US Army Corps of Engineers, CR DRP-94-4. 1994. 79 pp

[18] McAnally W et al. Management of fluid mud in estuaries, bays, and lakes, II: Present state of understanding on character and behavior. Journal of Hydraulic Engineering, ASCE. 2007;**133**:23-38

[19] Vanoni VA, editor. Sedimentation Engineering. American Society of Civil Engineering, ASCE Hydraulic Division Task Committee. 1975. p. 745. ISBN: 0-87262-001-8

[20] Bostater C, Rotkiske T, Oney T, Obot E. "Design and Operation of Sonde Arrays to Measure Fluid Mud in the Marine Environment", Proceedings of ISOPE. 2017. pp. 1511-1514. ISBN: 978-1-880653-97-5

Edited by Farzad Ebrahimi

Surface waves have drawn a significant attention and interest in the recent years in a broad range of commercial applications, while their commercial developments have been supported by fundamental and applied research studies. This book is a result of contributions of experts from international scientific community working in different aspects of *surface waves* and reports on the state-of-the-art research and development findings on this topic through original and innovative research studies. It contains up-to-date publications of leading experts, and the edition is intended to furnish valuable recent information to the professionals involved in surface wave analysis and applications. The text is addressed not only to researchers but also to professional engineers, students, and other experts in various disciplines, both academic and industrial, seeking to gain a better understanding of what has been done in the field recently and what kind of open problems are in this area.

Published in London, UK

IntechOpen

ISBN 978-1-83881-356-7
9 781838 813567